UNIVERSIDADE ESTADUAL DE CAMPINAS

Instituto de Física "Gleb Wataghin"

Bruno César da Silva

Ga-based III-V Semiconductor Nanowires: Growth, New Catalysts and Optical Properties

Nanofios Semicondutores III-V baseados em Ga: Crescimento, Novos Catalisadores e Propriedades Ópticas

Campinas

2020

Bruno César da Silva

Ga-based III-V Semiconductor Nanowires: Growth, New Catalysts and Optical Properties

Nanofios Semicondutores III-V baseados em Ga: Crescimento, Novos Catalisadores e Propriedades Ópticas

Thesis presented to the Institute of Physics "Gleb Wataghin" of the University of Campinas in partial fulfilment of the requirements for the degree of Doctor in Sciences, in the area of Applied Physics.

Tese apresentada ao Instituto de Física "Gleb Wataghin" da Universidade Estadual de Campinas como parte dos requisitos para a obtenção do título de Doutor em Ciências, na área de Física Aplicada.

Supervisor/Orientadora: Prof.ª Dra. Mônica Alonso Cotta

Co-supervisor/Coorientador: Prof. Dr. Fernando Iikawa

Este exemplar corresponde à versão final da tese defendida pelo aluno Bruno César da Silva e orientada pela Profa. Dra. Mônica Alonso Cotta.

Campinas

2020

Informações para Biblioteca Digital

Título em outro idioma: Nanofios semicondutores III-V baseados em Ga : crescimento,
novos catalisadores e propriedades ópticas
Palavras-chave em inglês:
III-V Nanowires
Vapor-liquid-solid growth
Gallium phosphide
Photoluminescence
Área de concentração: Física Aplicada
Titulação: Doutor em Ciências
Banca examinadora:
Mônica Alonso Cotta [Orientador]
Daniel Mario Ugarte
Christoph Friedrich Deneke
Evaldo Ribeiro
Maurício Pamplona Pires
Data de defesa: 27-03-2020
Programa de Pós-Graduação: Física

Identificação e informações acadêmicas do(a) aluno(a)
- ORCID do autor: https://orcid.org/0000-0001-8690-4796
- Currículo Lattes do autor: http://lattes.cnpq.br/9372271927420661

MEMBROS DA COMISSÃO JULGADORA DA TESE DE DOUTORADO DE BRUNO CÉSAR DA SILVA – RA 153903 APRESENTADA E APROVADA AO INSTITUTO DE FÍSICA "GLEB WATAGHIN", DA UNIVERSIDADE ESTADUAL DE CAMPINAS, EM 27/03/2020.

COMISSÃO JULGADORA:

- Profa. Dra. Mônica Alonso Cotta – Orientadora – DFA/IFGW/UNICAMP

- Prof. Dr. Daniel Mario Ugarte – DFA/IFGW/UNICAMP

- Prof. Dr. Christoph Friedrich Deneke – DFA/IFGW/UNICAMP

- Prof. Dr. Evaldo Ribeiro - DF/UFPR

- Prof. Dr. Mauricio Pamplona Pires - IF/UFRJ

OBS.: Ata da defesa com as respectivas assinaturas dos membros encontra-se no SIGA/Sistema de Fluxo de Dissertação/Tese e na Secretaria do Programa da Unidade.

CAMPINAS

2020

Aos meus pais e minha família, em especial, aos

meus irmãos André e Carlos.

Acknowledgments

Um trabalho desta natureza definitivamente não se faz sozinho e durante os quatro anos de desenvolvimento desta tese diversas pessoas me ajudaram, direta ou indiretamente, por isso gostaria de agradecê-las como muito carinho.

Gostaria de agradecer às agências de fomento, em especial, à Fundação de Amparo a Pesquisa do Estado de São Paulo (FAPESP), processo 2015/24271-9, pelo financiamento da minha bolsa, o que proporcionou o desenvolvimento deste trabalho.

O presente trabalho foi realizado também com o apoio da Coordenação de Aperfeiçoamento de Pessoal de Nível Superior (CAPES) - Brasil - código de financiamento 001, processo 1583273/2016.

Também gostaria de agradecer ao Conselho Nacional de Desenvolvimento Científico e Tecnológico (CNPq) por todo suporte institucional e financeiro em diferentes instâncias dentro do programa de pós-graduação do IFGW/Unicamp ao longo do doutorado.

Também gostaria de agradecer ao Laboratório Nacional de Nanotecnologia (LNNano) do Centro Nacional de Pesquisa em Energia e Materiais (CNPEM), ao Laboratório de Caracterização Estrutural (LCE) do Departamento de Engenharia de Materiais (DEMa) da Universidade Federal de São Carlos (UFScar) e também ao Centro de Componentes Semicondutores e Nanotecnologias (CCS) e Instituto de Física "Gleb Wataghin" ambos da Universidade Estadual de Campinas (UNICAMP) pelo acesso às diferentes *facilities* necessárias para o desenvolvimento deste trabalho.

No que toca as pessoas, gostaria de primeiramente agradecer de forma inequívoca a minha orientadora, Prof. Dra. Mônica Cotta, por todo apoio e intenso trabalho nestes últimos 4 anos. Não consigo mensurar a importância dela na minha formação, não só como físico e pesquisador, mas também como pessoa e futuro professor; espero poder um dia representar para os meus alunos o que você representou para mim. Para chegar até aqui você dedicou vários fins de semana, horas extras e muito trabalho, e sem a sua engenhosidade e capacidade de encontrar soluções para diversos percalços experimentais, de análise dos dados e de administração do projeto, uma vez que o projeto envolvia uma grande gama de pessoas e *facilities*, esse trabalho não teria dado os resultados que deu. Além disso, o seu profundo conhecimento sobre o crescimento de semicondutores III-V foi crucial para o meu desenvolvimento e para o alcance dos resultados, nos levando a publicar na Nano Letters. Você sempre me puxou aos meus limites, e hoje eu entendo que foi para o meu crescimento; certamente sem isto eu não teria me

ensinado a fazer litografia por feixe de elétrons. A gente briga, eu sou mau humorado às vezes, mas no final a gente se adora! Te adoro, tá?!

Também gostaria de agradecer aos amigos que fizeram deste final de tese uma coisa menos sofrível e sempre estiveram ali presentes para escutar as minhas lamentações, além de serem excelentes companhias para diversos momentos na minha vida, Rafael Macedo, Bruno Abreu e Gustavo Linhares, amo vocês!

Não poderia deixar de agradecer ao Renato Nogueira, por ter estado do meu lado em boa parte do desenvolvimento deste trabalho, por ter estado comigo nos momentos mais difíceis, foram diversos fins de semana onde eu não pude estar presente ou simplesmente não tinha energia, disposição ou verba (rs) para sair ou fazer algo, mas apesar de tudo, hoje eu entendo que você foi o melhor namorado possível nessas circunstâncias, assim como eu acredito que também fui. Você tem um lugar especial no meu coração.

Por último, agradeço à minha família, em especial à minha avó, Severina Bezerra da Silva, que sempre, sempre, me apoiou incondicionalmente, te amo Vó! E também ao resto da minha família, que nem sempre entendeu o meu caminho, mas que hoje em dia respeita e me apoia.

Resumo

Na primeira parte desta tese, apresentamos um estudo do crescimento de nanofios de fosfeto de gálio (GaP) catalisados por Au e crescidos por epitaxia de feixe químico. Mostramos que a nanopartícula pode se tornar instável, movendo-se na direção ±[110], dependendo das condições de crescimento. Apresentamos várias indicações do impacto desse fenômeno na morfologia dos nanofios, tais como a formação de uma nanoestrutura assimétrica. Além disso, essas nanoestruturas apresentam a fase hexagonal (Wurtzita) com baixa densidade de defeitos cristalográficos estendidos. A fase hexagonal no GaP foi prevista como um material de *band gap* direto com emissão na faixa espectral visível. No entanto, até o momento, existem poucas evidências experimentais sobre algumas informações básicas desse material relativamente novo. Assim, na segunda parte da tese, apresentamos uma série de dados de medidas ópticas obtidos por diversas técnicas, a fim de elucidar o valor exato do *band gap* fundamental, emissão excitônica e energias do *splitting* das bandas de valência. Nossos dados indicam a existência de um *band gap* óptico em 2.19 eV a 10 K, bem como um comportamento de *band gap* pseudo-direto, ou seja, uma transição eletrônica quase proibida por dipolo elétrico. Além disso, a partir desses dados propomos a origem e a natureza de impurezas não intencionais incorporadas no GaP, bem como de alguns defeitos pontuais, que apresentaram comportamentos ópticos distintos de acordo com as condições de crescimento. Por último, uma vez que o uso de ouro como catalisador tem alguns aspectos indesejados no crescimento de nanofios, além de não ser a melhor opção para a integração de nanofios de semicondutores III-V na tecnologia baseada em silício, analisamos catalisadores alternativos para o crescimento de nanofios de fosfeto de gálio (GaP) e arseneto de gálio (GaAs), tais como níquel (Ni) e estanho (Sn). Mostramos que o Ni pode ser usado com sucesso como catalisador em condições semelhantes relatadas para o ouro. No entanto, a dinâmica do crescimento tem uma mudança dramática, levando a nanoestruturas com características muito diferentes daquelas crescidas com o ouro, como a direção de crescimento <11-2>. Além disso, nanofios de alta razão de aspecto, dificilmente obtidos para compostos baseados em Ga catalisados por Au em nosso sistema CBE, devido à difusão superficial mais lenta do Ga e sua menor solubilidade em Au, podem ser crescidos em Si (100), apresentando emissões ópticas adicionais não observadas em nanofios crescidos com Au.

Abstract

In the first part of this thesis, we present a study of the growth of gallium phosphide (GaP) nanowires catalyzed by Au and grown by chemical beam epitaxy. We show that the nanoparticle can become unstable, moving in the $\pm$ [110] direction, depending on growth conditions. We present several indications of the impact of this phenomenon on the nanowire morphology, such as the formation of an asymmetric nanostructure. Furthermore, these nanostructures present the hexagonal phase (Wurtzite) with low density of extended crystallographic defects. The hexagonal phase in GaP was predicted as a direct band gap material with emission in the visible spectral range. However, so far there is little experimental evidence about some basic information from this relatively new material. Thus, in the second part of the thesis, we present a series of optical measurement data obtained by different techniques, in order to elucidate the exact value of the fundamental band gap, excitonic emission and splitting energies of the valence bands. Our data indicate the existence of an optical band gap at 2.19 eV at 10 K, as well as a pseudo-direct band gap behavior, that is, an electronic transition almost prohibited by electric dipole. In addition, from these data we propose the origin and nature of unintentional impurities incorporated in GaP, as well as some specific defects, which showed different optical behaviors according to the growth conditions. Finally, since the use of gold as a catalyst has some unwanted aspects in the growth of nanowires, besides not being the best option for the integration of III-V semiconductor nanowires in silicon-based technology, we analyze alternative catalysts to grow gallium phosphide (GaP) and gallium arsenide (GaAs) nanowires, such as nickel (Ni) and tin (Sn). We have shown that Ni can be used successfully as a catalyst under similar conditions reported for gold. However, the dynamics of growth has changed dramatically, leading to nanostructures with very different characteristics from those grown with gold, such as the direction of growth <11-2>. In addition, nanowires of high aspect ratio, which are difficult to obtain for Ga-based compounds catalyzed by Au in our CBE system due to the lower surface diffusion of Ga and the lower solubility in Au, can be grown in Si (100), presenting additional non-optical emissions observed in nanowires grown with Au.

Contents

Chapter 1

Introduction

1.1 Materials for optoeletronics: new opportunities using semiconductor nanomaterials

Solid state lightning presents huge technological and commercial implications and has been an active area of research. Several optoeletronic devices rely on the ability to generate and/or detect light in a wide spectral range - from far infrared to near ultraviolet emission - by using semiconductor materials [1, 2, 3, 4]. Although microeletronics is dominated by Silicon (Si) technology, the indirect bang gap of this material provides poor light emission/absorption. Therefore, Si is not the best candidate as an efficient light source.

In the last sixty years, III-V semiconductor compounds have been extensively studied and are commercially used in different segments of optoeletronics. Their direct band gap allows the fabrication of highly efficient solar cells and Light-Emitting Diodes (LED's) [5, 6]. Green and red LED's have become reality very early after initial research. However, we had to wait until the 90's for the development of bright blue LEDs based on GaN/InGaN [7, 8, 9], which allowed the white LED to become a commercial reality nowdays. Nevertheless, some limitations hinder the widespread application of III-V materials into optoeletronic devices as, for example, their cost and the low compatibility with Si, for thin films [10]. Moreover, highly efficient green/amber light emitting semiconductor material have yet to be developed, in order to achieve improved white LED performances [11, 12].

Currently, different materials have attracted attention as potential candidates for optoeletronic devices as transition metal dichalcogenides (TMD's) [13] and perovskites [14] Despite the great interest in these materials today, they also present huge challenges. TMD's have direct band gap in the form of a monolayer, but the ability to controllably produce perfect monolayers in large scale to fabricate devices has yet to be demonstrated [13]; perovskites, on the other hand, suffer with stability issues [14]. Therefore, III-V compounds are still attractive options for advanced optoeletronic devices, and new possibilities have emerged by growing III-V compounds in the nanoscale.

With the advance in scientific ideas and characterization tools in the last decades of the 20th century, a large interest in nanosystems and semiconductor nanomaterials in particular, such as nanowires (NWs), has showed up [15, 16, 17]. Semiconductor NWs first demonstrated the possibility to combine different III-V semiconductors that were not compatible in thin film technology; moreover, nanowires also allowed innovations in heterostructure engineering [18]. In particular, highly mismatched heterostructures were made possible due to the small contact area between nanowires and substrate and the lateral freedom of these structures, creating the possibility of monolithic integration of III-V devices onto Si chips. During the last twenty years, important advances in nanowire growth, related to the understanding of the crystal growth process at nanoscale, as well as the development of prototype devices have been demonstrated [19, 20, 21, 22].

However unlikely that III-V nanostructures replace Si in microelectronics, their application in optoeletronics can certainly be successful due to the interesting properties observed using nanomaterials. For example, band gap engineering, which involves the transformation of traditionally indirect gap materials in direct band gap semiconductors, as well as cost reduction by employing less material and allowing the unique combination of different large mismatched semiconductor materials.

Therefore, so that nanowire-based fabrication of optoeletronic devices becomes a reality, fundamental growth studies and the development of new growth procedures, which allow the fine control of crystal structure, morphology, optical and eletrical properties, are still required. The full understanding of basic material properties is also important, as the band gap value, excitonic energies, ionization energy of the impurities, phonon energies and etc. Moreover, a solid state light source based on III-V semiconductors and integrated into Si technology is also interesting for the development of on-chip photonics, which could revolutionize data signaling and processing [23].

1.2 Why does optoeletronics requires direct band gap semiconductors?

Semiconductor materials are systems in which electrical properties are intermediate between insulators and conductors. The conductivity in semiconductors can be modified by providing small energy values to the system, for example, with increasing temperature. This is possible because in a semiconductor the valence band, which is completely filled at 0 K, is separated from the conduction band, which is empty at 0 K, by a few eV difference. A small increase in energy allows the promotion of electrons from the valence to the conduction band,

increasing the material conductivity. This is not possible in insulators, which have a much larger forbiden band gap, in general, greater than 4 - 5 eV [3, 4]. The conductivity can also be modulated by adding a small amount of substitutional foreign atoms, i.e., impurities. In this case, the semiconductor material is called doped, and the majority of carriers can be electrons or holes, as one dopes the material as n-type or p-type, respectively.

Semiconductor materials have their optical properties largely determined by the nature of their band gap; the emission region in the electromagnetic spectrum and the efficiency of the luminescence both depend on the value and nature (direct/indirect) of the band gap. For a direct band gap, an electron can be excited from the valence to the conduction band when a photon, with energy equal to or larger than the band gap energy, is absorbed. On the other hand, in a material with indirect band gap, in addition to the photon, a phonon is also required, for moment conservation [3, 4].

The recombination of carriers (electrons and holes) in a semiconductor does not always generate energy in the form of light. The recombination process can be radiative, generating photons; or non-radiative, generating phonons (energy in the form of heat) or emission of electrons (Auger electrons). These processes occur simultaneously and compete with each other in a semiconductor material. Thus, in materials with indirect band gap, the assistance from a phonon for radiative recombination to occur makes the process much less probable than non-radiative recombination processes. Therefore, materials with indirect band gap, such as silicon (Si) and germanium (Ge), do not show good optical emission. However, radiative recombination is the dominant process in materials with direct band gap, making them efficient light emitters/absorbers and natural candidates for optoelectronic devices [3,4].

1.3 The growth of III-V semiconductor nanowires

Nanowires are nanostructures with at least two dimensions in the order of few dozens of nanometers; they usually present conical or cilindrical morphologies and can be grown using different techniques. In literature, nanowires are usually obtained from the same vapor-phase epitaxy systems that were used for thin film growth. In this case, the anisotropic crystal growth is usually promoted by a metal nanoparticle (a group III droplet for self-catalyzed nanowires [24]) in the Vapor-Liquid-Solid (VLS) mechanism [25] as well as selective area epitaxy (SAE) [26], growing in the mask-free areas on the substrate surface. The VLS mechanism using gold (Au) as catalyst is the most popular growth technique already used for several III-V nanowires such as InP, GaAs, GaP, InAs and ternary alloys [27]. Self-catalyzed

nanowires are also interesting [24], but they suffer from the position control of the structures, since the growth is nucleated by a spontaneous group III droplet formed on the substrate surface. More recently, SAE has demonstrated promising results [28].

Micron-sized wires have been reported in literature since the 60's, specially due to the pioneering work develop for Wagner and Ellis, studying gold (Au)-catalyzed Si whiskers [25]. They have proposed the Vapor-Liquid-Solid (VLS) mechanism in order to understand the anisotropic crystal growth promoted by the Au particles. In the 90's Hiruma et al. have applied the same method to study III-V nanowires [29, 30]. Despite the much more complicated growth process in this case, this method has been massively used to growth semiconductor nanowires as well as to study fundamental crystal growth processes at the nanoscale.

VLS growth usually occurs along the <111> crystal orientation in a layer-by-layer mode starting at the interface between the gold nanoparticle and the substrate, which results in anisotropic axial growth. This VLS axial growth is accompanied by Vapor Solid (VS) growth on the nanowire sidewalls, which depends on the crystal facets exposed, and can affect the nanowire aspect ratio; symmetric or asymmetric morphologies are thus obtained [27]. The morphology can be controlled in situ by using HCl vapor during growth in order to supress VS growth on the sidewalls and therefore increase the nanowire aspect ratio [31]. The formation of different geometries are interesting for applications and have attracted attention, as in high efficiency light polarized InP nanoflags [32], enhanced light scattering InAs nanomembranes [33] and high electron mobility InSb nanosails [34, 35]. Thus, it is important to develop new bottom-up strategies to control nanowire morphology.

1.4 Band gap engineering: exploring polytypism in nanosystems

Most of the III-V semiconductors (except the III-N) adopt the Zinc Blend (ZB) crystal structure, from the cubic system. However, in nanosystems as nanowires, surface effects are more prominent than in classical crystal growth processes, which leads to the synthesis of material in thermodinamically less probably phases, as the Wurtzite (WZ) structure, from the hexagonal system. This change in the atomic arrangement has been used in the last years to change the eletronic properties of these well-known materials. Although this phase has been predicted to be stable just for nanowires with small (a few nm) diameters [36], it has been experimentally demonstrated beyond this limit, leading to new theoretical developments [37]. In particular, DFT calculations have predicted the possibility of turning indirect band gap materials such as Germanium (Ge) [38], Silicon-germanium alloys (SiGe) [39], Aluminum

Phosphide (AlP) [40], and Gallium Phosphide (GaP) [41] into direct band gap semiconductors upon crystal phase transition, from cubic to hexagonal. These calculations were the motivation to intensive growth-oriented and properties-based research, carried out for nanowires based on these materials.

1.5 Gallium Phosphide

Bulk crystals and thin films of Gallium Phosphide exhibited the ZB crystal structure; in that form, GaP is an indirect band gap semiconductor with gap energy $E_g = 2.34$ eV (at 5 K) [42, 43]. Seventy years ago GaP was discovered to produce green luminescence and extensive studies were carried out in undoped and p-n junctions of GaP in order to elucidate the radiative recombination mechanism involved in such emissions. They were associated with the presence of different impurities in the material such as Zn, Cd and O [44, 45, 46, 47, 48].

Despite the indirect band gap of ZB GaP, its doping with Nitrogen (N), substituing P, forms an isoeletronic trap, producing green emission at room temperature [49, 50, 51]. An isoeletronic trap is formed when an element of the host material is replaced by another from the same periodic group, but with different eletronegativity. The substitution of P (lower eletronegativity than N) by N in the crystal lattice results in a strong short range force; when an electron is captured, a bound exciton is formed, leading to very localized states in real space and greatly extended in k-space, increasing the transition probability. Thus, even though ZB GaP is a indiret band gap, room temperature green luminescence can be obtained in such system by doping with N_p (nitrogen in substitutional position replacing phosphorus). Although the emission from GaP:N is not very efficient, this system has been quite well explored for the fabrication of commercial green light-emitting-diodes [52].

Therefore, investigating in detail the physical origin of the radiative recombination mechanisms, as well as their formation and how to control them, is extremely important in order to rationally fabricate an optoeletronic device. In this context, due to the advances of the synthesis as well as the characterization techniques employed in nanosystems, the formation of unstable phases such as WZ GaP has been made possible. However, properties change with the crystal structure, and the basic properties of WZ GaP are poorly known. DFT calculations have suggested that in the hexagonal phase a direct band gap for this material can exist, with the energy values smaller than for the cubic phase, but still in the green spectral range [40, 53, 54]. However, there are only few optical studies about WZ GaP NWs, and different questions

remain unanswered as, for example, the value and the true nature of hexagonal GaP band gap [41, 55, 56, 57, 58].

1.6 The outline of this thesis

In this thesis we present a study about growth dynamics and optical properties of III-V semiconductor nanowires. Two chapters are dedicated to Gallium Phosphide (GaP). In chapter 3 we report an investigation of the control over the morphology due to gold catalyst instabilities, which leads to the formation of asymmetric WZ GaP nanowires. The basic optical properties of these hexagonal GaP nanowires were also investigated and results are presented in chapter 4. Chapter 5 is dedicated to growth studies of new metal catalysts for the growth of Ga-based III-V nanowires. Chapter 6 presents our main conclusions and future perspectives.

Spontaneous thermally-activated Au motion on III-V surfaces has been studied due to the role of the gold nanoparticle on the VLS mechanism. In particular, the ability to control droplet crawling opens up the possibility to create novel structures and to facilitate nanowire integration into device fabrication, through a process totally determined by an in situ mechanism which can reach similar size limits as electron beam lithography, as suggested earlier [59]. The fabrication of oxide free surfaces by Au droplet crawling has already been observed [59, 60]; however, the direct impact of Au droplet motion in nanowire growth to create novel morphologies has not been determined yet.

In chapter 3, we expand a preliminary study[61] about the growth dynamics of GaP nanowires in order to determine the growth mechanism behind the formation of the asymmetric GaP nanowires. It is shown that the formation of this singular morphology is related to the thermally-activated crawling of the small Au nanoparticles on the substrate surface, which creates oxide-free areas, modifying growth dynamics. This phenomenon leads to the modification of nanowire morphology, and an asymmetric shape is obtained, rather than conical or cylindrical nanowires. These results could be interesting for light-harvesting applications, such as antireflective coating in solar cells [62, 63, 64].

The GaP nanowires discussed in chapter 3 present WZ crystal structure with few extended crystal defects. Therefore, in chapter 4 we discuss the optical properties of these GaP structures by measuring the optical absorption edges using Photoluminescence Excitation Spectroscopy (PLE). In order to accomplish that, very large (micron-sized) GaP structures were obtained for the first time in literature. We were thus able to measure the WZ GaP band gap at (2.19 ± 0.02) eV (10 K) as well as the valence band splittings. In chapter 4, we show how these

results provide understanding about the nature of the WZ GaP band gap, which is supported by DFT calculations performed by our collaborators.

The photoluminescence (PL) of WZ GaP nanowires is dominated by impurity luminescence; these impurities are unintentionally incorporated [56, 58, 65]. In fact, the ionization energies of impurities in WZ GaP have not been obtained so far, neither how to control their incorporation in the material. Thus, using our optical data, we tentatively assign some possible candidates for the typical emissions observed, associated with deep and shallow impurities. We also discuss about the impact of growth conditions on the overall luminescence properties, i.e., in the residual impurity incorporation.

Finally, one of the great advantages of nanowires is the possibility to grow III-V semiconductors on Si without the formation of structural defects, which may occur in the case of a large lattice mismatch. However, Au is not the best option as catalyst for integration of III-V semiconductors on Si. Thus, we have searched for different metals, rather than gold, to study the anysotropic crystal growth of GaAs and GaP at nanoscale. In chapter 5, we discuss the use of Tin (Sn) to grow nanowires, but Ni it was also found in the metal catalyst, and was also explored for VLS growth. Using pure Ni as catalysts, high aspect ratio GaP nanowires, with high yield, were obtained; impurity luminescence was also observed, with differences in PL spectra regarding the Au-catalyzed material. Some interesting questions concerning the growth process involving the Ni-catalyzed nanowires are also discussed.

Chapter 2

Epitaxial growth, characterization techniques and fundamentals

2.1 Nanowire Growth: Chemical Beam Epitaxy CBE

Epitaxy is a word that comes from the Greek "epi", which means above, and "taxis" meaning an ordered manner. This term is used to describe the crystal growth process where the precursor material is deposited on a substrate surface and the crystal formation will be directly influenced by the substrate crystal structure and surface.

Among many growth techniques, Chemical Beam Epitaxy (CBE) [66] has been used for III-V compounds. In fact, CBE joins features from two other widely used thin film growth techniques, MOVPE (Metalorganic Vapor Phase Epitaxy) and MBE (Molecular Beam Epitaxy). The three techniques are similar in the sense they rely on the exposure of a heated substrate to gas or vapor precursors containing the elements of interest, which will then provide epitaxial growth. The main difference between these three techniques is the chemical nature of the precursors, and the environment in the growth chamber.

Basically, the CBE technique uses chemical compounds in vapor phase as precursors of the elements of interest, similarly to the MOVPE technique, allowing precise control over their flow. Moreover, in CBE the growth is performed in a high vacuum chamber as in MBE and, since the distance between the precursors entering the chamber and the substrate is smaller than the mean free path of the molecules used, molecular beams are formed and reach the substrate, as also in MBE. Working pressures in the CBE chamber during growth are in the order of 10^{-5} Torr.

The nanowire growth in this work was carried out in the CBE model Riber 32 system installed in the Department of Applied Physics at IFGW-Unicamp. A schematic representation of the CBE system is shown in Fig. 2.1. In this system growth of III-V semiconductor compounds formed from the elements In, Ga, As and P is possible. Hydrides - phosphine (PH_3) and arsine (AsH_3) - are used as group V precursors. For group III precursors, organometallic (OM) vapors from trimethylindium (TMI) ($In(CH_3)_3$) and triethylgallium (TEG) ($Ga(C_2H_5)_3$) are used. In addition, dopants during growth, in this case Beryllium (Be) and Silicon (Si), can be introduced from effusion cells as shown in Figure 2.1.
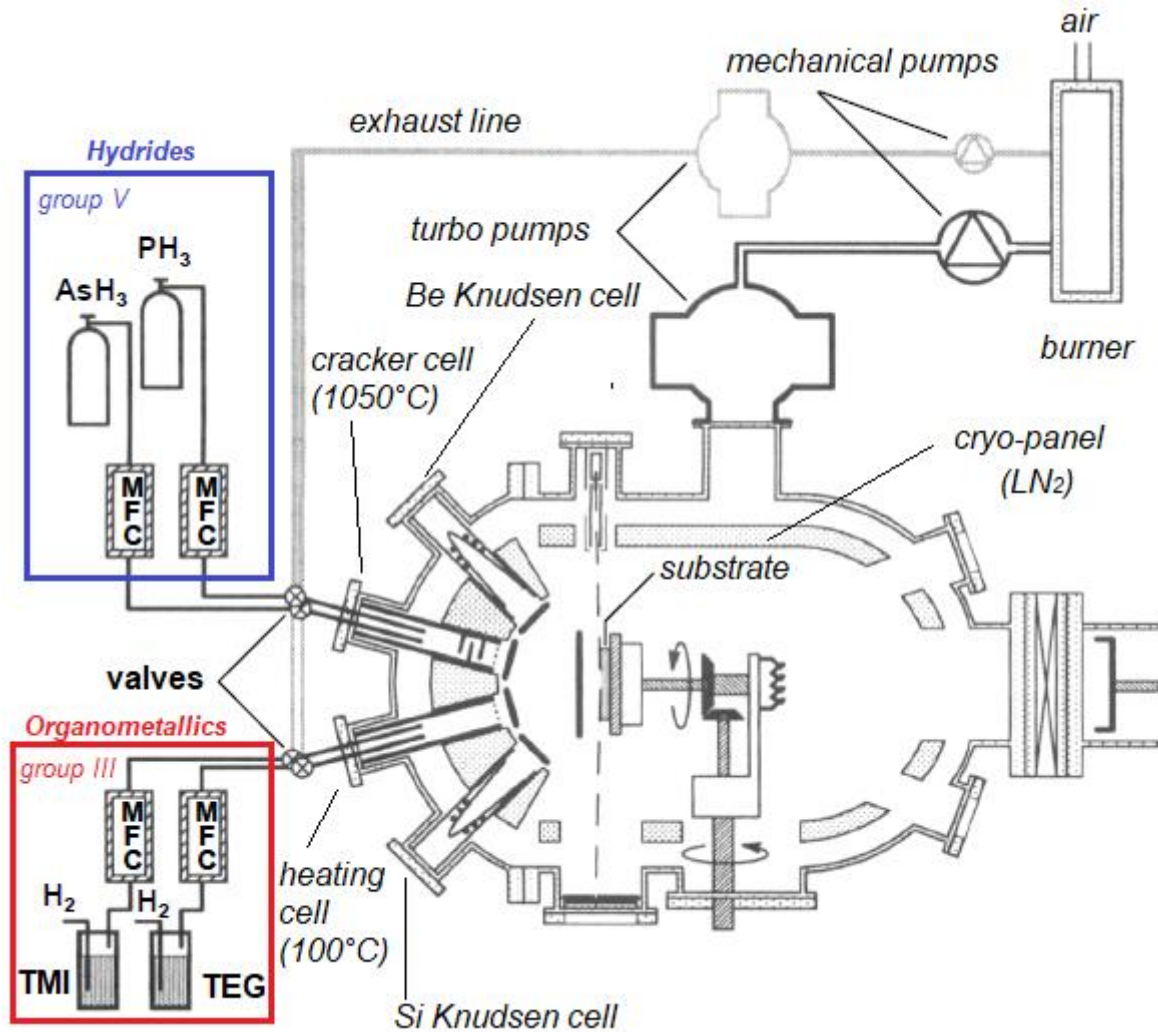
Figure 2.1 – Schematic representation of the CBE system installed in the DFA-IFGW/Unicamp, adapted from [67].

The growth chamber contains a cryo-panel, which is filled with liquid nitrogen (LN_2) during growth to prevent desorption of molecules from the chamber inner walls, Fig. 2.1. Growth occurs as pyrolysis of the precursors on the heated substrate provide the elements of interest. The hydrides are thermally broken in a cracker at ~ 1050 °C before being introduced into the chamber as shown in Fig. 2.1. In turn, organometallics undergo pyrolysis on the surface of the substrate since the temperature at which these molecules break (~ 300 °C) is below working temperatures during growth. A heating cell maintained at ~ 100 °C is used to avoid organometallic condensation before reaching the growth chamber, as depicted in Fig. 2.1.

Group V precursor flow is controlled by a pressure controller that keeps the line at 1 atm and a mass flow controller (MFC) that controls the amount of material supplied during growth. Our MFC has the following characteristics: flow control from 1 to 100% of the

maximum flow of 50 sccm (Standard Cubic Centimeter per Minute), accurate to within ± 0.5 sccm.

The flow control of group III precursors is slightly different. Due to the low vapor pressure of the organometallic (OM) compound, it is necessary to introduce a carrier gas; in this case hydrogen (H_2) is used. A capacitive pressure gauge (Baratron) measures the pressure of the mixture $H_2 + OM$, which is kept constant at the preset value (30 Torr), and a MFC controls the mixture flow. In this case, the MFC allows control from 1 to 100% of the maximum flow of 20 sccm, with accuracy ± 0.2 sccm.

2.2 Epitaxial growth of semiconductor nanowires using the Vapor-Liquid-Solid mechanism

Any crystal growth synthesis is a phase transformation process and the driving force is controlled by thermodynamics, while the rate for crystallization is determined by kinetics. In order to understand the growth process we can define basic growth parameters using the simple model provided by the classical nucleation theory (CNT) [68, 69]. According to CNT, for the homogeneous case, a new phase will emerge from the formation of a small nucleus (cluster) from the old phase [68, 69] This small cluster will form and, under favorable conditions, it will expand giving way to the new phase, or depending on the growth conditions, it will dissolve and the new phase will not form.

The conditions under which the new phase is formed can also be described by CNT. Although this theory was developed to the macroscopic scale, it is a reliable first approach to the study of the growth of nanostructures such as nanowires, which occurs in a more complicated scenario since it is a heterogeneous system. In CNT, for the case of homogeneous nucleation, Gibbs free energy is calculated considering the formation of a small spherical nucleus of radius R. In the case of homogeneous nucleation a new phase will appear from any point in the old phase, with no preferential nucleation sites, Fig. 2.2.
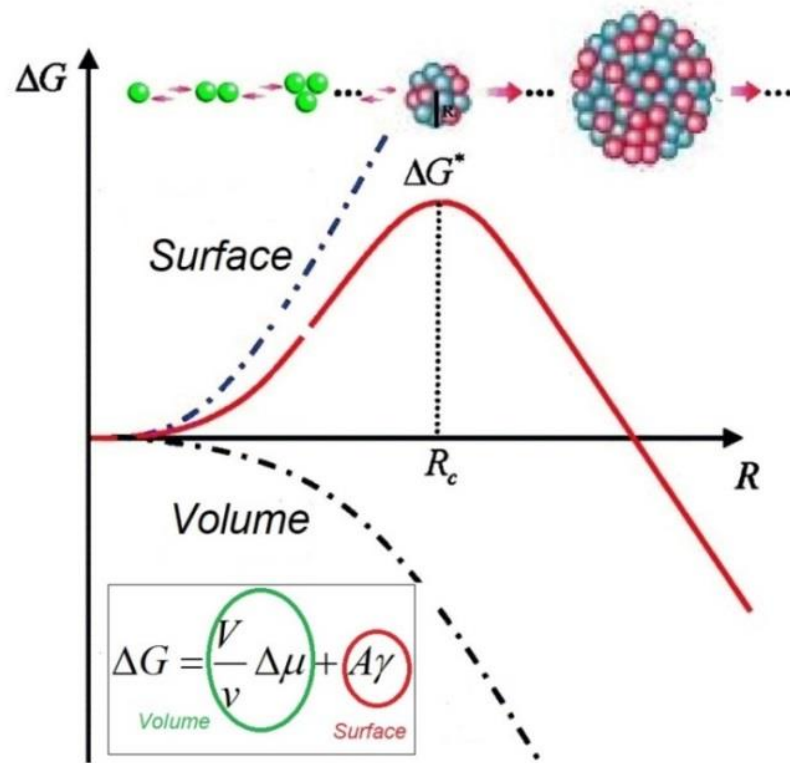
Figure 2.2 – Variation of Gibbs free energy for the formation of a small spherical cluster from a new phase according to the radius, where $A = 4\pi R^2$ and $V = \frac{4}{3}\pi R^3$. The behavior of the terms of surface and volume is highlighted in ΔG. Figure adapted from reference [70].

Considering the formation of a spherical cluster of the new phase with a volume (which depends on the volume of each atom and the number of atoms that make up the nucleus), the variation of Gibbs free energy in this process can be described by two terms, dependent on the volume and the surface, respectively [70]:

$$\Delta G = \frac{4}{3}\pi R^3 \Delta\mu + 4\pi R^2 \gamma \, , (eq. \, 2.1)$$

where γ is the interfacial energy per unit area of the surfaces exposed by the nucleus, $4\pi R^2$ it is the surface area of the nucleus and, since there is an energy cost for the formation of a surface (formed by not fully coordinated sites, with greater energy in relation to an atom within the volume), $\gamma > 0$. In the volume term we have the difference in energy per particle between the new and the old phases, given by:

$$\Delta\mu = \mu_{new} - \mu_{old} \, . (eq. \, 2.2)$$

We can also see from Fig. 2.2 that the term referring to volume, provided that the system is in a condition of supersaturation ($\Delta\mu < 0$), will lead to a decrease in the free energy of the system, while the contribution resulting from the surface term will lead to an unfavorable situation for increasing the cluster. The combination of the two is illustrated by the red curve, from which we can see that there is an energy barrier for the formation of the cluster, called a nucleation barrier. For $R > R_c$ the growth of the nucleus would be the favorable condition, leading to a decrease in free energy. This can be achieved by modifying the supersaturation of the system, so that the nucleation barrier will be overcome with a dominant volume term. Thus, the small cluster will expand, leading to the new phase. The supersaturation of the system can be modified by controlling the variables that define this parameter such as concentration of the elements, pressure, etc, depending on the growth technique.

To discuss the Vapor-Liquid-Solid (VLS) mechanism we will use the simple gold-silicon (Au-Si) binary system [25], as a model to introduce the basic steps of the VLS model, as presented in Fig. 2.3, which are essentially similar for III-V compounds. The VLS consists of the contact of a metallic nanoparticle (NP) with the precursors in the gas phase, Fig. 2.3-(2), forming an eutectic alloy; when growth temperature is reached, the nanoparticle melts, becoming a preferential site for the decomposition of the precursors. Thus, in the region close to the NP there will be an excess of material that leads to its incorporation until the NP reaches a condition of supersaturation, causing the deposition of the crystalline semiconductor material at the interface with the substrate, Fig. 2.3-(3). From this process, monolayer to monolayer, Fig. 2.3-(4), with nucleation of a cluster and subsequently layer growth, an anisotropic structure, in the form of a needle, can be obtained, Fig. 2.3-(5). This is the most accepted model for VLS growth, validated by electron microscopy data in the case of III-V NWs [21, 71]. There are, however, different scenarios for VLS growth in conditions more distant from equilibrium that will not be discussed here.

In addition to the axial growth provided by the VLS mechanism, there is also growth at the crystallographic facets, forming the nanowire sidewalls, which minimize the free energy of the system. These facets can act as a substrate in relation to the vapor phase containing the material of interest, resulting in growth of thin films, free of the catalyst and called VS (Vapor-Solid), Fig. 2.3-(6). The base of the nanowire is always exposed longer than the new layers at the top, resulting in larger VS growth at this former region which, consequently, leads to tapered nanowire morphologies, Fig. 2.3-(6).
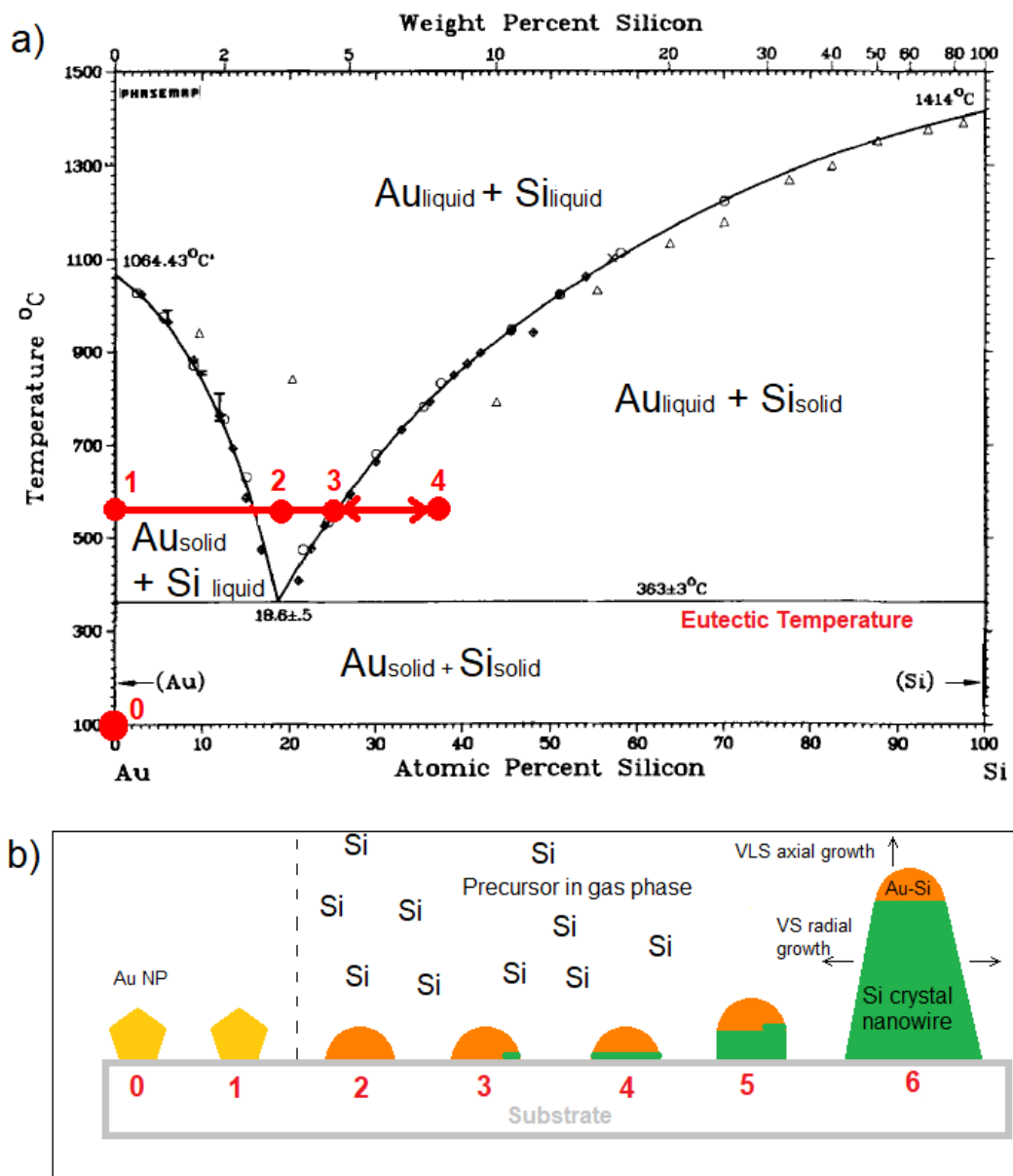
Figure 2.3 – (a) Phase diagram of gold-silicon eutectic system, in which points of interest for VLS growth are highlighted [72]. (b) Steps of the growth of semiconductor nanowires according the VLS mechanism. Initially (0), the Au nanoparticles are in a solid state. By heating the sample above the eutectic temperature (1) and, subsequently, exposing the system to the precursors in vapor phase, an eutectic alloy forms, and the nanoparticle melts (2). After incorporating enough Si into the metal, the NP reaches a condition of supersaturation and deposition of crystalline silicon at the interface with the substrate occurs (3). The NP eventually achieves high supersaturation in which nucleation and the layer growth occurs more quickly (4). After the formation of the monolayer, the NP returns to point (3) with the expulsion of material from its volume; then it absorbs more material from the vapor phase, reaches again a condition of supersaturation and new monolayer forms (5). The continuous sequence of steps (3) and (4), monolayer by monolayer, allows the formation of the nanowire (6). Moreover, during growth the sidewalls are also exposed to the vapor precursors, leading to sidewall deposition, Vapor-Solid (VS), and the final structure presents a conical shape (6).

Basically, the phase diagram obtained for the bulk provides an indication of which materials to use for the NP (materials that form an eutectic alloy with the semiconductor to be grown) and at which growth temperature to work, above the eutectic temperature of the system (temperature at which the eutectic alloy melts), in the case of VLS growth. The scenario for III-V compound growth is more complicated because it involves at least three components, element III, element V and the metal nanoparticle. Scarce information is found concerning ternary phase diagrams, which makes a similar analysis difficult. Here, the supersaturation depends on the concentration of group V and group III elements in the metal nanoparticles, $\mu(C_{III}, C_V)$. The VLS mechanism assumes the formation of an eutectic alloy between the metallic NP and the semiconductor material of interest. However, it has been reported extensively, through in-situ and post-growth chemical analysis that the Au nanoparticle gets rich in group III, rather than group V elements [22, 73]. These results indicate that the group III element plays a more deterministic role to control supersaturation and the crystal structure [73]. However, as we can see in Fig. 2.4, the phase diagram for Au-Ga system is much more complicated than the simple eutectic Au-Si system.
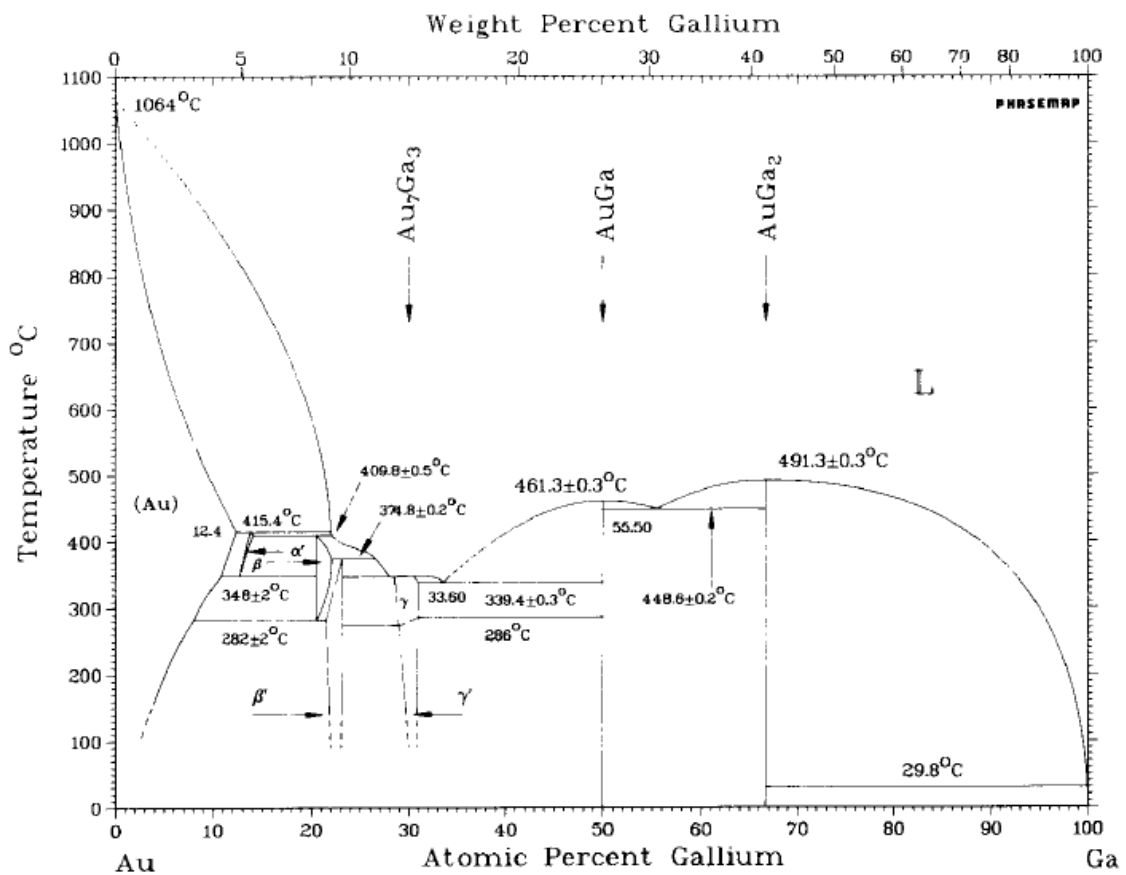
Figure 2.4 – Phase diagram of the Au-Ga system [74].

Therefore, the choice of a new catalyst to be used along with the VLS mechanism should be based on the phase diagram of this metal and the group III and V elements that form the compound. However, due to the scarce information available for ternary phase diagrams and the dominant role of group III elements observed in VLS literature, at least for Au catalysts, we can use binary phase diagrams (group III-metal) instead. This preliminary analysis accounts for determining the possibility of crystal growth along with growth temperatures for that (i.e., above the eutectic temperature for the bulk case). In Fig. 2.5 we can see the phase diagram for the Sn-Ga system, showing that an eutectic alloy is possible and that the eutectic temperature is very low, and easily achieved with most growth systems. Hence, we expect that Tin (Sn) is a possible catayst for Ga-based III-V nanowires. Indeed, recently, the possibility to grow well ordered GaAs NWs using Sn nanoparticles by MOVPE in a narrow growth temperature window was reported by Sun et al [75]. Therefore, in this thesis we have chosen Sn as catalysts for growing GaAs NWs in our CBE system, which has not been reported so far, providing more information about growth dynamics when this new catalyst is used for GaAs. We have also explored Sn catalysts for GaP NWs. We should mention here that we have also explored other different metals as Cu, Al and Ag for nanowire growth. The results were not as successful, but are discussed in appendix B of this thesis.
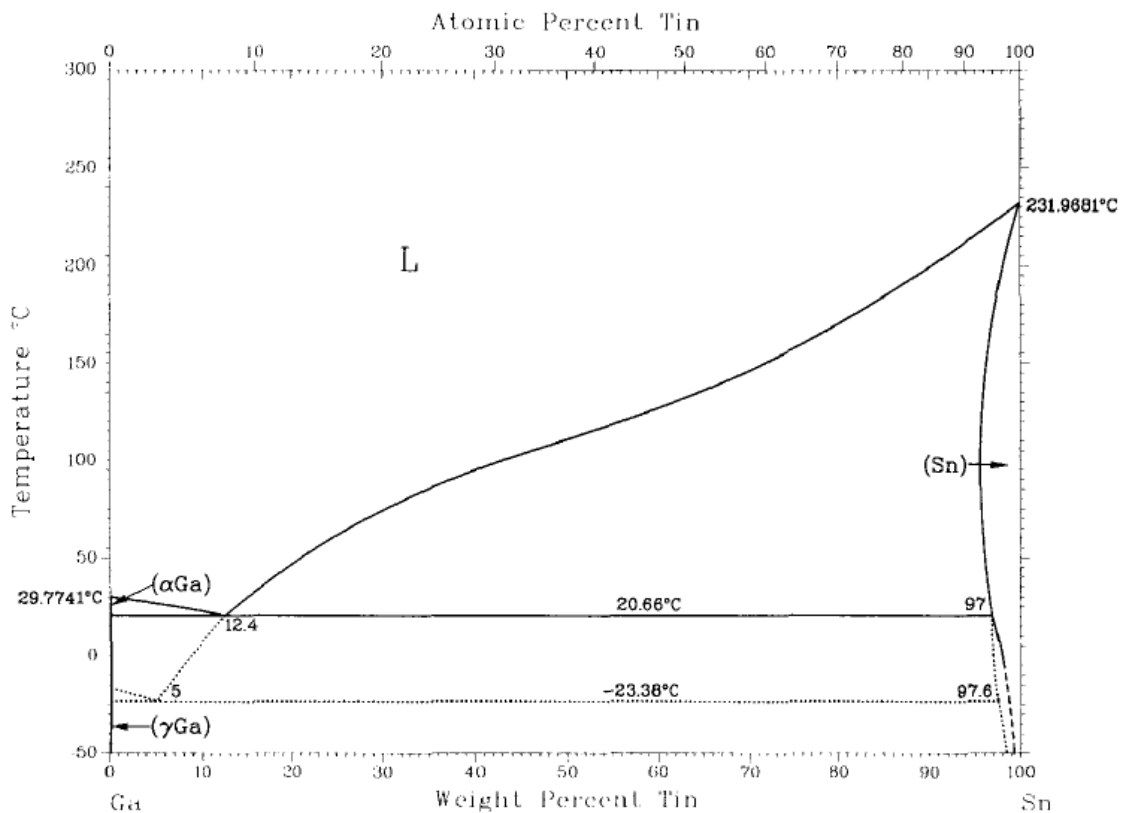
Figure 2.5 – Phase diagram of the Sn-Ga system [76].

Interestingly, as we will show in chapter 5, during the investigation of Sn-catalyzed VLS growth nanowires, we found out that Ni was the actual catalyst for GaP NWs. The phase diagrams for the Ni-P and Ni-Ga systems are presented in Fig. 2.6 and Fig. 2.7, respectively. We will also discuss the group V-Ni system because, as we will discuss in chapter 5, group V elements could play an important role in VLS mechanism in this case.
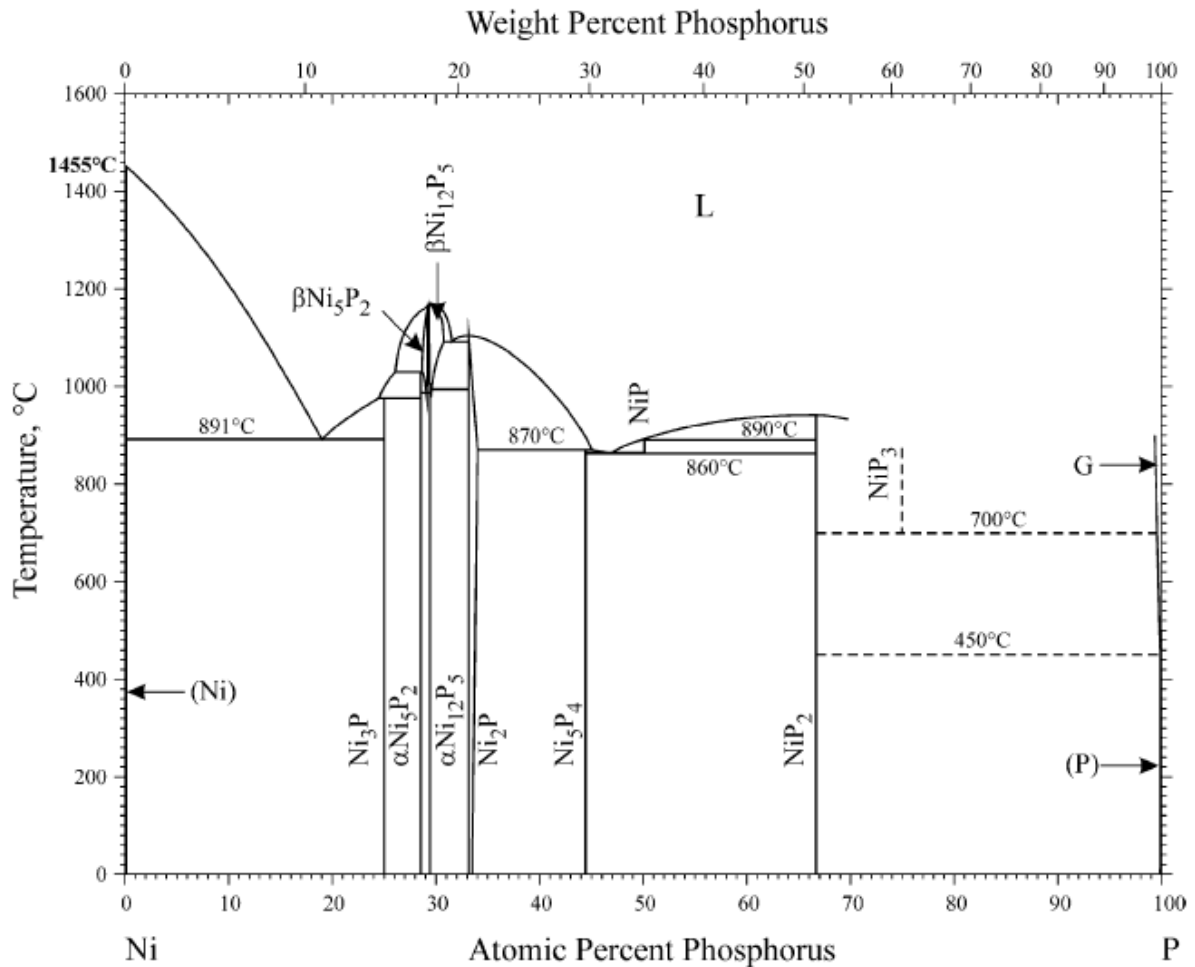
Figure 2.6 – (a) Phase diagram of the Ni-P system [77].

Based on the discussed analysis of phase diagrams, Fig. 2.6 and 2.7 indicate that classic VLS growth is unlikely, in both cases. However, the analysis of the ternary phase diagram of Ga, P and Ni is needed to further understand the crystal growth in this case. This also shows how the scenario for metal-catalyzed III-V nanowires is more complex than for the simple Au-Si model. Therefore, further ex-situ analysis of the growth nucleation process as well as particle composition could elucidate the growth dynamics in this case. Analyzing the post-growth composition of Ni-catalyzed GaP NWs and the growth temperature window, we provide in chapter 5 a first attempt in understanding the growth process in this case.
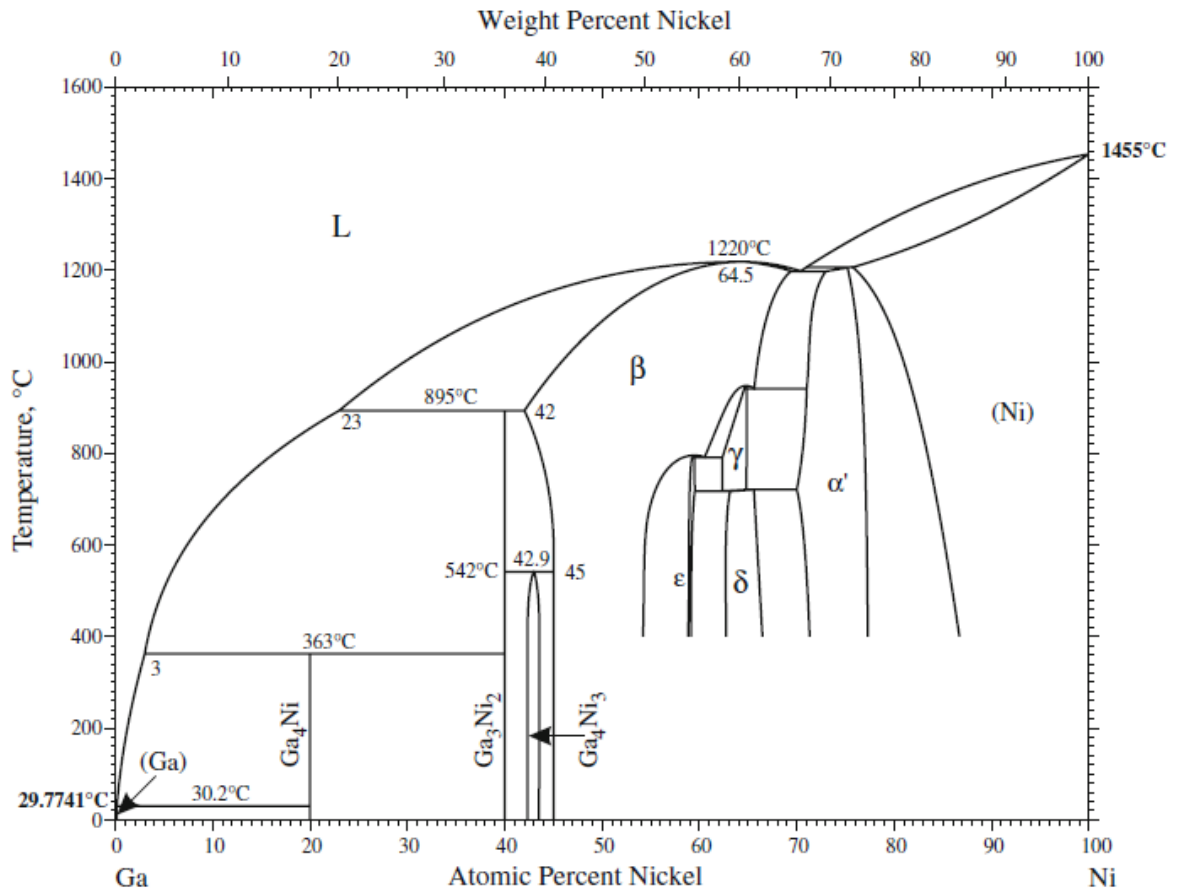
Figure 2.7 – (b) Phase diagram of the Ni-Ga system [78].

2.3 Structural properties of III-V nanowires

Most III-V compound semiconductors assume the Zinc Blend (ZB) crystal structure from the cubic system in bulk or thin film forms, Fig. 2.8a. On the other hand, the Wurtzite (WZ) phase, from the hexagonal system, can be obtained for nanowires, Fig. 2.8b.
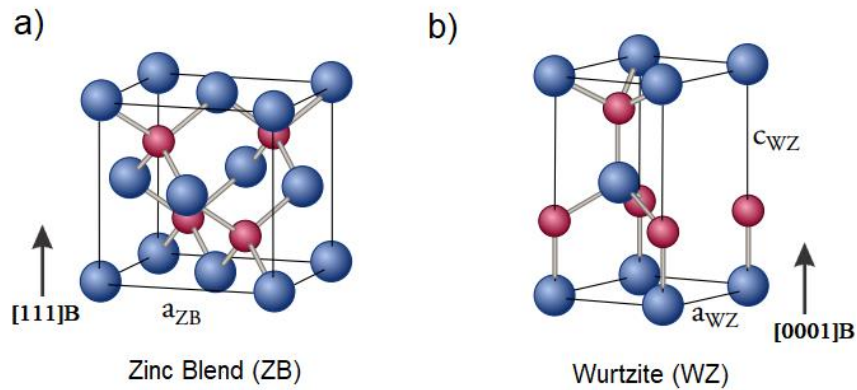
Figure 2.8 – (a) Representation of the Zinc Blend (ZB) crystal structure. (b) Representation of Wurtzite crystal structure, extracted from [79].

The ZB structure can be described by a fcc lattice with base composed of different atoms in the positions: group III in (0, 0, 0) and group V in (1/4, 1/4, 1/4), Fig 2.8a. Wurtzite is a structure of the hexagonal system, which can be described by a simple hexagonal lattice with base formed by atoms in the following positions: group III_1 (0, 0, 0), group III_2 (2/3, 1/3, 1/2), group V_1 (0, 0, u), group V_2 (2/3, 1/3, u + 1/2), where u = 8/3, Fig. 2.8b.

These two structures are similar when the crystal is stacked in the equivalent [111]B and [0001]B directions for ZB and WZ, respectively. III-V nanowires usually grow in these crystallographic directions, with stacking order αβαβαβ … for WZ and αβγαβγαβγ … for ZB, where each layer contains the two elements, as represented in Fig. 2.9 [80]. The energy difference for the formation of a new layer in these two cases is very small, hence, extended defects are easily generated, such as stacking faults [80].

During growth, the nanowires usually expose lower surface energy crystallographic facets, in order to minimize the total free Gibs energy of the system. Depending on the characteristic facets exposed, different Vapor-Solid (VS) growth rates can take place. The Wurtzite structure is non-centrosymmetric, which means that it does not contain an inversion center as one of the its symmetry elements. Thus, the WZ surface can be polar, depending on the crystallographic direction. In the example illustrated in Fig. 2.9b, <0001>-oriented WZ structures present polar facets, as the perpendicular planes {0001}, i.e., (0001)A and (0001)B, which have distinct atomic termination in the opposite directions across <0001>. The polar planes with group III and V terminations are named as "A" and "B", respectively. On the other hand, {1-100} planes present the same atomic termination in all equivalent directions, Fig. 2.9b. In this case, the apolar set of planes should exhibit similar VS growth rates.
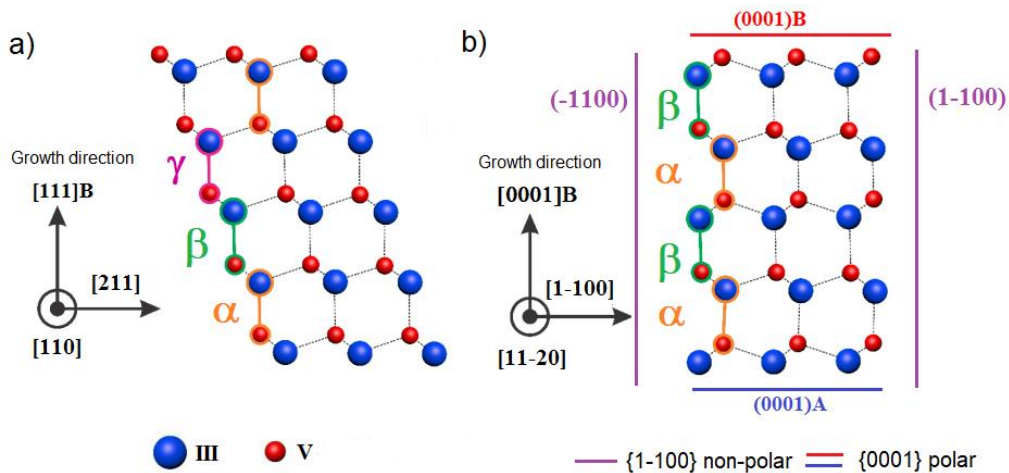
Figure 2.9 – (a) Characteristic αβγαβγαβγ... stacking of ZB in the direction [111]B. (b) Characteristic αβαβ ... stacking of WZ in the direction [0001]B. Apolar planes of the {1-100} family are highlighted in purple, and the polar planes of the {0001} family are shown in red and blue. Adapted from [81].

2.4 Nanowire Characterization

An initial evaluation of the sample (morphology, population distribution, yield and etc) is always necessary, as a screening step to eventually achieve optimized growth conditions. For that goal we have first performed scanning electron microscopy (SEM), and after that, transmission electron microscopy (TEM) and related techniques was used to access the crystal structure and the chemical composition. The distribution of nanoparticles and morphology on the substrate were analyzed using Atomic Force Microscopy (AFM). The optical properties and structural information were investigated by photoluminescence (PL), photoluminescence excitation (PLE) and Raman spectroscopy.

2.4.1 Scanning Electron Microscopy

Morphological analyses and the first inspection after growth were performed using scanning electron microscopy (SEM), which is a routine technique to investigate materials at micro and nanoscale. In SEM the sample is probed by a focused electron beam, controlled by eletromagnetic lenses, as illustrated in Fig. 2.10a. Using field-emission electron guns, with higher brightness, the resolution of SEM can reach a few nm (1-3 nm). When the high energy, focused electron beam hits the sample, different signals are generated as X-rays, Auger electrons, Backscattering electrons and secondary electrons (SE), as illustrated in Fig. 2.10b.
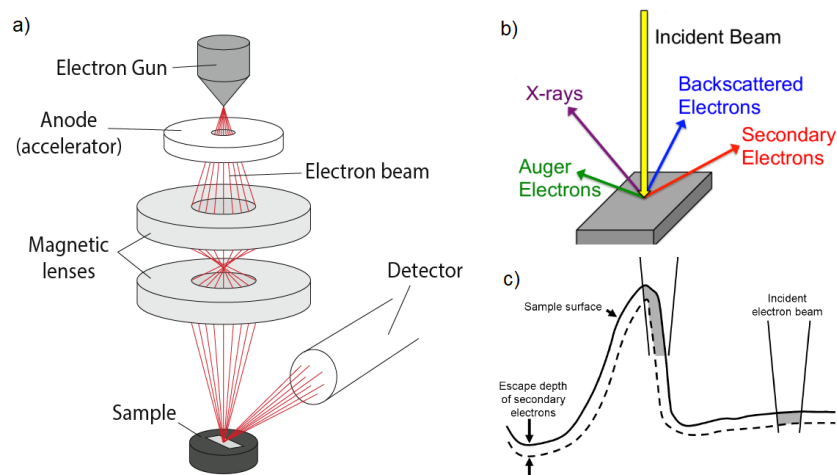
Figure 2.10 – (a) Scheme illustrating the components of a scanning electron microscope (SEM), extracted from reference [82]. (b) Illustration of the main signal generated in the interaction of the focused high energy electron beam and the sample, extracted from [83]. (c) Illustration of the influence of sample topography in the secondary electron extraction, extracted from [84].

Chemical analysis can be carried out by detecting the characteristics X-rays from the sample. SEM images can be formed by scanning the sample surface point-to-point and detecting a specific signal such as, for example, the secondary electrons (electrons with energy ≤ 50 eV). This signal is very sensitive to the topography of the sample, due to the low escape depth (< 5 nm), as illustrated in Fig. 2.10c. Thus, a gradient in the SE signal can be produced due the morphological changes in the sample, with more SE detected in areas with high curvature rather than in flat surfaces on the sample, Fig. 2.10c; the different contrasts along the sample generate the SEM image. More about this tehnique can be found elsewhere [85].

SEM is an easy and fast characterization technique, and the only requirement for the sample is to be conductive, as well as stable in the vacuum enviroment inside the microscope. This is important in order to avoid charging effects when the electron beam is focused on the sample surface. If the sample is non-conducting, a very thin gold film can be deposited on the sample, or a conductive tape can be used to reduce the charging on the sample. For our III-V nanowires, no special sample preparation was needed.

In this work we used electron microscopes from the Eletron Microscopy Laboratory of the Brazilian National Nanotechnology Laboratory (LNNano), located in the Brazilian National Center for Research in Energy and Materials (CNPEM) and the Laboratory of Structural Characterization (LCS) from the Federal University of São Carlos (UFSCAR). The used equipment is listed below:

- SEM FEI FEG-Inspect F50, operated in the range $2 - 20$ kV, using the secondary electron detector (at LNNano);

- SEM Philips XL30, operated at 10 kV, using the secondary electron detector (at UFSCar).

2.4.2 Transmission Electron Microscopy

Transmission electron microscopy is a powerful tecnique to analyze many aspects of nanomaterials such as morphology, crystal struture and chemical composition. TEM uses a electron beam controlled by electromagnetic lenses to iluminate a very thin sample (usually less than 100 nm), Fig. 2.11. The sample needs to be thin because electrons are easily scattered [86]. Thus, nanomaterials as nanowires usually do not need special preparation for TEM measurements due to their reduced dimensions.
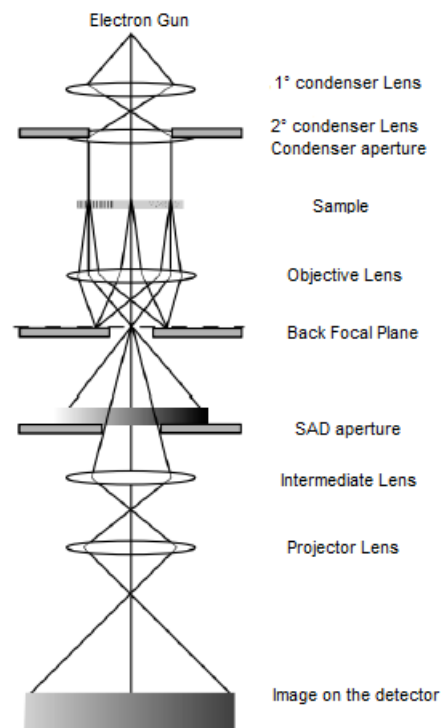
Figure 2.11 – Scheme illustrating the components of a transmission electron microscope (TEM), extracted from the reference [87].

Images in TEM can be formed by illuminating the sample with a parallel beam with the incoming electrons in phase; if the sample is in zone axis, i.e., oriented in a specific crystal orientation where the interatomic distances are higher than the resolution of the microscope, (usually in the order of Å or less), High Resolution Transmission Electron Microscopy (HRTEM) images can be obtained for crystaline materials. In this case, the change in the eletron phase due to the interaction with the periodic potential of the material lattice generates a phase contrast image with atomic resolution. Although HRTEM images are not easily interpreted, they can be used to identify nanowire crystal structure and characteristic stacking sequences for the WZ and ZB crystal phases. Thus, extended crystal defects as stacking faults or insertions of one phase into another along the III-V NW structure can be easily identified.

In a different configuration, Scanning Transmission Electron Microscopy (STEM), the sample is scanned by a convergent electron beam; the transmitted electrons are measured using an annular detector located below the sample. Different images can be formed as, for example, High Angle Annular Dark Field (HAADF). Unlike the phase-contrast HRTEM images, in HAADF images the contrast is generated due to Rutherford scattering, i.e., the electron interaction with atomic nuclei in the material. Hence, HAADF images are interesting because the contrast is related to the atomic number, i.e., the interface between different

materials can be easily identified. Furthermore, HAADF images can also reach atomic resolution, depending on the microscope [86].

Structural information can also be obtained in a TEM by electron diffraction. If a sufficiently thin sample is in zone axis and illuminated with a parallel (in phase) electron beam, the electrons will be diffracted, forming a pattern in the back focal plane of the objective lens; this pattern contains crystallographic information about the material. One of the greatest benefits of performing diffraction in a TEM is that the crystallographic information can be accessed with spatial resolution, in an specific area of the sample, which is called Selected Area Electron Diffraction (SAED) [86].

Furthermore, chemical analysis is possible in a TEM by measuring the specific X-rays generated in the sample due to the interaction with the high energy electron beam, which is called Energy Dispersive X-ray Spectroscopy, or EDS. The number of photons at a specific energy obtained in an EDS measurement follows Poissonian statistics; therefore, the uncertainty in the number of counted photons of a characteristic X-ray peak is [86]:

$$u = \frac{3\sqrt{N}}{N} \, 100\% \, , \quad (eq. \, 2.3)$$

where N is the number of counts related to the peak. Moreover, a detected peak can be considered reliable if the number of counted photons, i.e., the integrated intensity ($I_{peak} = N$) exceeds the background uncertainty, i.e., $I_{peak} > 3\sigma_{background} = 3\sqrt{\mathbb{N}_{background}}$, where $\mathbb{N}_{background}$ is the counts of the background. In this work, we have used the TEM FEI Titan, equipped with a field emission electron gun and spherical aberration corrector, allowing sub-angstrom resolution. In addition, the Titan has four Si drift detectors (SDD) arranged around the sample, providing a larger solid angle for the collection of characteristic X-rays, and therefore lower exposure times for photon counting, minimizing sample damage. These features allowed us to perform chemical analysis of very small catalyst particles (d $\leq$ 10 nm), as discussed in chapter 5. More about TEM analysis can be found elsewhere [86].

For this work we have mechanically transferred the GaP and GaAs nanowires from the as-grown substrate to Ted Pella carbon grids. The analyses were performed in the following equipment, operated by the author, in the Eletron Microscopy Laboratory of the Brazilian National Nanotechnology Laboratory (LNNano), located in the Brazilian National Center for Research in Energy and Materials (CNPEM):

- TEM JEOL2100, with a LaB_6 electron gun, operated at 200 kV in conventional TEM mode;

- TEM JEM2100F, with a field emission electron gun, operated at 200 kV in conventional TEM mode;

- TEM FEI spherical aberration-corrected Titan Cubed Themis with field emission electron gun, operated at 80 kV and 300 kV in the conventional and STEM modes.

2.4.3 Atomic Force Microscopy

The spatial distribution of nanoparticles and morphology on the substrate surface were analyzed using Atomic Force Microscopy (AFM), Fig. 2.12. This technique monitors surface morphologies using a cantilever, in which a very thin tip with nanometer-sized radius is mounted, and piezoelectric scanners; the cantilever deflection (Fig. 2.12a), resulting from the interaction between tip and surface (Fig. 2.12b), can be measured, providing the corresponding force. As the tip is scanned along the surface of the sample, a servo feedback loop maintains the force constant by actuating the z-movement of the scanner. The topography of the sample surface can be thus obtained, as shown in Fig. 2.12a. Different AFM modes depend on the interaction used to detect the signal used for the feedback loop and how the scan is performed. In this work, we used the non-contact mode, where the cantilever oscillates in a resonance frequency and changes in the cantilever amplitude, due to sample interaction, are monitored. Non-contact mode (tapping mode) prevents damage to the sample since weaker forces are involved (Fig. 2.12b). More details about AFM-related techniques can be found elsewhere [88].
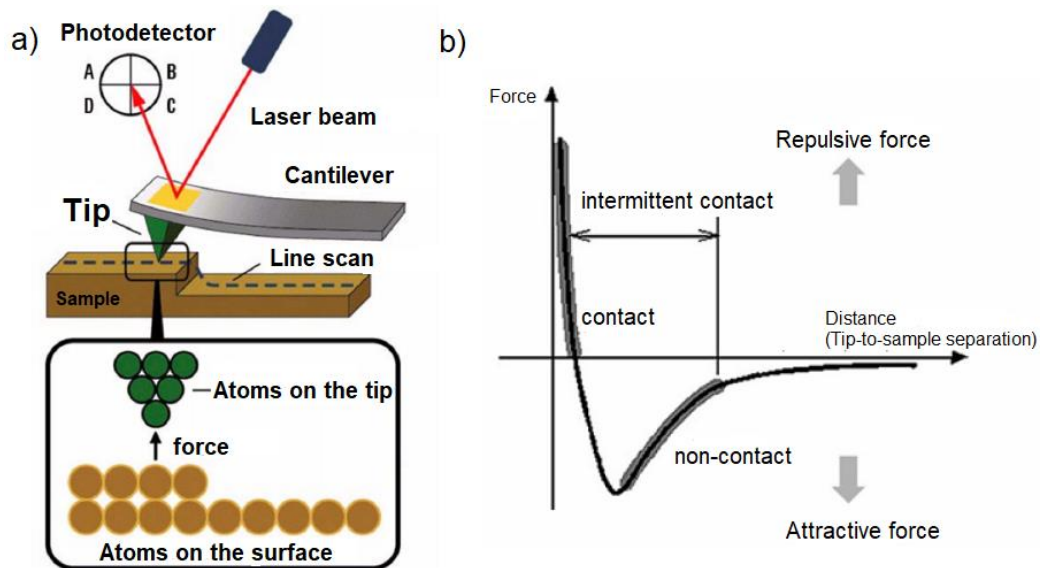
Figure 2.12 – (a) Schematic representation of an Atomic Force Microscopy (AFM) microscope [89] (b) Lennard Jones model for the potential of the interaction between the tip and the sample, also showing the different modes of operation of the AFM as a function of the separation between them [90].

The measurements in this work were acquired in air with Keysight model 5500 equipment operating in noncontact mode with conical Si tips.

2.4.4 Optical Spectroscopy setup

Optical characterization of the ensemble of the nanowires was carried out by macro photoluminescence (macro-PL) and photoluminescence excitation (macro-PLE) spectroscopy at low temperature (10 K). The optical setup used for the measurements is illustrated in Fig. 2.13. For macro-PL experiments a 405 nm diode laser was used as excitation source and for macro-PLE experiments, a Xenon lamp coupled to a 0.32 m single monochromator (iHR320, Horiba) was used as excitation light. The output spectral response of the PLE excitation source (Xe lamp) was detected using a lock-in amplifier and a piroelectric detector to correct the PLE spectra measured for the NWs. The luminescence detection, in both cases, were performed by a 0.75 m double monochromator with 1200 gr/mm grating (SPEX) and a GaAs-cathode photomultiplier (PMT) (Hamamatsu - cooled with peltier). The current from the PMT was amplified by a Keithley Digital Electrometer (617). A helium (He) cold-finger cryostat (Oxford) was used to reach cryogenic temperatures and the temperature was setup by a PID temperature controller with a heating filament.
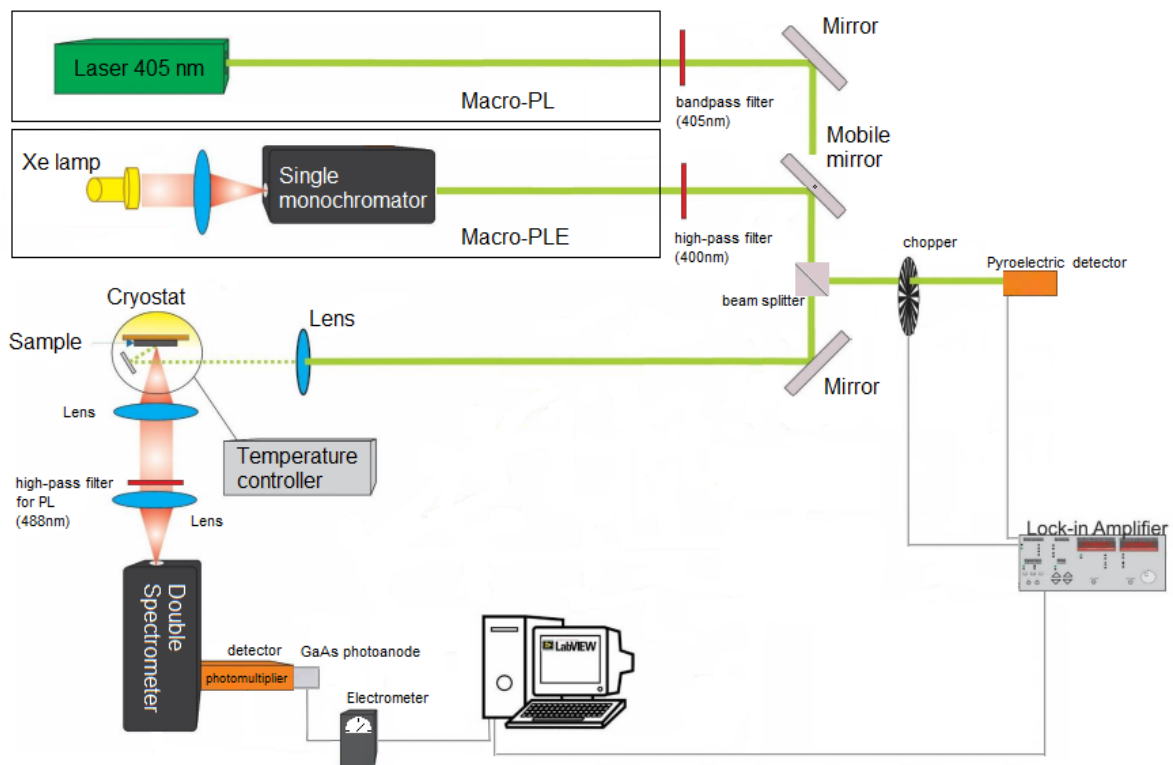
Figure 2.13 – Schematic representation of the optical setup used for macro-PLE and macro-PL measurements, adapted from [91].

Single nanowires optical analyses were done by micro-photoluminescence (μ-PL) at low temperature and Micro-Raman (μ-Raman) spectroscopy at room temperature, using the optical setup illustrated in Fig. 2.14. In both μ-PL and μ-Raman analysis, the micro-sized GaP structures were transferred to a Si/SiO_2 substrate. The μ-Raman and the μ-PL measurements, were performed in the backscattering geometry with a 50X (laser spot diameter of ~ 2 μm) objective lens and a solid state laser emitting at 488 nm used as excitation source. The signals were detected by a Si CCD camera and a single (Jobin Yvon, T64000) monochromator with 600 (1800) gr/mm grating. A helium (He) cold-finger microscope cryostat was used to reach cryogenic temperatures and the temperature was setup by a PID temperature controller with a heating filament. Using micropositioners (Newport), with a step motor in each XYZ axis, it was possible to control the focus (Z axis) as well as the laser spot position on the nanowires (X and Y axis), as illustrated in Fig. 2.14.
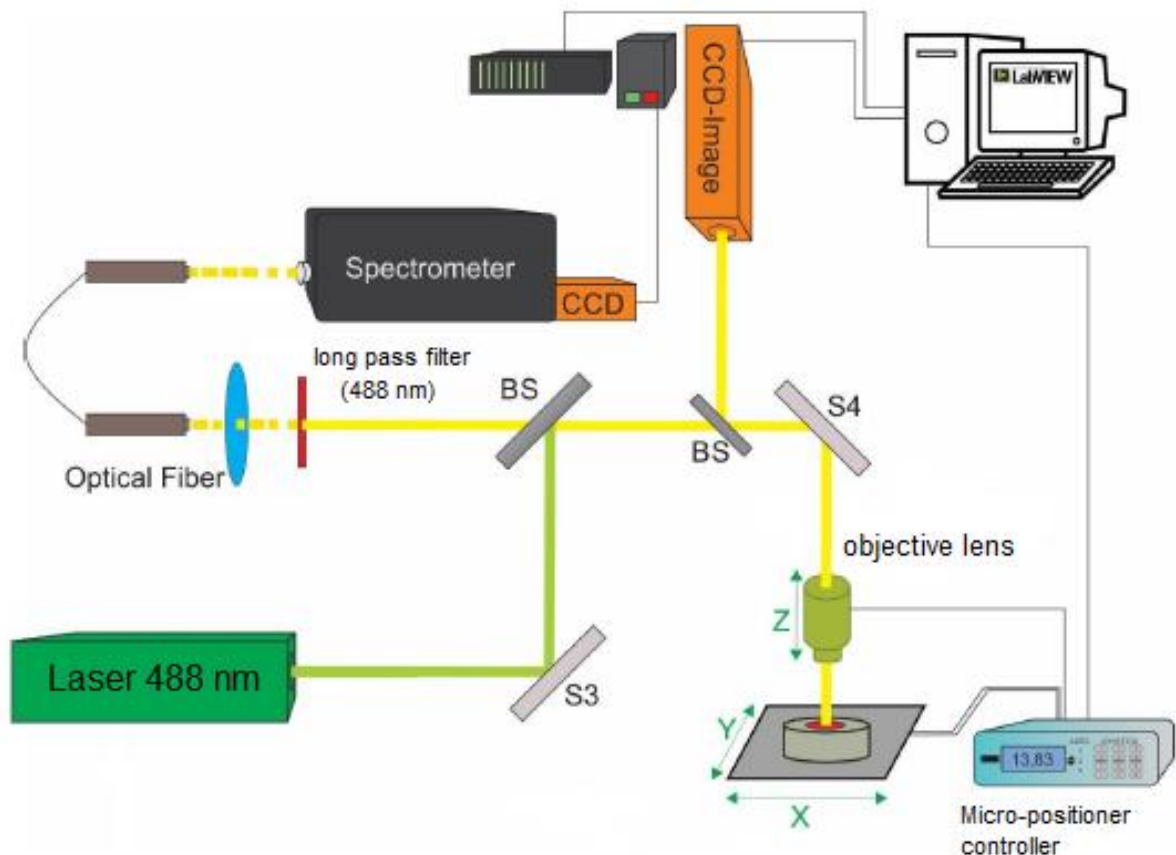
Figure 2.14 – Schematic representation of optical setup used for micro-PL and micro-Raman measurements, adapted from [91].

2.4.4.1 Photoluminescence (PL) and Photoluminescence Excitation Spectroscopy (PLE)

Photoluminescence Excitation Spectroscopy (PLE) is a technique where the photoluminescence of a material is monitored at an specific energy and the excitation energy is varied. The optical emission intensity, $I_{emission}$, depends on the carriers population and the probability (rate) of emission. The emission can be from fundamental gap (electron-hole, i.e., electron in the conduction band and hole in the valence band) recombination and can also involve impurities or defects states. The carriers population depends on the different components as the probability of absorption (P_{abs}) and probability of relaxation to a specific state, i.e., thermalization (P_{rel}). Therefore, if the optical absorption occurs in a resonance condition involving excited states the carriers population increases; consequently, the emission intensity also increases. Since the carrier relaxation in semiconductors is dominated by phonon scattering, which occurs in a time scale of pico-seconds (much shorter than the emission time, over hundreds pico-seconds), the emission intensity is practically dependent only on the absorption process. Therefore, the PLE spectra reflects the absorption spectra, i.e., the joint of optical density of states [3].

Let us use parabolic bands in a direct gap semiconductor as an example. All photo-excited electrons at high energy are quickly thermalized (we assume here that the non-radiative channel is absent) to the bottom of the conduction band (hole also thermalizes to the top of the valence band) and both carriers recombine. The density of states in bulk, in three-dimensional (3D) systems, is proportional to the root-square of the energy. For each singularity of the joint density of states we have an additional feature. Fig. 2.15 (right panel) shows the typical PLE spectra involving three bands transitions, detecting at the fundamental gap emission.

In addition, in order to supress the intensity variation with energy of the excitation source, in our case a Xe lamp, we have corrected the PLE spectrum by using its ratio with the Xe lamp spectrum. Thus, we can directly correlate the PLE intensity to the optical absorption edges of the WZ GaP nanowires.
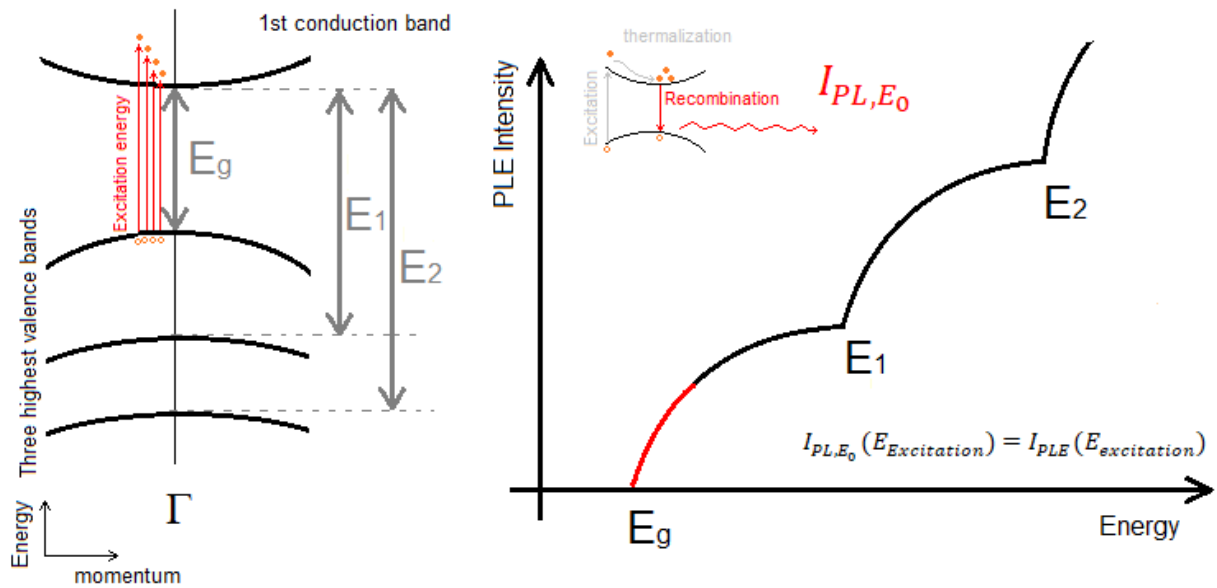
Figure 2.15 – Illustration of the eletronic band structure in a direct band gap semiconductor and the schematic representation of a PLE spectrum. The three lowest energy transitions lead to the threshold observed in PLE.

2.4.4.2 Raman Spectroscopy

Raman spectrosccopy is a non-invasive and very useful technnique to probe the lattice vibrational modes (phonons) of materials, their frequency and also symmetry. Due to the vibration symmetry of the phonons, different modes can be selected by changing the crystal orientation and incident and scattered light directions, as well as the polarization. Hence, crystal structure can be easily probed by Raman polarized measurements. Moreover, it is possible to identify the chemical bonds present, in the case of molecules.

In the Raman measurements, the sample is illuminated with a focused ligh source and then, the light is scattered, as illustrated in Fig. 2.16. A large portion of the light suffers elastic scattering, known as Rayleigh scattering. However, a small fraction of the light is inelastically scattered by the crystal, producing the well known Stokes and anti-Stokes modes, Fig. 2.16.
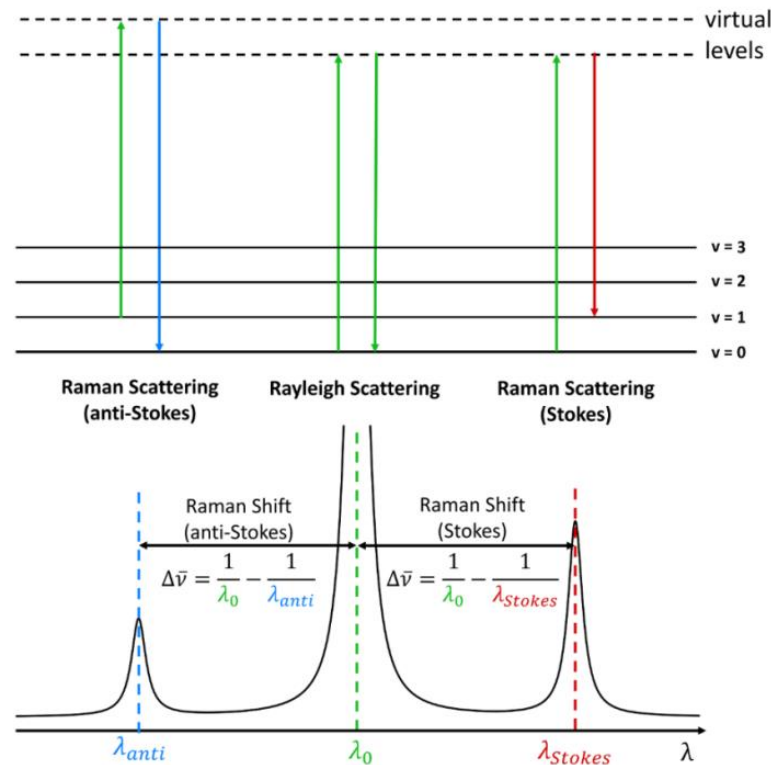
Figure 2.16 – Schematic vibration energy diagram and the Raman scattering spectrum. The top panel shows the photon energies involved in the Stokes and anti-Stokes modes. The bottom panel shows the Raman scattering intensity versus wavelength of the radiation. Extracted from [92].

Raman experiments usually display results in terms of Raman shift, as defined in eq. 2.4, which is the difference between the incident and scattered light frequency, $\Delta\omega$, but in most cases the wavenumber (inverse of the wavelength and proportional to the frequency) is used in cm^{-1} unit:

$$\Delta\omega = \omega_{incident} - \omega_{scattered} . \quad (eq.\,2.4)$$

In the anti-Stokes modes the phonons or molecules are already in a high energy vibration state and, after light scattering, return to a lower state, leading to a higher energy inelastic light scattering, see left side peak in Fig. 2.16 (note that the x-axis is wavelength). On the other hand, the Stokes modes are the inverse, phonons or molecules are in ground states and are promoted to a higher energy states, leading to a scattered light to lower energy than the incident light source, see right side peak in Fig. 2.16. Since the lower states are much more populated when the system is in thermodynamical equilibrium, the Stokes modes are stronger than the anti-Stokes.
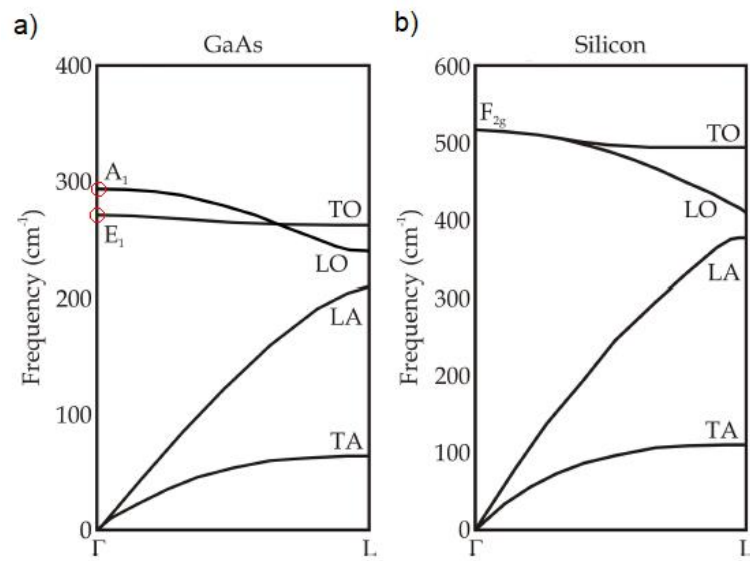
Figure 2.17 – Phonon dispersion in Zinc Blende Crystal Structure-based material. In (a) GaAs and (b) Si. Extracted from [93].

In a crystal, the vibrational modes can be classified according to the directions of the atoms oscillation and their vibration between each other relative to the wave propagation. Figure 2.17 shows the phonon dispersion in ZB semiconductors. There are 3 vibrational modes associated with acoustic modes (low frequency), where two are transverse and one longitudinal, namely as TA and LA, respectively. Acoustic phonons are vibrational modes where nearest neighbor pair atoms move in the same direction and in phase. Hence, there is no change in the polarization in the unit cell and they do not interact with light. The acoustic branch has a linear relationship with the wavevetor k, close the Γ point ($\omega \rightarrow 0$, when $k \rightarrow 0$), as can be seen in Fig. 2.17. In contrast, in optical phonon modes neighbouring atoms move in opposite directions, leading to a change in the dipole moment, and the interaction with light. Thus, these modes only exist when we have more than one atom per unit cell. They can be observed in Raman scattering, as well as in infrared spectroscopy, where their selection rules are different.

The optical modes can be longitudinal (LO) (group theory A_1) and transverse (TO) (group theory E_1), and depend on the number of atoms in the primitive cell. The total of modes in a crystal with N atoms in a primitive cell is $3N - 3$. The phonon dispersion for a single atom in the primitive cell (Si) and a double atom in the primitive cell (GaAs) is displayed in Fig. 2.17.

In this thesis, we have measured the Raman spectrum in the backscattering geometry. Thus, the scattered light is detected in the opposite direction where the excitation source comes from, resulting in a momentum transfer to the phonon in the same direction. The

transferred momentun is ~ 2k$_{inc}$, where k$_{inc}$ is the photon momentum of the incident light which is 2π/λ$_{inc}$. Since λ$_{inc}$ (the incident light wavelength) is, in most cases, in the visible spectral range, then k$_{inc}$ << π/a$_{lattice}$ (approximately edge of the Brillouin zone), where a$_{lattice}$ is the lattice parameter; this means that the k-vector of the phonon is, k ~ 0, practically at the center of the Brillouin zone, i.e., at the Γ point, see, e.g., highlighted modes in Fig. 2.17a, A$_1$ and E$_1$ modes of GaAs.

The Raman intensity depends on the Raman tensor, according the following relation [3]:

$$I_{Raman} \sim \omega^4 |\hat{e}_i \cdot \mathcal{R} \cdot \hat{e}_s|^2 , \quad (eq.\ 2.5)$$

where ω is the frequency of the scattered light, $\hat{e}_i$ and $\hat{e}_s$ are the polarization directions of the incident and scattered lights, respectively. $\mathcal{R}$ is the Raman scattering tensor and is related to the crystal symmetry. Using polarized incident light and selecting the polarizarization of the scattered light, we can select some elements of $\mathcal{R}$, i.e., determine the Raman selection rules. Thus, it is possible to determine specific vibrational lattice modes using specific scattering geometries and light polarization measurements. The allowed modes for each Raman configuration in WZ crystals is described elsewhere [94, 95]. We have used these type of measurements in order to probe specific vibrational modes in the WZ GaP.

The active vibration modes in Raman scattering for Wurtzite crystals are well known, using group theory, they are A$_1$, E$_1$ and E$_2$ [96]. In A$_1$, the motion of the atoms in the unit cell lies in the z axis and E$_1$ is polarized in the xy plane; both are optical phonons. Two E$_2$ modes are E_2^L and E_2^H (L for low frequency and H for high frequency). The nomenclature displayed here is related to group theory [3].

Recently, Benyhaia et al. [97] have calculated the phonon dispersion for the WZ phase of GaP, shown in Fig. 2.18. Some of the Raman allowed modes are the E_2^L at 76 cm^{-1}, E_2^H at 358 cm^{-1}, $A_1(LO)$ at 413 cm^{-1}, $A_1(TO)$ at 361 cm^{-1}, $E_1(LO)$ at 393 cm^{-1}, $E_1(TO)$ at 366 cm^{-1}. The E_2^L is only observed in WZ crystals and is absent in the Zinc Blend case. Thus, it can be used to probe the crystal structure and differentiate ZB from WZ phases.
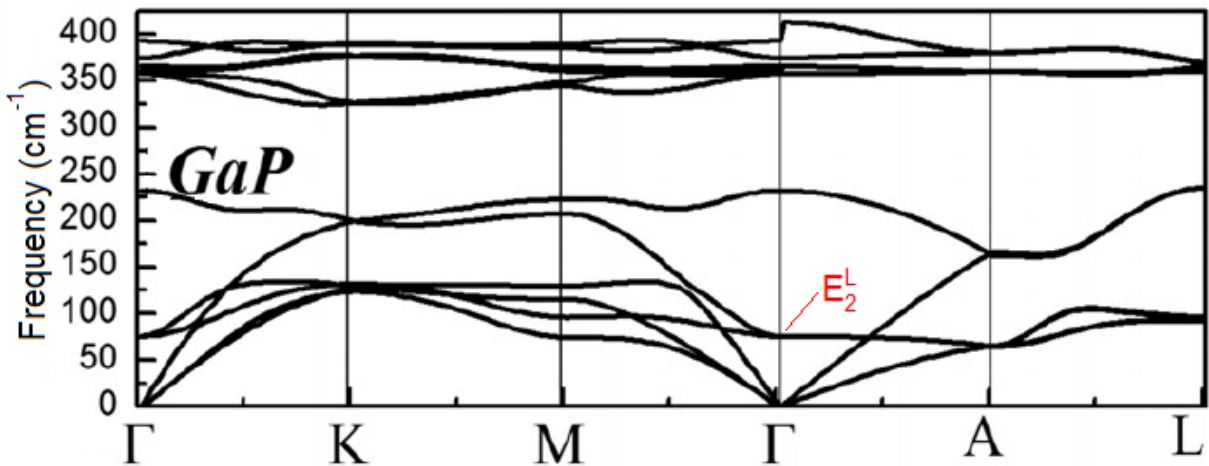
Figure 2.18 – Calculated phonon dispersion WZ GaP. The E_2^L vibrational mode at 76 cm^{-1} is highlighted. Figure extracted from [97].

2.5 Electronic band structure of WZ Gallium Phosphide, oscillator strength and transition matrix element

The electronic band structure of a material provides the energy dispersion of the electrons in the solid, thus the possible allowed optical transitions. However, it is important to account for the probability of each eletronic transition, which is related to the crystal symmetry as well as to the selection rules derived from the symmetry of the eletronic wavefunctions in the conduction and valence bands.

The optical absorption is a quantum mechanical phenomenon can be described by the first order time-dependent approximation theory, which is the Fermi's golden rule [4]:

$$W_{i \to f} = \frac{2\pi}{\hbar} |\langle f|H_{ext}|i\rangle|^2 \delta(E_f - E_i). \quad (eq.\,2.6)$$

This equation describes the transition rate probability (probability per unit of time) of a specific eletronic transition involving the states i and f, $W_{i \to f}$, for example in an absorption experiment. $|\langle f|H_{ext}|i\rangle|$ is the electric dipole transition matrix element between the initial i and final f states. This term gives us the selection rule, for example, the angular momentum conservation, i.e., the angular momentum variation is $\Delta j = 0, \pm 1$ of the photon, wavevector conservation, etc. The perturbative Hamiltonian can be considered in the dipole approximation as $H_{ext} = \boldsymbol{p} \cdot \boldsymbol{E}$, where $\boldsymbol{E}$ is the external eletromagnetic field and $\boldsymbol{p} = q\boldsymbol{r}$ the linear momentum. The equation 2.6 can be rewritten in terms of $|\langle f|\boldsymbol{p}|i\rangle|^2 = |p_{fi}|^2(\boldsymbol{k})$, which is known as the transition dipole momentum.

In spectroscopy, the integrated intensity (strength) of specific absorption peaks (edges) are treated using the oscillator strength f, which is a dimensionless quantity that expresses the probability of that transition to occur and is related to the quantum mechanical treatment by the expression [4]:

$$f = \frac{e^2}{\varepsilon_0 m \omega_{21}^2} \frac{2|\langle f|\boldsymbol{p}|i\rangle|^2}{m\hbar\omega_{21}} \quad . \quad (eq. \, 2.7)$$

$|p_{fi}|^2(\boldsymbol{k})$ depends on the symmetry of the valence and conduction wavefunctions involved in the transition.
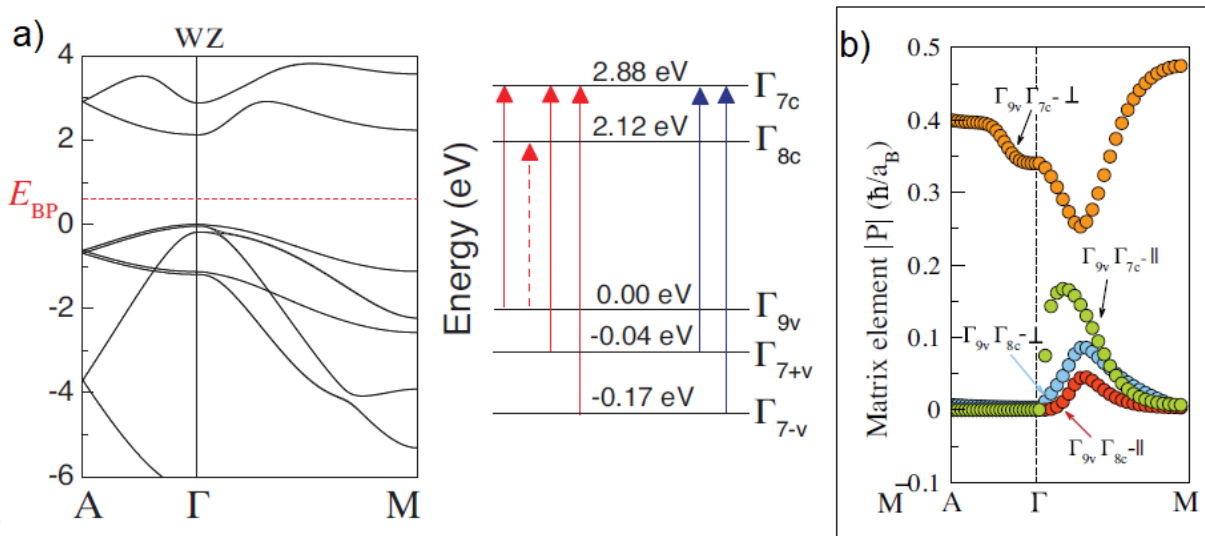
Figure 2.19 – (a) The eletronic band structure of WZ GaP calculated by Belabbes and Bechstedt and the labeled bands, the three highest valence bands Γ_{7v-}, Γ_{7v+}, Γ_{9v} and the two lowest conduction bands Γ_{8c} and Γ_{7c}, respectively. (b) Optical transition strength (matrix element moment) of the lowest eletronic transitions. Extracted from [54].

Recently, Belabbes and Bechstedt [54] have reported the calculation results of the electronic band structure of WZ GaP, Fig. 2.19a, and the optical transition strength of the lowest eletronic transitions in WZ GaP, Fig. 2.19b. These authors have predicted a direct band gap for the hexagonal phase with the fundamental band gap at 2.12 eV, Fig. 2.19a. Moreover, the fundamental eletronic transition, involving the bands Γ_{9v} and Γ_{8c} according to the label for the bands provided by Belabbes and Bechstedt [54], is almost forbidden, with very low probability at the Γ point. Therefore, in this case, WZ GaP has a dipole forbidden fundamental eletronic transition, i.e., it is a so-called pseudo-direct band gap semiconductor. This should lead to weak band-to-band absorption and emission, as weak as an indirect bang gap semiconductor.

2.6 Absorption in semiconductors: probing the band gap

Absorption measurements in semiconductors is a useful technique to probe the eletronic structure as well as determine the band gap of these materials. Measuring the absorption edges provides the eletronic transitions close to the band gap. Depending on the characteristic eletronic band structure - direct, indirect, dipole-forbidden (pseudo-direct) - the absorption response is different. The negligible linear momentum of a photon leads to eletronic transitions to occur at the same **k** in eletronic band structure. Thus, dipole-allowed direct band gap semiconductors have naturally the lowest energy transition at same **k**, resulting in an short lifetime and high probability of radiative transition.

In Fig. 2.20 we can see the optical absorption of GaAs, which is a classical direct band gap semiconductor ($E_g = 1.52$ eV).
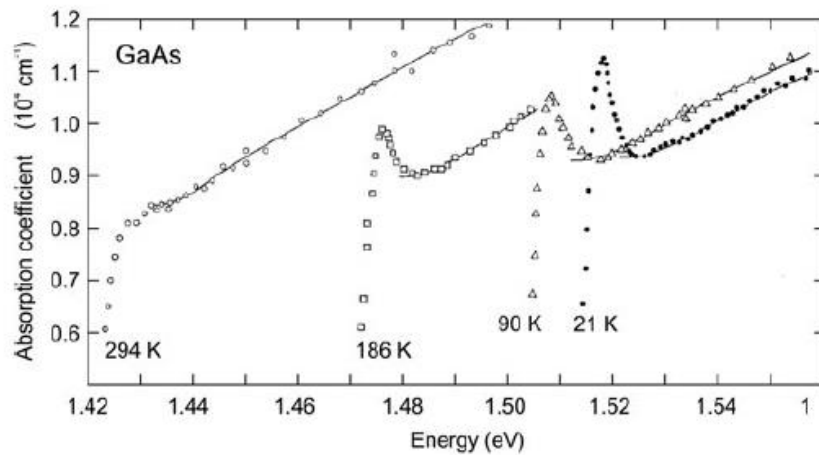
Figure 2.20 – Optical absorption for GaAs at different temperatures, extracted from [4].

At low temperature, excitonic (electron-hole interaction) peaks in the absorption appear in dipole-allowed direct band gap materials, as shown in Fig. 2.20. They present a characteristic, abrupt threshold and a strong increase in absorption, characterized by a curve growing with the square-root of energy, as [3, 2]:

$$\alpha \sim \left(h\nu - E_g\right)^{1/2}. \quad (eq.\,2.8)$$

On the other hand, indirect band gap semiconductors present a different behaviour. The fundamental transitions have to be assisted by a phonon in order to conserve momentum, since a change in **k** is needed. This leads to an increase in absorption according to [3, 2]:

$$\alpha \sim \left(h\nu - E_g - E_p\right)^{2}, \quad (eq.\,2.9)$$

where E_p is the energy of the involved phonon. We can see in Fig. 2.21 the absorption spectrum at different temperatures for the indirect band gap semiconductor Si. Moreover, these two-particle process is less probable than the direct transition, resulting in a much weaker absorption, about 10^{-3} smaller than for their direct band gap counterparts.
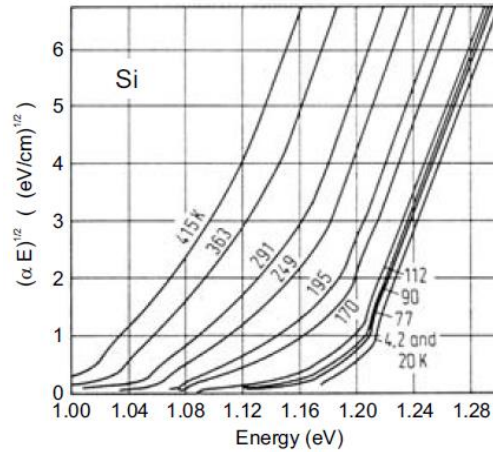
Figure 2.21 – Optical absorption for Si at different temperatures, extracted from [4].

Therefore, the optical absorption measurements can be used to identify the nature of the eletronic band structure of a new semiconductor material, since they have very different absorption responses, as illustrated in Fig. 2.22. This information is not possible to deduce directly from luminescence studies.
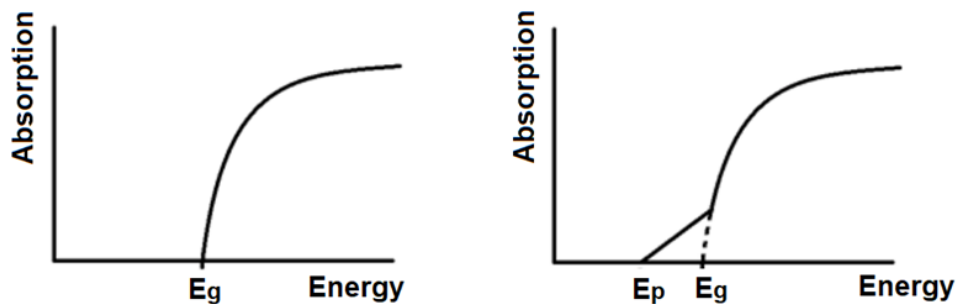
Figure 2.22 – Schematic representation of the optical absorption in a direct and indirect band gap semiconductor, respectively.

Furthermore, there is a third case, where the eletronic band structure results in a direct band gap, but the selection rules leads to a dipole-forbidden fundamental transition, due to the symmetry of the conduction and valence wavefunctions. In this case, the semiconductor is called a pseudo-direct band gap semiconductor. CuO_2 [3] and $ZnGeP_2$ [98] are typical examples. In this case, the absorption presents a different exponent, as [3, 2]:

$$\alpha \sim \left(h\nu - E_g\right)^{3/2}. \quad (eq.\,2.10)$$

In all three cases, ploting the absorption spectrum with the apropriate exponent α^n, depending on the nature of the band gap, a linear curve is obtained; by extrapolating the linear plot at $\alpha = 0$, we can determine the band gap value E_g. In addition, the features of the curve in the vicinity of the band gap can also be used to determine if the transition is direct, indirect or dipole-forbidden (pseudo-direct).

2.7 Excitons and impurity emissions in semiconductors

In a semiconductor there are different radiative recombination channels: the band-to-band recombination, where electrons from the conduction band recombine directly with holes in the valence band, as well as recombination mechanisms usually associated to different crystalline point defects and/or impurities formed by foreign atoms. Their behavior and corresponding effect on the eletronic band structure vary, depending on impurity type and its charge, donor or acceptor, for example. Acceptors generate excess of holes, as in p-type doped semiconductors. On the other hand, donors provide more electrons, leading to n-type doped semiconductors. Some possible impurity recombinations usually observed in semiconductors are shown in Fig. 2.23 [3, 2, 99].
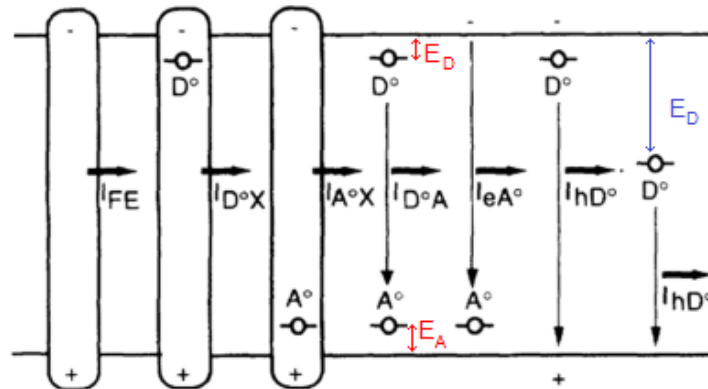
Figure 2.23 – Band diagram of some band-to-band and impurities eletronic transitions observed in semiconductors, adapted from [99].

One possible emission observed in semiconductors, which is not related to impurities, are the free-excitons (FE). This emission occurs in a slightly smaller energy than the band-to-band band gap recombination involving a free electron-hole pair. Excitons are quasi-particles attributed to the interaction between free electrons and holes in the semiconductor, which form a hidrogen-like state. Thus, in the Wannier-Mott picture for the exciton, the emission is observed in a smaller energy due to the binding energy of the exciton,

E_n^X, as the system can be treated as a hydrogen atom, with the dieletric constant of the material considered [3, 2]:

$$E_n^X = E_g - \frac{\mu e^4}{2\hbar^2 \varepsilon_0^2 \varepsilon_r^2} \frac{1}{n^2} , \quad (eq. \, 2.11)$$

where E_g is the band gap of the material, ε_0 permissivity in vacuum, ε_r permissivity of the material, $\hbar$ planck constant, e eletric charge, and $\mu = \frac{m_e m_h}{m_e + m_h}$ is the reduced effective mass (m_e and m_h are the electron and hole mass, respectively). Excitons usually have small binding energies and for most semiconductors are observed at low temperatures; for example, for WZ GaP the free exciton binding energy is predicted to be 17 meV and very small radius (2.3 nm) for the first exciton energy level [55].

Excitons can also interact with impurities in the semiconductor and form localized states in the real space; the bound excitons lead to emissions at smaller energies than for free-excitons [3, 2]:

$$E_n'^X = E_g - E_n^X - E_b^X , \quad (eq. \, 2.12)$$

where E_b^X is the binding energy of the exciton in the impurity. The bound exciton can be bound to a donor (D^0X) or an acceptor (A^0X), Fig. 2.23.

Other possible recombination channels are due to impurities, usually foreign atoms, but can also be point defects as vacancies, intersticials and anti-sites. Impurities can introduce states in the band gap of the semiconductor, which can be donors or acceptors - when ionized, electrons or holes are added to the crystal, respectively. They can recombine with a electron (or hole) from the conduction band (or valence band), forming the e-A^0 (or D^0-h) emission, as represented in Fig. 2.23. The impurities are characterized by their ionization energy, E_D or E_A, which is the energy required to promote the electron (or hole) from the impurity state to the conduction band (or valence band), Fig. 2.23. Each impurity has an specific ionization energy which can be used as a fingerprint to detect its presence in the material. In addition, the impurities states can be classified as deep levels, when the ionization energy $E_{A,D} \gg kT$ at room temperature, with $kT \sim 25 \, meV$ ($300 \, K$), as represented in blue in Fig. 2.23. Thus, at room temperature the impurities are not ionized and the recombination channel is still active. On the other hand, we can observe shallow levels when $E_{A,D}$ is of the same order of magnitude of the thermal energy, in red in Fig. 2.23. For deep and shallow impurities, the emission associated can be determined as [3, 2]:

$$E_{e-A} = E_g - E_A , \quad (eq.\,2.13)$$

$$E_{D-h} = E_g - E_D . \quad (eq.\,2.14)$$

Moreover, a transition between two impurity states can also take place, which is known as donor-acceptor pair (DAP). The emission occurs at a smaller energy than band-to impurity recombination, subtracting the ionization energy of the donor and the acceptor involved, as well as the Coulomb interaction between the ionized impurities [3, 2]:

$$E_{DAP} = E_g - (E_A - E_D) + \frac{e^2}{4\pi\varepsilon_0\varepsilon_r R} . \quad (eq.\,2.15)$$

DAP recombinations usually display a strong blue-shift (70 meV/decade for Mg forming acceptor and donors states in GaN) [100] when the excitation power is increased, since more impurities are ionized, reducing the distance between them, R, and increasing the Coulomb term, the last term in eq. 2.15.

Free-excitons or bound excitons are characterized by very narrow emission (usually with linewidth smaller than 1meV) [55, 57] and they do not present stronger energy shift with increasing excitation power. In addition, from the power dependent measurements, a phenomenological relation can be obtained in order to identify the nature of the emission [99]:

$$I_{PL} = P^n , \quad (eq.\,2.16)$$

where I_{PL} is the integrated PL intensity of the analyzed emission and P the excitation power. When $n \leq 1$ the emission is due to impurities, i.e., band-to-acceptor (donor-to-band), donor-acceptor pair and etc. On the other hand, for $n \geq 1$ the emission is usually excitonic (free-exciton, bound exciton and etc).

Chapter 3

Exploring the growth dynamics of Au-catalyzed GaP nanowires synthetized by Vapor-Liquid-Solid mechanism

3.1 Introduction

Gallium Phosphide in the WZ phase (WZ GaP) has attracted attention of the semiconductor nanowire community due to the possibility of changing the electronic band structure, i.e., the optical properties, by modifying the atomic arrangement [40, 41, 53, 55]. The WZ phase is unstable; however, it can be easily obtained, depending on the growth conditions, when the synthesis occurs at the nanoscale, as a result of the high surface/volume ratio of the nanowires [80].

In the last years, the fabrication of devices from Au catalyzed III-V semiconductor nanowires has shown some drawbacks. For example, arrays of Au nanoparticles can be fabricated through EBL [101] or nanoimprinting [102], but uniformity and pattern fidelity have been difficult to achieve, depending on the growth conditions [101, 103]. Recently, instabilities of the Au particle on the III-V surface prior to growth, which can drastically affect sample quality, have been reported [103]. These instabilities arise specially due to the effect of annealing procedures, used to remove the native oxide layer prior to growth [59, 60, 65, 103].

In this chapter, we investigate the growth dynamics of asymmetric GaP NWs, continuing prior studies carried out in the group [61]. We show here the effect of Au nanoparticle instabilities on the III-V substrate surface for the formation of asymmetric WZ GaP nanowires, grown by chemical beam epitaxy. We discuss how the thermally activated Au NP crawling can alter the growth dynamics, leading to an unusual morphology, which has also high volume and is in the WZ crystal phase. The understanding of the mechanisms leading to these phenomena also implies in getting a better control of them. For that goal, we report the effect of varying growth conditions such as precursor flows and substrate temperature on the properties of WZ GaP NWs.

3.2 The growth procedure

GaP nanowires presented in this chapter were grown by chemical beam epitaxy using triethylgallium (TEG) and thermally cracked phosphine (PH₃) as precursors, as described in chapter 2. Different sizes of Au colloidal nanoparticles obtained commercially from Ted Pella were used to study the growth dynamics and the effect of nanoparticle crawling on GaP NW growth. We have used different growth substrates as epiready GaAs(100), GaAs(111)B and InP(100), but most of the samples were grown on GaAs(100) substrates.

3.3 Investigating the spontaneous motion of Au droplets on III-V surfaces

Currently, different authors have observed the motion of Au and Ga droplets on III-V surfaces and different mechanisms have been proposed to explain this phenomena. Ga droplet motion has been observed when the system is heated up above the congruent temperature, i.e., when group V atoms evaporate from the substrate at a higher rate than group III, leading to the formation of Ga droplets on the III-V surface [104, 105, 106, 107]. In the case of Au droplets, the driving force has been attributed to vacuum conditions [60] or the introduction of water vapor in the growth chamber during the heat step [59].

In order to investigate the effect of temperature on the droplet stability we have first performed thermal annealing on the samples. We deposited colloidal Au nanoparticles (20 nm and 50 nm in size) on GaAs(100) substrates and annealed in vacuum conditions ($P_{chamber} \sim 10^{-9}$ Torr) at different temperatures in the range 450 – 540 °C, for 5 min. We have also investigated the effect of AsH₃ overpressure during annealing. All the samples were cooled down under As₂ overpressure (13.0 sccm AsH₃ flow), Table 3.1.

Samples	AsH₃ (sccm)	Base Pressure (Torr)	Temperature (°C)	Au NP (nm)
A1	-	10^{-9}	450	20
A2	-	10^{-9}	480	20
A3	-	10^{-9}	510	20 and 50
A4	-	10^{-9}	540	20
A5	13.0	10^{-5}	510	20 and 50

Table 3.1 – Annealing conditions for the colloidal Au nanoparticles deposited on GaAs (100).

We have observed that for small Au NP's (20 nm) a trail form on the substrate surface in the ±[110] direction, when the annealing is carried out in vacuum, and above a specific temperature, 510 °C.
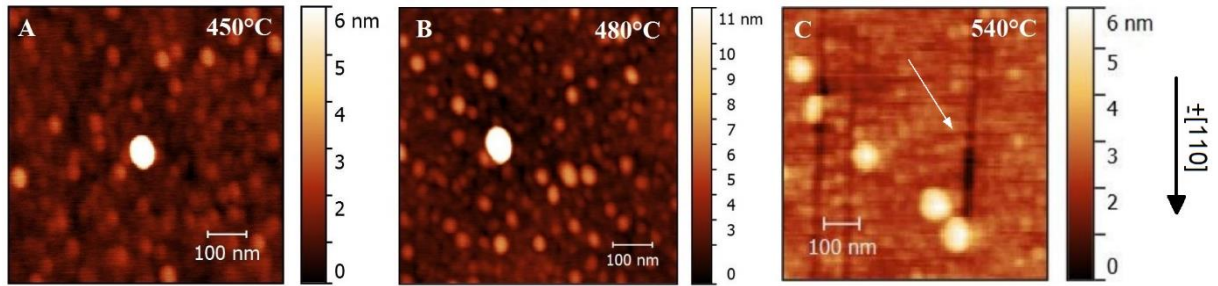
Figure 3.1 – Atomic Force Microscopy (AFM) of annealed samples in vacuum. Topography images of 20 nm Au nanoparticles on GaAs (100) substrates annealed at different temperatures. (a) 450 °C, (b) 480 °C, (c) 540 °C. In (c) the trail formed by the nanoparticles is highlighted with a white arrow, extracted from [65].

We show typical examples in Fig. 3.1A-C. This effect is also dependent on the nanoparticle size; for 50 nm Au nanoparticles, just a few and smaller droplets move across the substrate surface, also along ±[110] direction, not shown here. Thus, we do not observe the formation of a trail for the majority of the nanoparticles when small Au nanoparticles (d ≤ 20 nm) are used.

Next, we studied the effect of the gas phase on the annealed 20 nm Au nanoparticles at 510°C. The AFM image in Fig 3.2A shows that no surface modification is observed when AsH_3 is present (sample A5); however, the annealing made in vacuum impacts the stability of the Au droplet, Fig. 3.2B, sample A3. In this case, the majority (~ 70%) of the droplets move, creating trails on the surface (Fig. 3.2B-D).

The depth profile across the trail shows a V-shape, with lateral planes forming ~ 45° with the substrate surface (Fig. 3.2B,C). The motion of the droplets occurs along the two equivalent directions ±[110], and the droplets move within distances in the range of 0.1 – 1.3 µm, as indicated by white arrows in Fig. 3.2D.

It is well known that liquid Au pieces or droplets on III-V surfaces strongly interact with the substrate when heated, dissolving material beneath the particles and forming a faceted pitch below the droplet [59, 108, 109]. Indeed, the volume of the 20 nm particles annealead at 510 °C observed after annealing is at least 30% greater than the nominal value for the colloidal particles used, indicating substrate material consumption. Fig. 3.2C shows that the trails are approximately 2 nm deep, and GaAs (100) native oxide layer is approximately 0.8 nm [110]. Thus, this result also suggests that the oxide layer was totally removed inside the trail due to the droplet crawling.
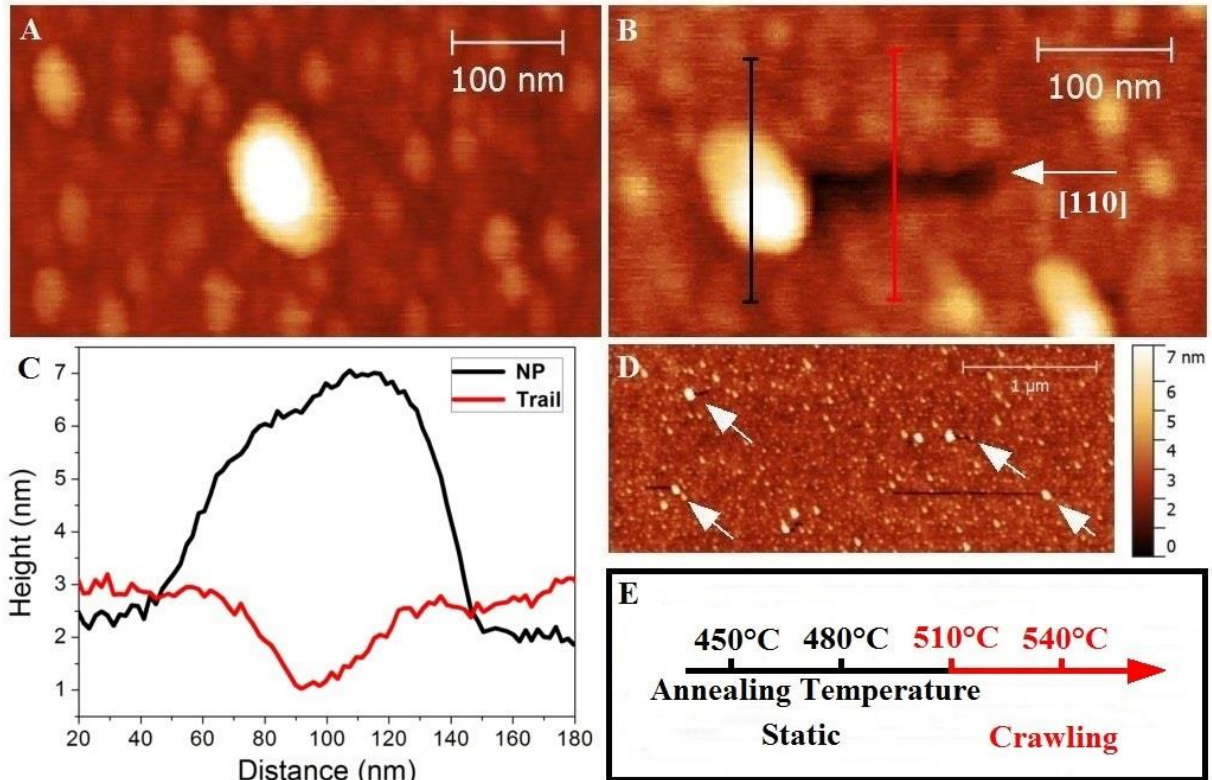
Figure 3.2 – (A) and (B) AFM topography images of the annealed sample using 20 nm Au nanoparticles deposited on (100) GaAs. Annealing was performed for 5 min at 510 °C under AsH$_3$ overpressure (13 sccm), and in vacuum (10^{-5} torr), samples A5 and A3, respectively. (C) Height profiles across the directions highlighted in black and red in (B), showing the faceted trail. (D) AFM topography image of the annealed sample in vacuum, shown in (B). (E) Representation of the effect of annealing temperature on the 20 nm Au nanoparticle stability for the annealing in vacuum; droplet crawling occurs at or above a critical temperature (510 °C), extracted from [65].

We summarize the temperature range for which motion occurs in Fig. 3.2E. Based on this data, we provide a picture of the process of thermally activated motion of the Au droplet on the III-V surface. The most likely scenario thus is that liquid Au droplets form V-shaped grooves composed by {111} planes on GaAs (100) surfaces, similarly to the behavior observed for interfacial reactions using Au thin films [109, 111]. These faceted grooves present two sets of Ga and As-terminated {111} planes, with projection on the (100) GaAs surface along the directions ±[110] and ±[1-10], respectively, as schematically represented in Figs. 3.3. These two different set of facets present distinct chemical etching rates, depending on the etchant used [112, 113]. The reaction of Au in Ga-terminated {111} facets is much faster than for As-terminated planes [110, 114]. Therefore, this inhomogeneous dissolution can explain the crawling along ± [110] directions, as illustrated in Fig. 3.3.

Concerning the driving force for the motion, we should mention that spontaneous temperature-activated motion of liquid metal droplets on III-V semiconductor surfaces has

already been reported, especially for Ga droplets [104, 106, 107]. In this case, droplet dynamics have been shown to be intrinsically associated with differences in surface roughness on solid surfaces, such as the local step density [106, 107]; in general, the motion can be interpreted as a result of the surface free energy gradient under nonequilibrium conditions, caused by changes in surface roughness [107]. Recently, the crawling of liquid droplets has been observed and studied in more detail for Au nanoparticles, where vacuum conditions [60] and the introduction of water vapor [59] during the heating step have been demonstrated to affect droplet stability. Despite chemical and surface energy differences for Ga and Au droplets on III-V surfaces, we can expect some common features.
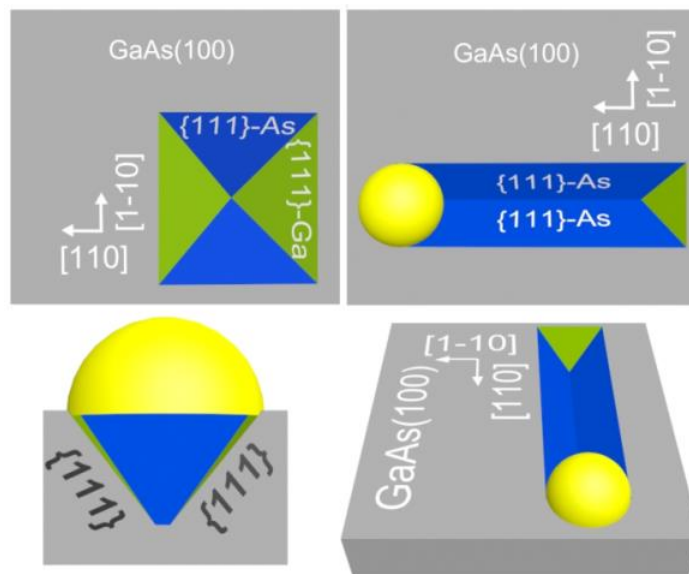
Figure 3.3 - Illustration of the crawling occurring in the specific ±[110] directions, due to the faster dissolution rate of Ga-terminated {111} facets by Au nanoparticles, extracted from [65].

Heating the substrate in vacuum can generate pits in the oxide layer of (100) GaAs surfaces at the temperature range used here (T > 500 °C) [115, 116, 117]. In fact, we observe an increase in surface roughness ($\sim 40\%$) when the annealing was performed in vacuum in comparison to As_2 overpressure. Therefore, the driving force for droplet motion, in our case, can be partially explained by the larger surface roughness, caused by our heating procedure. Thus, crawling of liquid Au droplets could minimize the total surface energy, eliminating steps and smoothening the surface, while consuming part of the underlying material [107]. However, we should point out that surface morphology has profound implications on the As and Ga evaporation rates, which may affect the droplet motion in a more complicated scenario [118], where the gradient of chemical composition around the droplet plays a significant role [104]. Therefore, we can summarize that the crawling of the Au droplets here is thermally activated

for small NP's (d < 20 nm), observed above an specific temperature (510 °C), with the annealing made in vacuum (base pressure 10^{-9} torr).

3.4 The influence of growth temperature and droplet size on GaP NW morphology

The effect of nanoparticle crawling on nanowire growth was investigated using the same temperature window where the spontaneous motion occurs. In this case, we have already described the growth [61]. The conditions used in previous work are described in table 3.2; GaAs(100) was used as substrate.

Sample	TEG (sccm)	PH₃ (sccm)	Time (min)	Temperature (°C)	Au NP (nm)
B1	2.4	15.0	60	450	5 and 20
B2	2.4	15.0	60	480	5 and 20
B3	2.4	15.0	60	510	5, 20 and 50
B4	2.4	15.0	60	540	5

Table 3.2 – Growth parameters for the growth of the asymmetric GaP nanowires at different temperatures.

Figures 3.4(a-c) show the resulting morphologies obtained with 5nm Au droplets. For the lower temperatures (450 and 480 °C), symmetric and conical nanowire shapes, due to reasonably low axial growth rates, are obtained. For temperatures from 510 up to 540 °C, an asymmetric morphology appears.
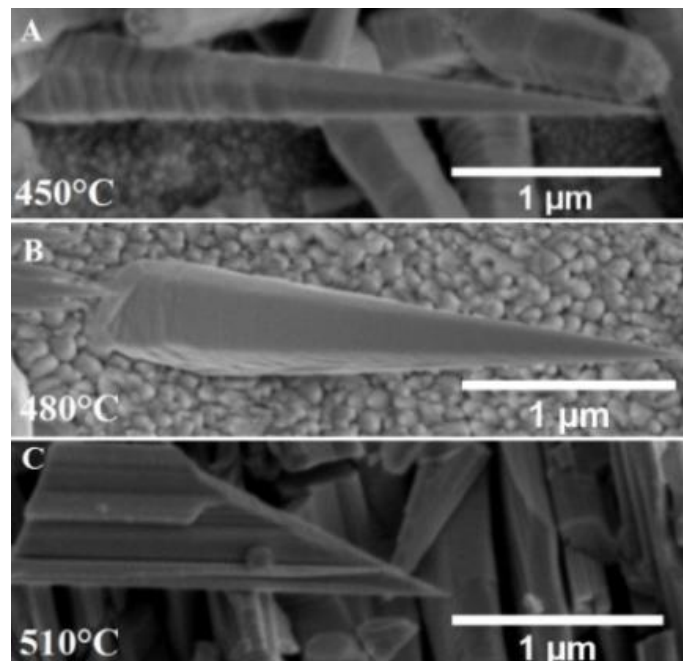
Figure 3.4 – SEM images showing the effect of growth temperature on the morphologies of GaP nanowires grown using Au 5 nm nanoparticles, extracted from [61, 65].

These structures show a base with a parallelogram shape and a conical top. Previously, we had observed that different structure populations had appeared on the sample; however, about 80% of them are asymmetric [61]. This asymmetric morphology is also observed as the main population (~ 60%; N = 200 nanowires) when we use 20 nm Au nanoparticles under the same GaP growth conditions [61]. We have prepared other samples in order to understand the growth window in which asymmetric GaP nanowires are formed. Fig. 3.5 shows results for the growth using larger (50 nm) Au catalysts; the droplet crawling also takes place on the substrate surface. However, during growth the metal catalyst keeps contact with the substrate, leading to the formation of irregularly-shaped planar nanowires [119]. Nevertheless, smaller Au dots, found along the planar structure, give rise to the growth of asymmetric structures as well.
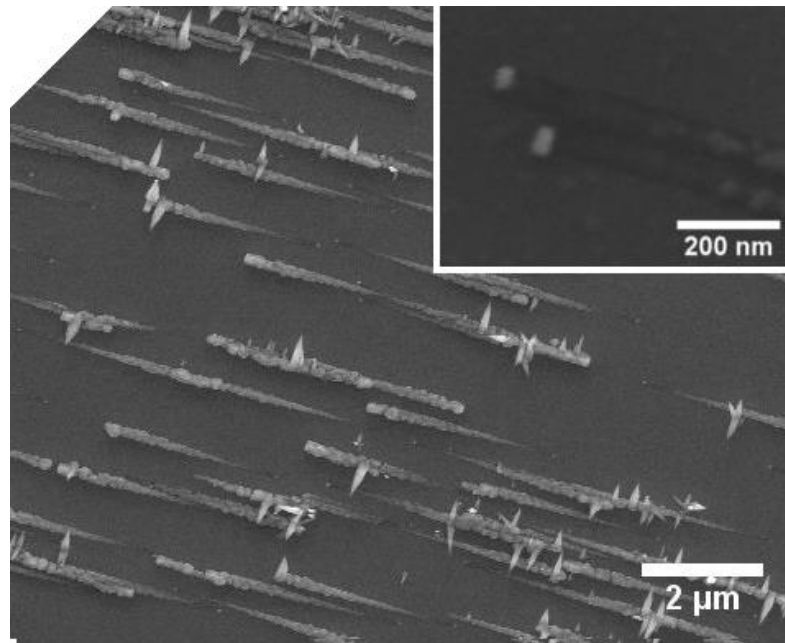
Figure 3.5 – SEM images of the growth using 50 nm Au nanoparticles. The particle left behind small Au dots, which allows the growth of the asymmetric structures along the trail of the particle, extracted from [65].

We had already observed that these alternative morphologies present the WZ phase, few stacking faults density (< 2/µm) and the usual [0001]B growth direction of hexagonal systems (5 nanowires were measured by HRTEM images throughout the entire NW) [61].

3.5 The effect of the TEG and PH$_3$ flows on asymmetric GaP NW growth

In order to better understand the growth dynamics of the asymmetric NWs, we have studied the general characteristics of the asymmetric structures under different V/III ratios. First, we have analyzed the effect of group III flow, i.e., the TEG precursor keeping PH$_3$ flow

constant, and also performed the growth at the highest and lowest V/III ratios in our CBE system, as shown in Table 3.3. In this case, annealing at 510 °C in vacuum was carried out before growth and the sample was cooled down under P_2 overpressure (15.0 sccm PH_3 flow).

Sample	TEG (sccm)	PH$_3$ (sccm)	Time (min)	Temperature (°C)	Au NP (nm)
C1	1.6	15.0	60	510	5
C2	2.4	15.0	60	510	5
C3	3.2	15.0	60	510	5
C4	4.0	15.0	60	510	5
C5	4.8	15.0	60	510	5
C6	1.0	37.5	60	510	5
C7	5.3	7.5	60	510	5

Table 3.3 – Growth parameters for the growth of asymmetric GaP nanowires using different group III flows.

Our results show that the general asymmetric morphology is preserved, but the nanostructure aspect ratio can be altered, Fig. 3.6.
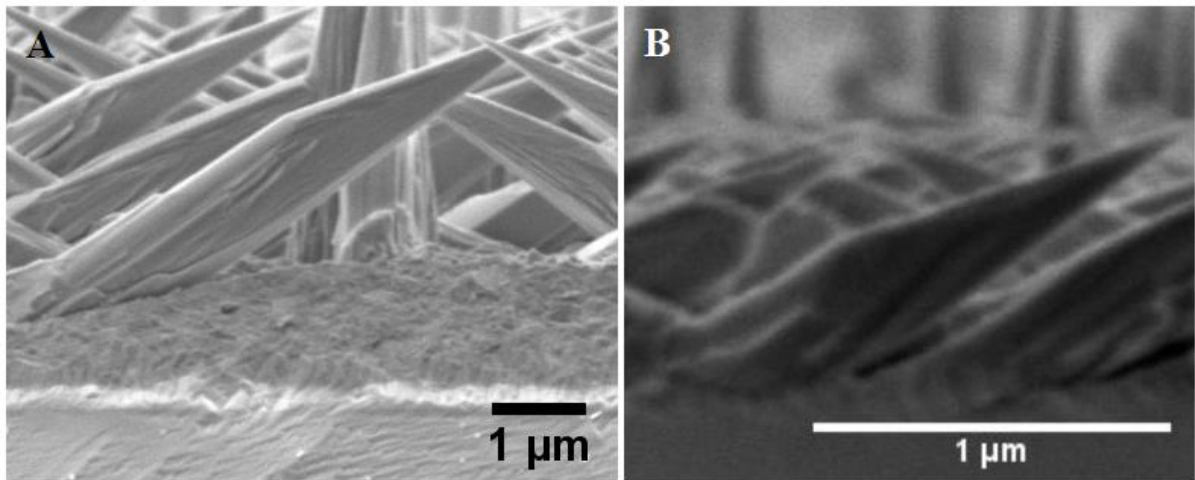
Figure 3.6 – (A and B) Side-view SEM images of the asymmetric GaP nanowires grown on GaAs (100) substrates at 510 °C using 5 nm Au NPs and different precursor flows, i.e., distinct V/III ratios: (A) high TEG flow at 5.3 sccm (with PH$_3$ at 7.5 sccm) and (B) low TEG at 1.0 sccm (with PH$_3$ at 37.5 sccm), extracted from [65].

The general nanostructure shape can be modified by TEG flow, and the parallel segment is enhanced for growth under high TEG flows (Fig. 3.6A). On the other hand, low values of group III precursor results in morphologies that resemble a nanosheet with high aspect ratio D/L (Fig. 3.6B). This dependence occur because the growth rate is directly dependent of the group III flow and, in our case, inside the temperature range in which TEG pyrolosis occurs and the desorption of alkyl species do not dominate, the group III flow/axial growth rate ratio

is constant. Thus, by controlling TEG flow, the ratio between axial VLS growth and radial VS growth can be modified and a finer morphology control within the temperature and nanoparticle sizes windows studied here is achieved, Fig. 3.7.
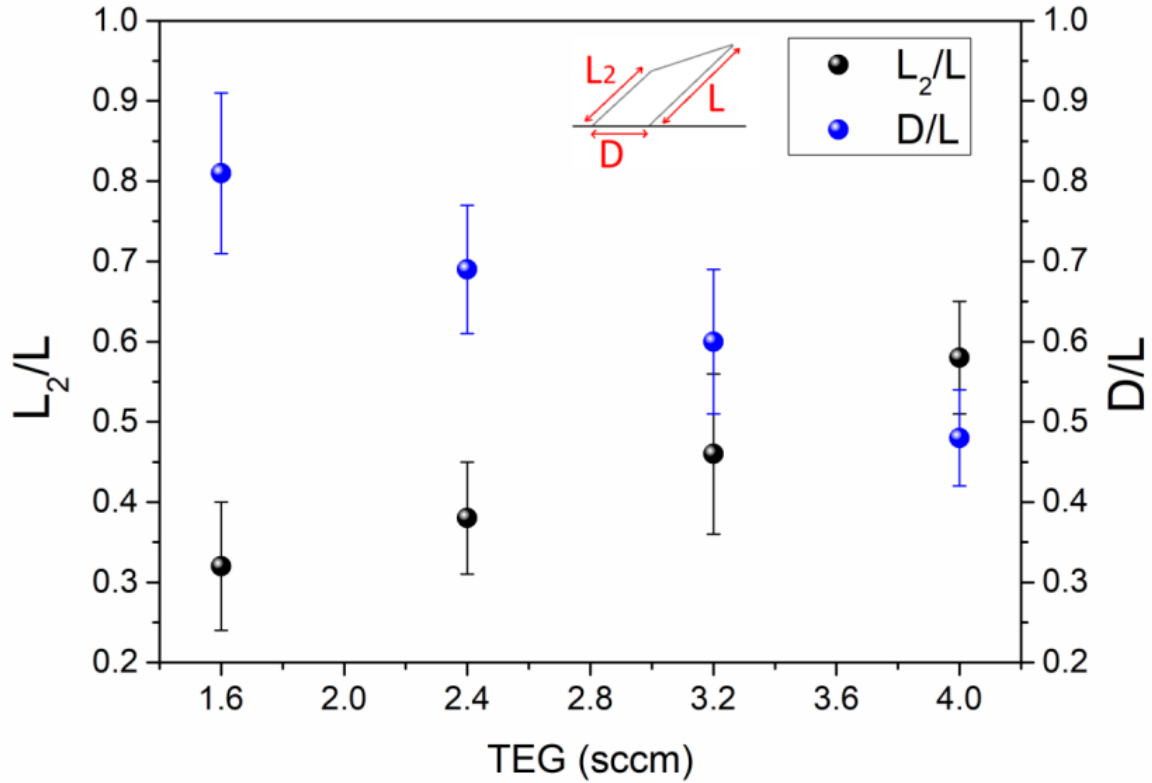
Figure 3.7 - Effect of the V/III ratio on the relative dimensions of the asymmetric GaP nanostructures: The impact of TEG with constant PH_3 flow at 15.0 sccm, extracted from [65].

On the other hand, the characteristic dimensions are not very sensitive to the group V precursor; keeping TEG flow constant and increasing PH_3 flow (Table 3.4), we can see no substantial change in the aspect ratio, Fig. 3.8.

Sample	TEG (sccm)	PH₃ (sccm)	Time (min)	Temperature (°C)	Au NP (nm)
D1	2.4	7.5	60	510	5
D2	2.4	15.0	60	510	5
D3	2.4	22.5	60	510	5
D4	2.4	30.0	60	510	5
D5	2.4	37.5	60	510	5

Table 3.4 – Growth parameters for the growth of the asymmetric GaP nanowires using different group V flows.
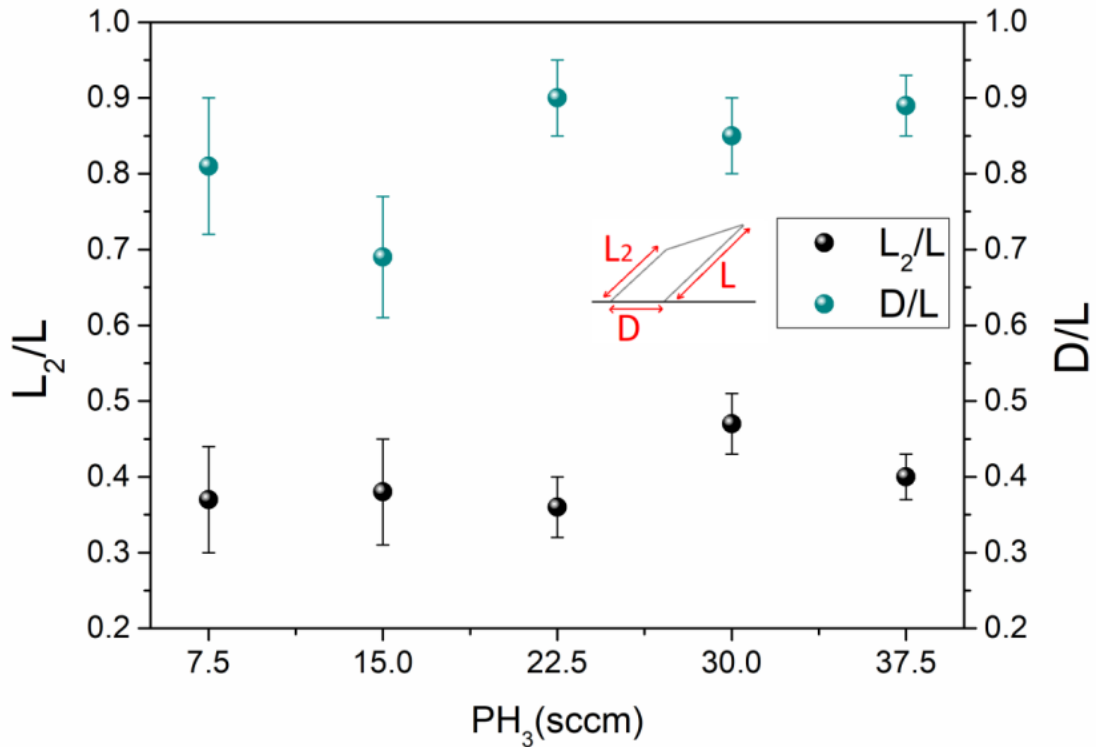
Figure 3.8 – Effect of the V/III ratio on the relative dimensions of the asymmetric GaP nanostructures: Effect of PH_3 with constant TEG flow at 2.4 sccm, extracted from [65].

3.6 The influence of surface energy and the balance between VS and VLS growth modes

The overall morphology of metal-catalyzed nanowires is determined by the balance of axial VLS and the VS growth on the exposed sidewalls. When nanowires expose facets with different polarities and hence distinct VS growth rates, the overall morphology can be quite distinct from the metal-catalyzed nanowire core [120, 121, 122, 123]. Wurtzite III-V nanowires grown in the <0001> direction usually exhibit low surface energy {10-10} or {11-20} planes as sidewalls, which results in a regular hexagonal cross-section [124, 125]. We have observed that the main facets correspond to {11-20} family planes [61]. Thus, since these non-polar planes should exhibit similar VS growth rates, they cannot account for the formation of this singular morphology.

The lack of high density of crystallographic defects and polar facets for the asymmetric nanowires suggests their association with the droplet crawling process, particularly because their formation occurs in the same temperature range. In fact, enhanced VS growth can be expected in the oxide-free region associated with the droplet trail, as similar temperature values are usually employed for thin film growth. The axial VLS growth rate decreases with increasing temperature [61] and more pronounced VS growth also occurs on the nanowire

sidewalls, which present areas much larger than the growth front of the catalyst droplet. Indeed, approximately 98% of the nanowire volume obtained can be attributed to VS growth.

It is interesting to note that the GaP axial growth rate is much smaller than for In-V nanowires grown in similar conditions, due to the low Ga solubility in the Au droplet [126]. We can thus expect similar magnitudes to both VS and VLS growth processes in Ga-base NWs. In fact, we have observed the formation of the same structure in the growth of GaAs nanowires in similar conditions, but we have not seen the same effect when we have employed the same procedure for the growth of InAs and InP nanowires, most likely due to the fast axial VLS growth rate, in this case.

We have also investigated the effect of energy surface, i.e., substrate nature and orientation in the formation of the asymmetric GaP NWs, Table 3.5.

Sample	TEG (sccm)	PH₃ (sccm)	Temperature (°C)	Au NP (nm)	Substrate
E1	2.4	15.0	510	5	GaAs(111)B
E2	2.4	15.0	510	5	InP(100)

Table 3.5 – Growth parameters for the growth of the asymmetric GaP nanowires on different substrates.

Figures 3.9A,B and 3.9C,D show GaP nanowires grown on (100) InP and (111)B GaAs substrates, respectively. We can observe in Fig. 3.9A-D that the asymmetric morphology is preserved in both cases, despite different geometrical characteristics. The axial growth rate is significantly altered when growth is carried out on (100) InP substrates, Figure 3.9A,B. Consequently, the aspect ratio of the asymmetric structures is also modified due to the different diffusion lengths on the substrate surface and material availability for the growth.
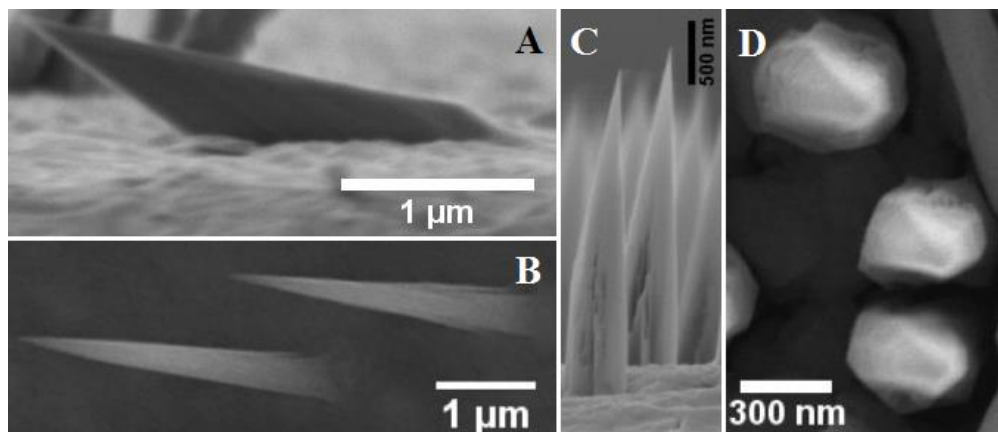
Figure 3.9 – SEM images of asymmetric GaP nanowires grown at 510 °C using 5 nm Au nanoparticles deposited on different substrates. (A and B) grown on (100) InP (C and D) grown on (111)B GaAs, extracted from [65].

Furthermore, vertical asymmetric nanowires with almost 100% yield are possible when the growth is carried out using (111)B GaAs substrates and 5 nm Au nanoparticles, Figure 3.9C,D. These observed changes are related to the interplay between nanoparticle crawling and surface chemistry, as well as group III solubility in the catalyst metal.

3.7 Initial stages of the growth of the asymmetric morphology

The effect of droplet crawling on nanowire growth and the driving mechanism for the asymmetric morphologies were studied by performing NW growth for short times. We have used the growth conditions described for sample B3 and grown GaP nanowires in different growth times. We present here the two more relevant cases for discussion.

In Fig. 3.10A we can see the AFM topographic image for the sample with growth carried out during 30 s on GaAs (100) substrates. It is possible to see that the droplet remains in contact with the substrate, and is connected to a short trail on the surface, along the same ±[110] directions observed for the crawling in the annealed sample. In the AFM height profiles we can see that more material is deposited along the trail as compared to surrounding areas (~ 2 nm in height differences), Fig. 3.10B.
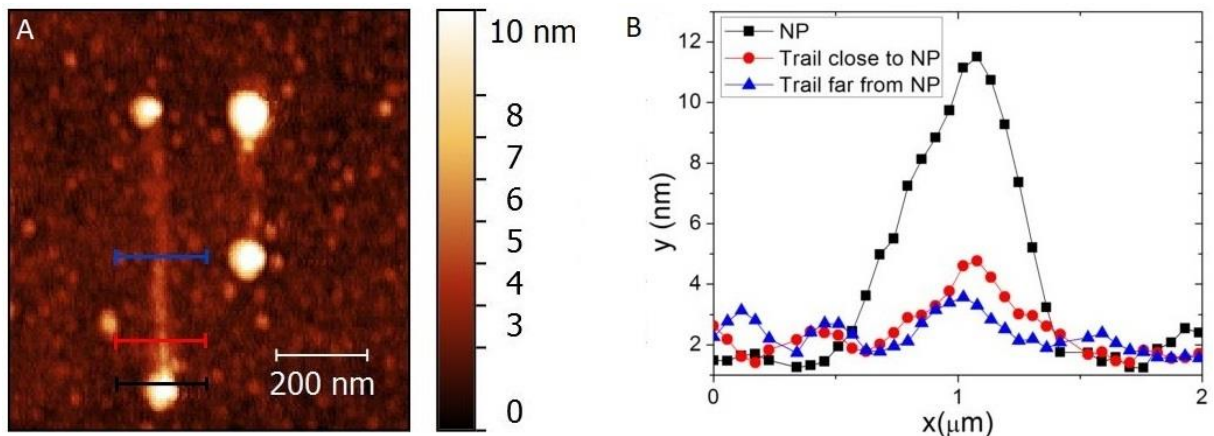
Figure 3.10 – Asymmetric GaP nanowires grown at 510 °C using 20 nm Au nanoparticles deposited on GaAs (100) substrates in the initial growth stages. (A) AFM topography image showing the growth performed for 30 s. (B) Height profiles showing that more material is deposited in the droplet trail, and closer to the nanoparticle, extracted from [65].

Statistical analysis of the lengths of the grown trails show that most of them (~ 70% ; N = 77 crawling nanoparticles) lie in the range 100 – 400 nm. These values agree well with the majority of the distances covered by the droplets during the annealing procedure, as described in section 3.3. We can also observe that there are droplets in the two opposite sides of the trail,

which is expected, since these two directions, ±[110], are crystallographic and chemically equivalent, i.e., they are the projection of Ga-terminated {111} facets on (100) substrate plane.

An axial lamella of the nanowires was prepared by FIB (Focused-Ion-Beam) in order to analyze the epitaxial relationship as well as the crystallographic information for short growth times. The lamella was prepared directly on the as-grown sample, in collaboration with Dr. Jefferson Bettini from the Brazilian Nanotecnology National Laboratory. Thus, for growth times around 300 s, we can see (Fig. 3.11) that the characteristic asymmetric shapes are already formed. At this stage, the structure exhibits a pedestal at its base. Side-view HRTEM images of the structure directly on the substrate are shown in Fig. 3.12A; the GaP pedestal grows in the zinc blend (ZB) phase and keeps an epitaxial relationship with the GaAs substrate, with no crystallographic defects at this point. The formation of a pedestal at the nanowire base is commonly attributed to the accumulation of material due to surface diffusion; once a pedestal is formed below the droplet, the crystallographic phase may change from ZB to WZ [127, 128, 129]. The formation of the cubic phase in the initial stages is generally associated to the low supersaturation condition of the droplet in the beginning of the growth [130].
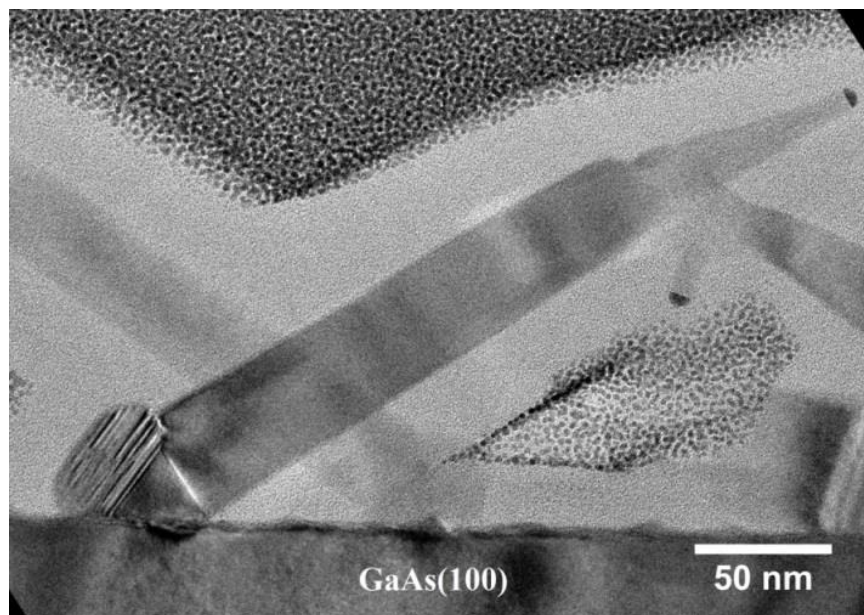
Figure 3.11 – Side-view low-magnification TEM images of the asymmetric GaP nanowire grown for 300s; the contrast variation at the nanowire pedestal is due to thickness differences during lamella preparation, extracted from [65].

Fig. 3.12B shows a sharp and defect-free interface between the two phases at the beginning of the growth, and the wurtzite phase of the asymmetric nanowires appears after the

droplet loses contact with the substrate, Fig. 3.12A. Furthermore, stacking faults and diameter variations appear in the top region of the structure; however, they are not necessarily related. These observations suggest that the pedestal could act as a buffer layer, also releasing the elastic energy accumulated due to the lattice mismatch between GaP and the GaAs substrate [131].
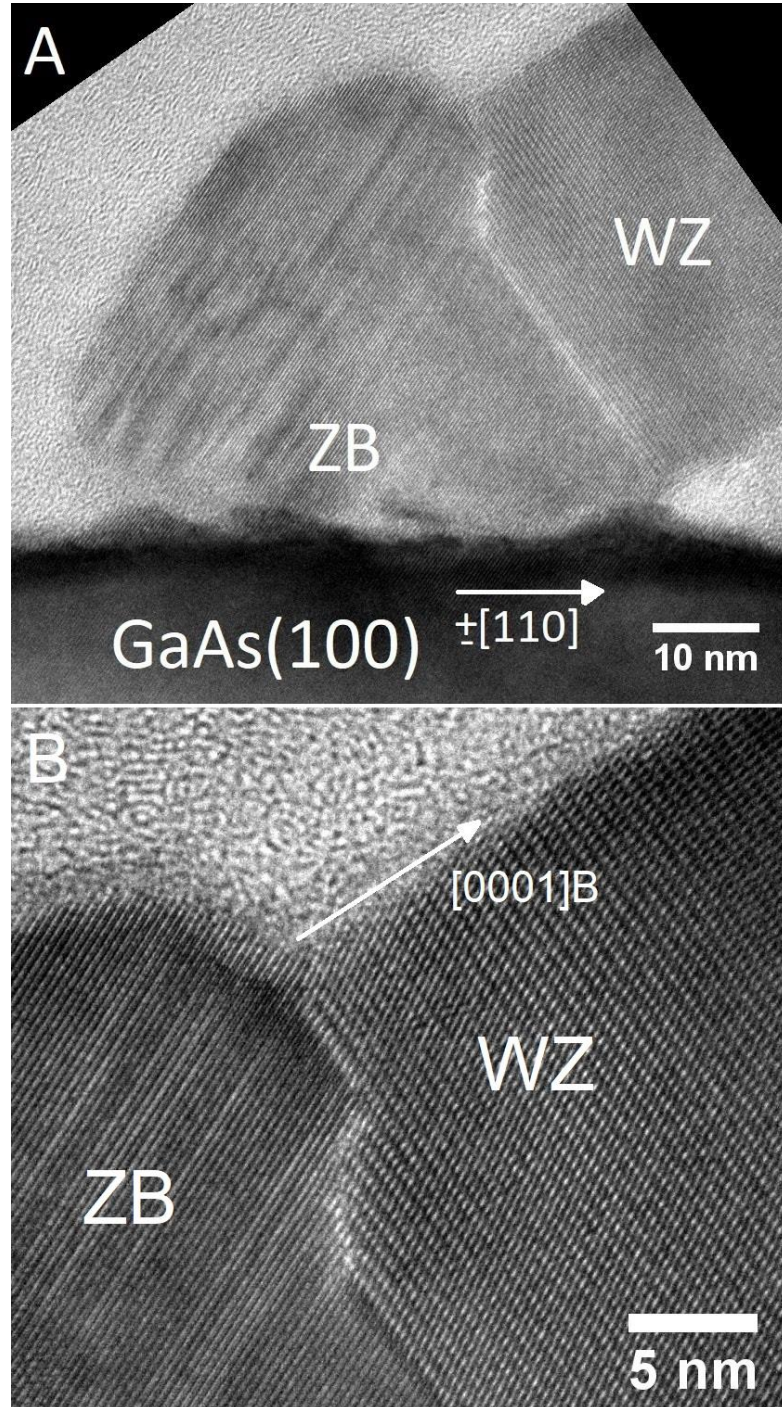
Figure 3.12 – (A and B) Side-view HRTEM images of the asymmetric GaP nanowire grown for 300 s. It is possible to see that a ZB pedestal forms during growth and the WZ phase occurs when the NP loses contact with the substrate. An asymmetric deposition of material is also observed in (A), extracted from [65].

3.8 Proposed growth scenario for the asymmetric WZ GaP NWs

The droplet behavior observed in the initial growth stages may have important implications to the entire nanowire growth process. Based on data presented up to this point, our interpretation for the growth scenario that leads to the asymmetric morphology follows below.

First, during the heating of the substrate in vacuum the droplet moves due to temperature-activated surface processes, Fig. 3.13a, b.
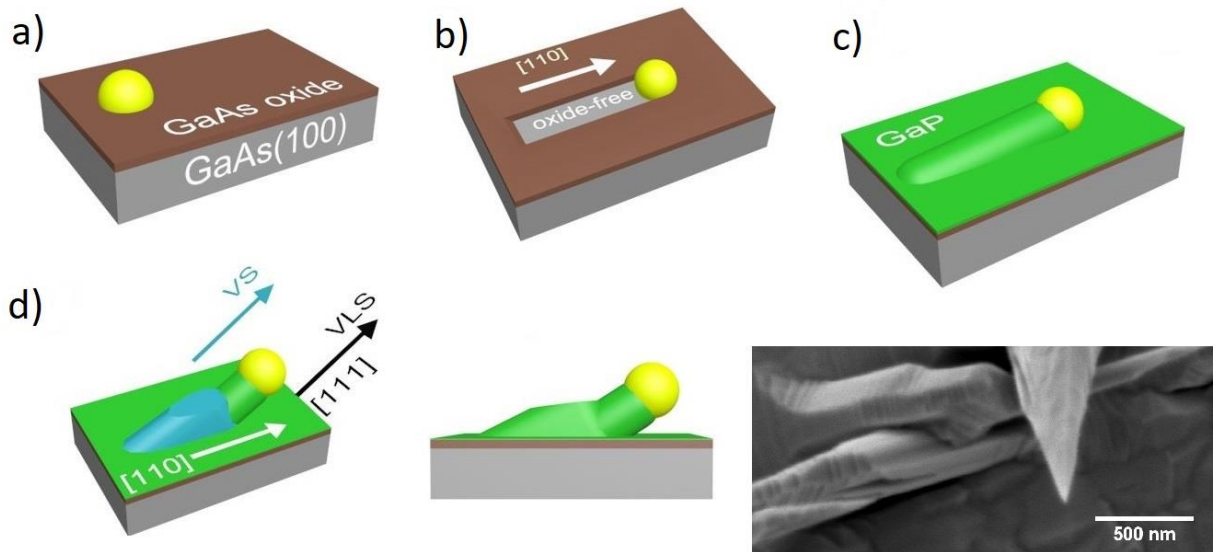
Figure 3.13 – (a) Illustration of the growth scenario which leads to the asymmetric morphology. Inset: SEM image of GaP nanowires grown at 510 °C; the asymmetric morphology shows different aspect ratio due to shadow effects caused by another nanowire, extracted from [65].

However, in the temperature range used, the oxide layer on the remaining substrate surface is not entirely removed [115]. The droplet crawling alters the roughness of the original surface, consuming the oxide layer and part of the underlying substrate surface. This crawling process thus generates areas where the bare semiconductor surface is totally exposed (Fig. 3.13b), hence effectively creating a selective area VS growth [132, 133]. Due to the asymmetry created by droplet along the trail, preferential deposition occurs at the side of the droplet-trail interface, with large VS growth rates due to the high temperature employed, Fig. 3.13c (510 °C).

Subsequently, after the final supersaturation condition is achieved and the formation of the first VLS layers occurs, the droplet loses contact with the substrate, originating the wurtzite phase. From this point on, the nanowire is supported by a thicker ZB GaP originated from the enhanced deposition on the trail of the droplet (Fig. 3.13c, d). It is interesting to note

that the sidewalls opposite to the droplet trail are not supported by a ZB base, and instead present a clear interface with the GaAs surface (Fig. 3.12A). In this scenario we may assume that a stress field arises due to the lattice mismatch, creating a gradient in the chemical potential which modifies adatom kinetics [134, 135], favoring incorporation on the thicker GaP regions. As both VLS and VS growth processes take place (Fig. 3.13d), the asymmetric morphology appears. Diffusive processes create mass transport along the different sidewalls of the growing structure, eventually leading to the formation of intermediary facets with lower surface energy. The presence of new facets other than {11-20} could also influence the VS growth rate for the non-polar planes [61]. However, if a nanowire shadows the stub originated by VS growth, the structure does not form, inset in Fig. 3.13.

Therefore, in our interpretation, the crawling and the subsequent pedestal formation alter the adatom kinetics creating an unbalanced VS growth on the apolar sidewalls. This process also generates enhanced VS growth originated from the trail, eventually leading to the asymmetric morphology. A similar process has been reported for V-shaped InAs nanomembranes [33], originated from growth at the opposite facets of a rectangular pyramidal island nucleus, obtained via selective area epitaxy using nanoscale apertures on a dielectric mask. In our case, the preferential Au dissolution on Ga-terminated {111} facets, and the resulting droplet trail, determine the asymmetry of our nanostructures. Furthermore, the procedure demonstrated here does not require lithographic processes before growth, while providing a high yield of the asymmetric nanostructures, by exploring a much simpler process.

Nevertheless, despite the important role of the droplet trail for the asymmetric growth scenario, its length does not directly determine the final nanowire width, as we can see in Fig. 3.14. Although the crawling occurs in a large range of distances (0.1 – 1.3 µm), the width of the asymmetric morphology is restricted to a few hundreds nm. The VS growth on the trail is not uniform, and more material is deposited close to the droplet. The most likely reason is that VLS growth continues during the deposition on oxide-free areas, and both the nanowire pedestal and sidewalls can act as nucleation regions for VS growth. Therefore, substrate annealing conditions and the resulting broad range of droplet trail lengths are not necessarily the best parameters for growth control. The final nanostructure morphology can be more effectively altered via V/III flux ratios and TEG flow in particular, as we have discussed in section 3.5. In addition, we should point out that the crawling process could be explored for creating *in situ* preferential deposition areas, and subsequent growth performed at higher

temperatures could be employed in order to minimize nanowire growth, providing morphologies such as rectangular nanosheets, for example.
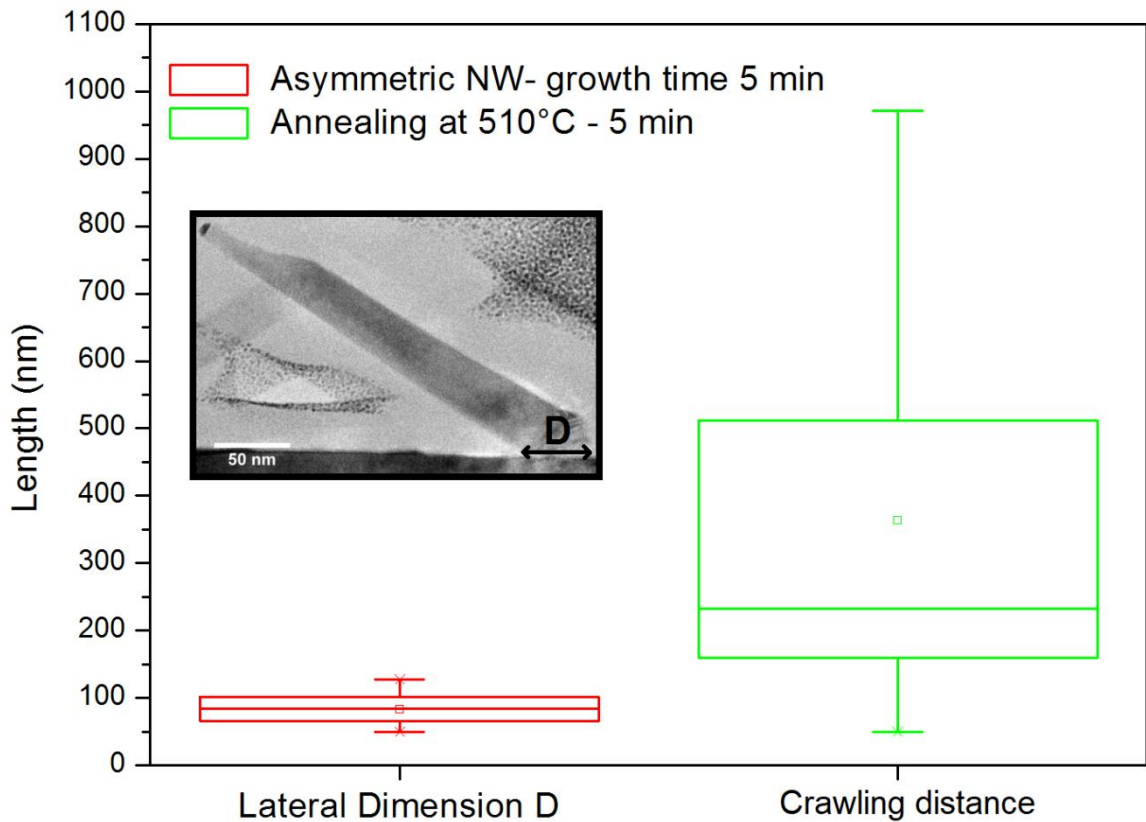
Figure 3.14 – Box plot comparing the crawling distance and the lateral dimension for the growth performed for 5 min. Inset: TEM image of the asymmetric GaP NW grown for 5 min (N = 77), extracted from [65].

3.9 Conclusions

In this work, we have reported that the crawling of Au droplets can be used to alter the nanowire growth process in order to escape from traditional nanowire morphologies. We have investigated the driving force behind the spontaneous motion of the Au droplets, demonstrating that the motion is intrinsically linked to surface quality, as surface roughness, and the droplets move along specific crystal directions caused by unbalanced etching on {111} facets. We have also shown that crawling can be activated, for small particles, by a simple annealing procedure performed at a critical temperature, in a range where the oxide layer has probably not yet been totally removed. Concerning the nanowire growth dynamics, our result indicates that the crawling can locally remove the oxide layer. These oxide-free areas, due to the high temperature employed, present an enhanced vapor-solid growth compared to non-modified areas. We have proposed that this effect may alter the growth kinetics in the initial

stages of the growth and, combined with the slow axial growth rate of Ga-based nanowires, leads to formation of these distinct morphologies. Additionally, the asymmetric morphology can also be obtained in different substrates and overall morphology can be controlled by TEG flow, rather than PH_3 precursor.

In conclusion, the development of new bottom-up procedures to obtain fine control over the morphology, as demonstrated here, could be explored for photonic applications as, for example, antireflection coatings [33]. Moreover, the large area and volume of GaP in the WZ phase with good crystal quality make them interesting building blocks for optoeletronic applications as well as virtual substrates with large 2D areas for the growth of Si and SiGe alloys in the hexagonal phase, since the lattice mismatch between GaP and Si is small (less than 0.5%) [136].

Chapter 4

Optical properties of WZ GaP NWs: probing the electronic band structure and understanding impurity-related luminescence

4.1 Introduction

The Wurtzite (WZ) phase of Gallium Phosphide has been studied in the last few years due to the novel properties obtained by controlling the crystal structure. It has been predicted as a direct (or pseudo-direct) band gap semiconductor, with emission in the amber/green spectral range [40, 41, 55, 137, 53].

Despite the effort of many research groups in recent years, measurements of the predicted direct band gap of WZ GaP have remained elusive [55, 57, 56, 58]. Density Functional Theory (DFT) calculations have led to the speculation that the electronic band structure exhibits anomalous behavior, i.e., an almost forbidden fundamental optical transition, which is called a pseudo-direct gap [55, 54], as discussed in chapter 2. Very few works have investigated in detail Wurtzite GaP optical properties [41, 55, 57], and no conclusive experimental evidence about the exact value of the band gap as well as the possible pseudo-direct behavior of this material has been provided so far.

Furthermore, in vapor-phase growth systems when a organometallic source is used, carbon is expected as the main contaminant, which comes from the pyrolysis of the organometallic precursor [138, 139]. However, other different residual impurities may also be incorporated, usually associated with impurity levels in the organometallic source. For example, Cd, Zn, S, Sn, Al, Cu and mainly Si have been reported as unintentional impurities in undoped GaAs [140, 141, 142]. Therefore, understanding the correlation between optical properties and growth conditions is crucial to achieve very high quality crystals and, consequently, optimize optoelectronic device fabrication. However, no report in literature so far has discussed the impact of growth conditions on the luminescence neither on the nature of typical residual impurity emissions observed in the hexagonal phase of GaP nanowires – even if in most cases they dominate the photoluminescence spectra [56, 58, 65].

In this chapter we report our investigation on the optical properties of WZ GaP nanowires, presenting the optical data and then discussing the results. First, we have probed the

electronic band structure of WZ GaP using Photoluminescence Excitation (PLE) spectroscopy. In order to enhance the PL signal detected in PLE, large volume, asymmetric WZ GaP structures were successfully grown, allowing us to measure the lowest energy band-to-band absorption edges of this material. We have also studied the influence of growth parameters of Au-seeded WZ GaP NWs on photoluminescence properties and on the incorporation of residual impurities and defects. Using different growth conditions for doped and undoped nanowires, changing the III/V flux ratio, and varying optical measurement conditions (sample temperature and excitation power), we have identified deep and shallow level optical emission bands.

4.2 Growth of very large WZ GaP structures

The photoluminescence (PL) signal at low temperature (10 K) of the WZ GaP nanowires discussed in chapter 3 is weak, as we will discuss in more detail further in the chapter. Preliminary photoluminescence excitation spectroscopy (PLE) measurements were not able to resolve the first absorption edges of the WZ GaP; therefore we did not observe an excitonic recombination for the PL or μ-PL measurements. In fact, GaP is very sensitive to surface states, and it is important to passivate the surface to improve the optical signal. Growing a lattice-matched material with larger band gap than GaP, such as AlGaP [41, 58], can do that; however, we do not have an Al source in our CBE system.

In order to overcome this barrier and to study the optical absorption as well as the excitonic recombination of the WZ GaP nanowires, we have grown a very large structure, with micron-sized diameter, for 6 hours using the conditions described for sample B3 in chapter 3. With this sample, we were able to improve the signal/noise ratio and measure the first electronic transitions as well as the excitonic recombinations. We can see in Fig. 4.1a,b and 4.2 that the same morphology is obtained for the growth performed for 1 h (Fig. 4.1a) and 6 h (Fig. 4.1b).
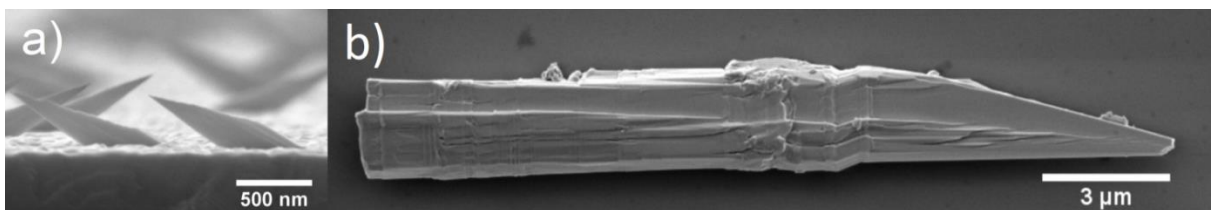
Figure 4.1 – (a) Side-view SEM image of as-grown asymmetric WZ GaP nanowire grown for 1 h. (b) Top-view SEM image of GaP structure grown for 6 hours and transferred to Si substrate.

On average, the as-grown structures have a length of approximately 40 µm and more than 2.5 µm in diameter, Fig. 4.1b and Fig. 4.2. The growth procedure studied in chapter

3 allowed us to obtain large volume of WZ GaP, since the majority of the structure is formed by the Vapor-Solid (VS) mechanism. The WZ phase is obtained in nanowires due to the high surface/volume ratio, and the WZ phase is expected for small structures only. However, it has been observed that the experimental size limits of Au-catalyzed VLS grown nanowires for the formation of WZ phase is much higher than the theoretical values reported [143, 36]. Therefore, we should inspect if our microsized GaP structure is indeed in the hexagonal phase, as recently reported for InP [37].
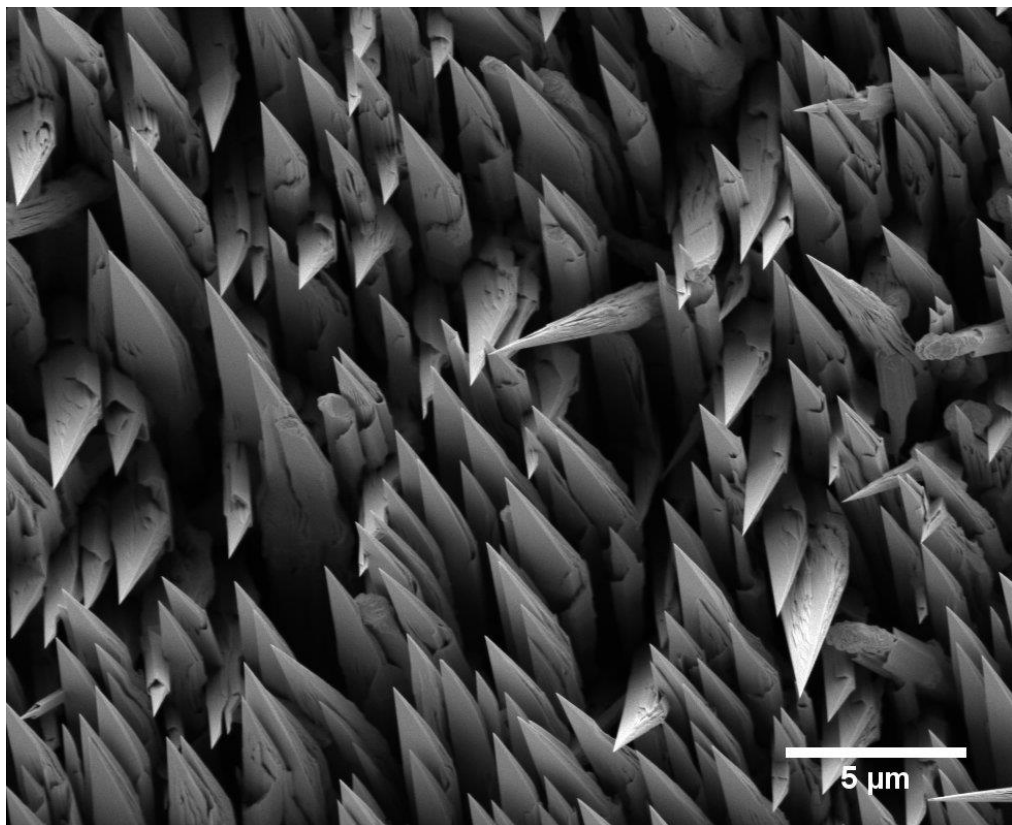
Figure 4.2 Top-view SEM images of sample with large asymmetric WZ GaP structure grown for 6 hours; the structures present average length of 40 µm and diameter up to 3 µm.

First, we have analyzed the GaP structures by Raman spectroscopy; we have observed the characteristic signal from the WZ phase, as we will discuss in more detail in section 4.3. Next, in order to understand the inhomogeneities, and inspect crystal structure at the atomic level, i.e., the formation of defects such as stacking faults or ZB insertions along the nanowire, we have prepared a lamella by Focused Ion Beam (FIB), in collaboration with Dr. Braulio Archanjo from the National Institute of Metrology, Quality and Technology (Inmetro) in Rio de Janeiro, Brazil.

Figure 4.3a,b shows the TEM images of the lamela and the SAED pattern, acquired at the base of the GaP structure (the SAED pattern measured in the tip was similar). The contrast differences in Fig. 4.3a are related to thickness variation during lamela preparation. The SAED patterns are indexed as WZ in the [10-10] zone axis.
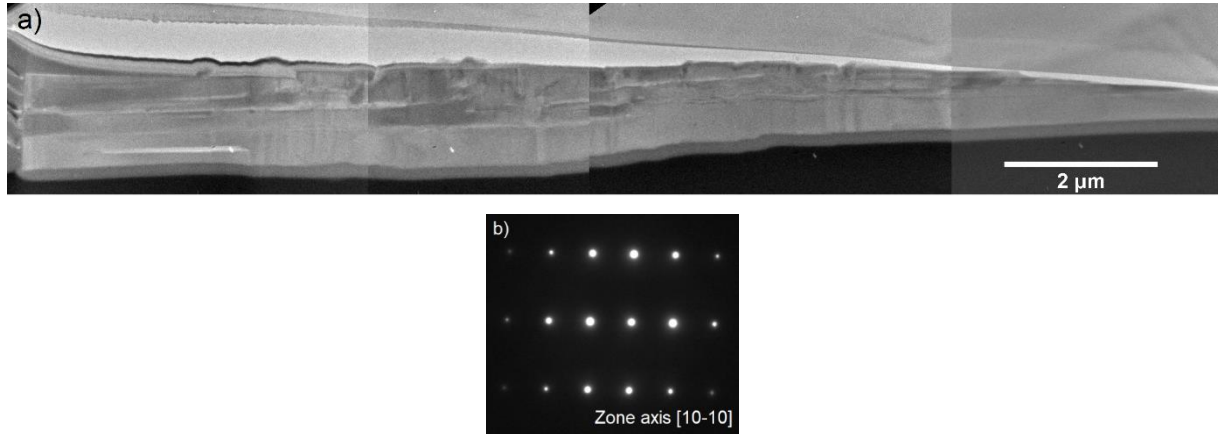
Figure 4.3 (a) Mosaic of low magnification TEM image of a lamella prepared from the WZ GaP structure (b) SAED pattern acquired at the basis and of the structure and indexed as WZ in the [10-10] zone axis, the same SAED pattern was observed at the tip of the structure.

We have analyzed by HRTEM different areas of the structure as shown in Fig. 4.4, where the image was obtained in the middle segment along the axis of the structure. Different areas across the microsized structure were analyzed, and very few defects were observed. Therefore, both SAED patterns and HRTEM images indicate that the structure has a good crystal quality and the WZ phase is preserved despite the large volume.
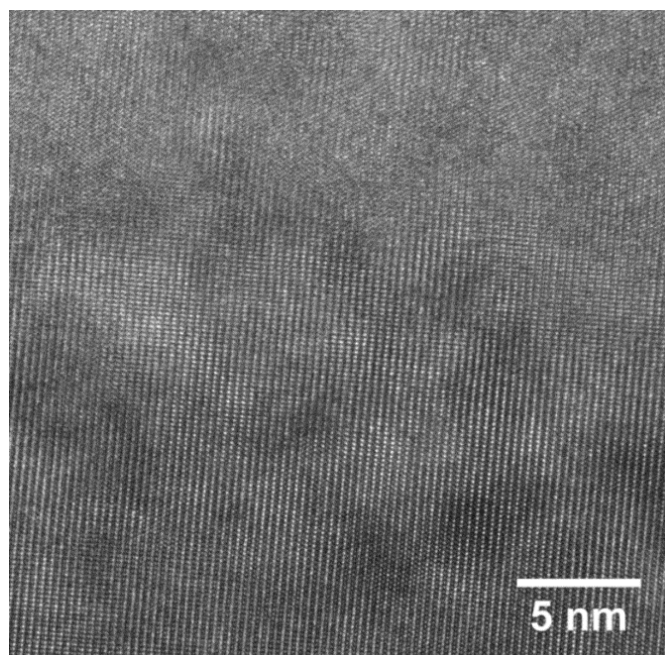
Figure 4.4 HRTEM image of the lamella prepared by FIB of the asymmetric GaP grown for 6 h.

4.3 Raman Spectroscopy: probing crystal structure and identifying the vibrational modes of the WZ GaP phase

In order to probe the crystal structure, room temperature μ-Raman spectroscopy was used with two line polarization configurations: $Z(XY)\bar{Z}$ and $Z(XX)\bar{Z}$. Here X and Y are the light polarization direction of the excitation and detection. In our experiment X lays along the basal plane and Y along the c-axis of the WZ crystal, Fig. 4.5. The directions Z and $\bar{Z}$ are the incident and scattered light directions, respectively, along the perpendicular direction of X and Y axes, Fig. 4.5.
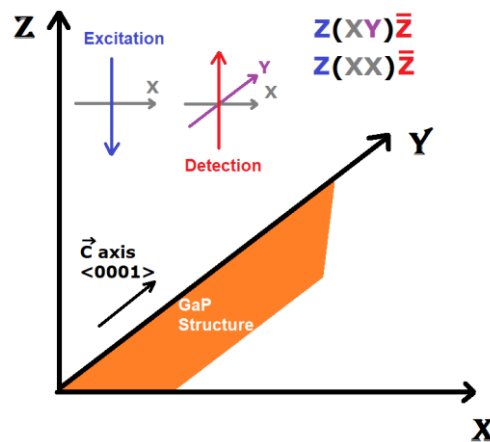
Figure 4.5 Schematic representation of the different configurations used in the Raman measurements.

The Raman spectrum depicted in Fig. 4.6 shows the characteristic Raman active vibrational mode E_2^L of the WZ GaP at 78.1 cm⁻¹ [144]. Other Raman allowed mode in $Z(XX)\bar{Z}$ configuration is E_2^H at 355.8 cm⁻¹. The A₁(TO) at 363.4 cm⁻¹ is also observed (see Fig. 4.6). The $Z(XY)\bar{Z}$ configuration, Fig. 4.7, provides only E₁(TO) mode at 363.4 cm⁻¹ (see Fig. 4.7). The E_2^H peak in this case is observed due to the relaxation of selection rules; the forbidden modes assigned as E₁(LO) at 401.4 cm⁻¹ and A₁(LO) at 395.7 cm⁻¹ are also observed.

The pronounced forbidden LO modes presented in Fig. 4.6 and 4.7 are most likely caused by resonance effects. The 488 nm (2.54 eV) laser line is very close to the high energy band transition as will be demonstrated below in our PLE spectra. Recently, Panda et al. have shown the use of this resonance effect to investigate electronic transitions in WZ GaP [144]. It is important to note that the lateral dimensions (d) of the WZ GaP structure discussed here are much larger than for usual nanowires and, since d >> λ (λ is the wavelength of the laser spot), thus we rule out antenna effects [145]. Similar enhancement has also been observed in other polar semiconductors such as in GaAs [146], InAs [95], and CdS [147]. In most cases, this

resonance effects lead the forbidden LO modes to reach the same order of magnitude than the allowed modes at resonance [144, 146, 95, 147]. The LO phonons involve uniform displacements of charged atoms, which are accompanied by a macroscopic electric field; consequently, electrons are expected to couple to these LO phonons in polar semiconductors, a phenomena described by the Fröhlich interactions [3]. The breakdown of Raman selection rules near resonance has been observed for nanostructures as well as for bulk materials [144, 146, 95, 147, 148]. Therefore, we speculate that, for our GaP structure , the mechanism behind the LO enhancement could be related to bulk effects depending on the excited electronic state, as proposed for CdS [147].
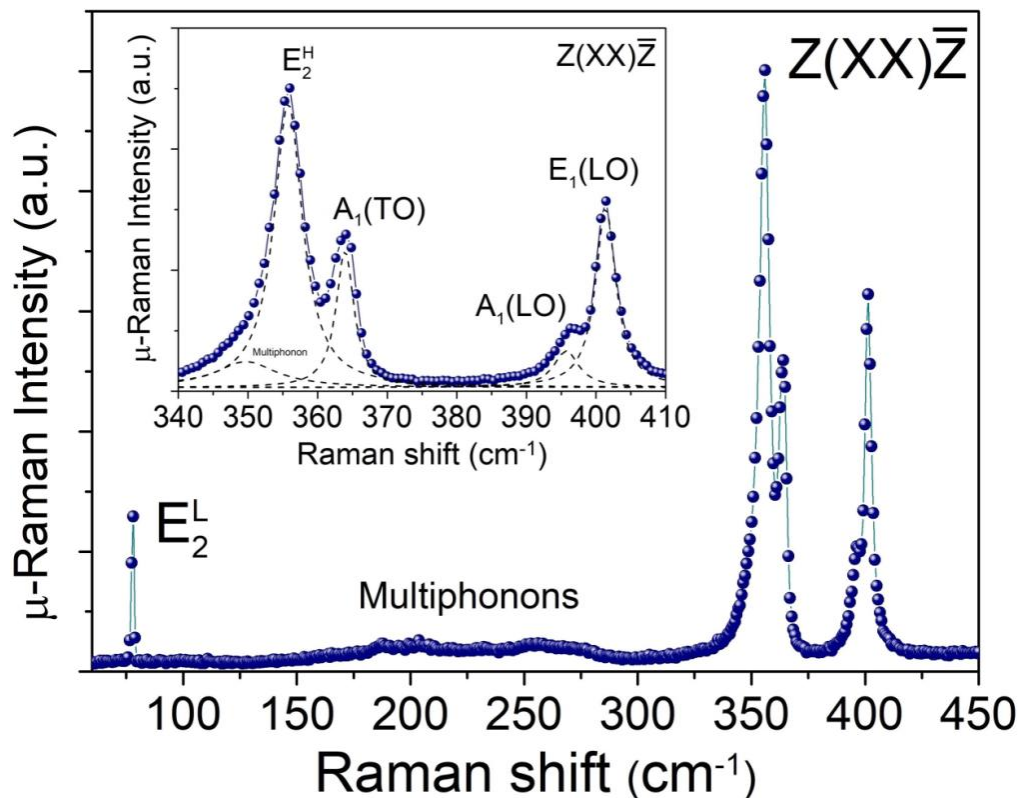
Figure 4.6 Room temperature Raman spectra performed in the $Z(XX)\overline{Z}$ configuration. Insets show the deconvoluted modes around the optical phonons in dashed lines.

Multiphonon scattering is also observed between 150 - 300 cm^{-1} in the Raman spectra presented in Fig. 4.6 and 4.7. Moreover, the peak at 78.1 cm^{-1}, i.e., E_2^L mode is absent in ZB phase, thus confirming the presence of the WZ phase in our very large GaP structures [97, 144]. All the vibrational modes measured are summarized, assigned and compared with the predicted values in Table 4.1.

Raman mode	Configuration	Measured position (cm⁻¹)	Predicted position (cm⁻¹)
E_2^L	$Z(XX)\bar{Z},\ Z(YY)\bar{Z},\ X(YY)\bar{X},\ X(YY)\bar{Z}$	78.1	78
E_2^H	$Z(XX)\bar{Z},\ Z(YY)\bar{Z},\ X(YY)\bar{X},\ X(YY)\bar{Z}$	355.8	368
A$_1$(LO)	$Z(YY)\bar{Z}$	363.4	407
E$_1$(LO)	$X(YZ)\bar{Y}$	395.7	402
A$_1$(TO)	$X(YY)\bar{X}, X(ZZ)\bar{X}$	401.4	362
E$_1$(TO)	$Z(XY)\bar{Z}$	363.4	362

Table 4.1 – Vibrational modes measured by Raman spectroscopy at room temperature in this work and predicted theoretical values [149].
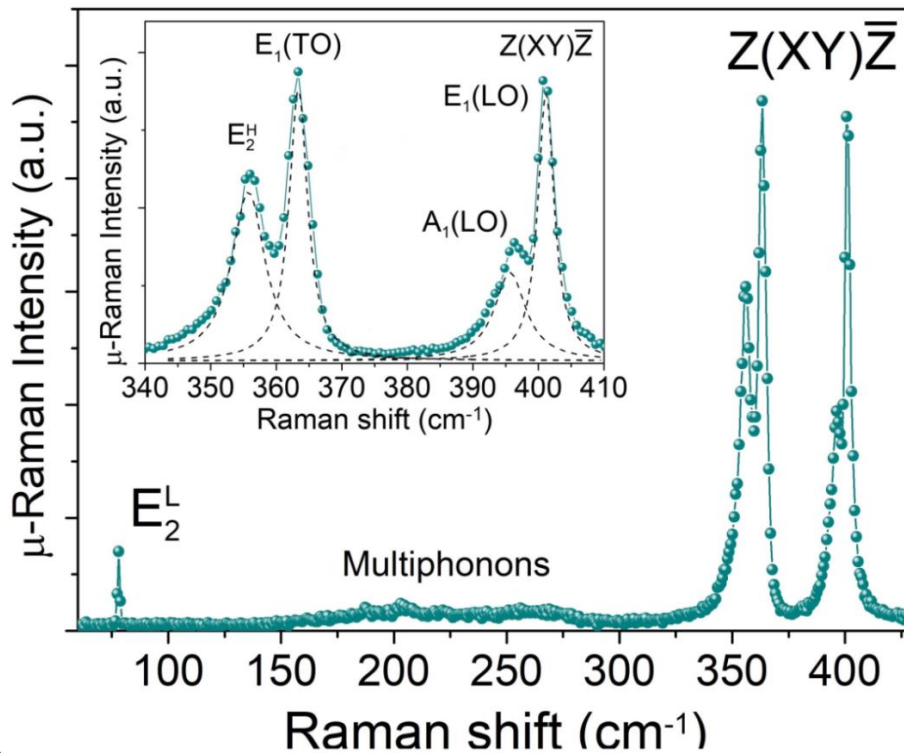
Figure 4.7 Room temperature Raman spectra performed in the $Z(XY)\bar{Z}$ configuration. Insets show the deconvoluted modes around the optical phonons in dashed lines.

We have also performed Raman measurements across the GaP structure axis, Fig. 4.8. It is possible to see the characteristic mode E_2^L mode at 78.1 cm⁻¹ in the entire structure, showing the WZ phase is present. Moreover, a slight shift in the TO modes accompanied by an inversion of the TO modes intensity was observed. This inversion is confined to specific regions across the axis and always observed at the base of the structure, which suggests that it is related

to extended crystal defects. The lamella prepared by FIB has approximately 20 µm in length. Thus, it is possible that at the very bottom of the structure defects appear, since we should not expect a stable WZ phase in this case. More careful studies should be done in order to fully understand this result.

Therefore, as the TEM analysis, the µ-Raman scattering results show clear evidence of the WZ phase in the GaP structure, since zinc-blend (ZB) GaP presents only two optical modes. In addition, we provide experimental information about the exact position of the vibrational modes of the WZ GaP, which can be used in the future to probe this crystal structure.
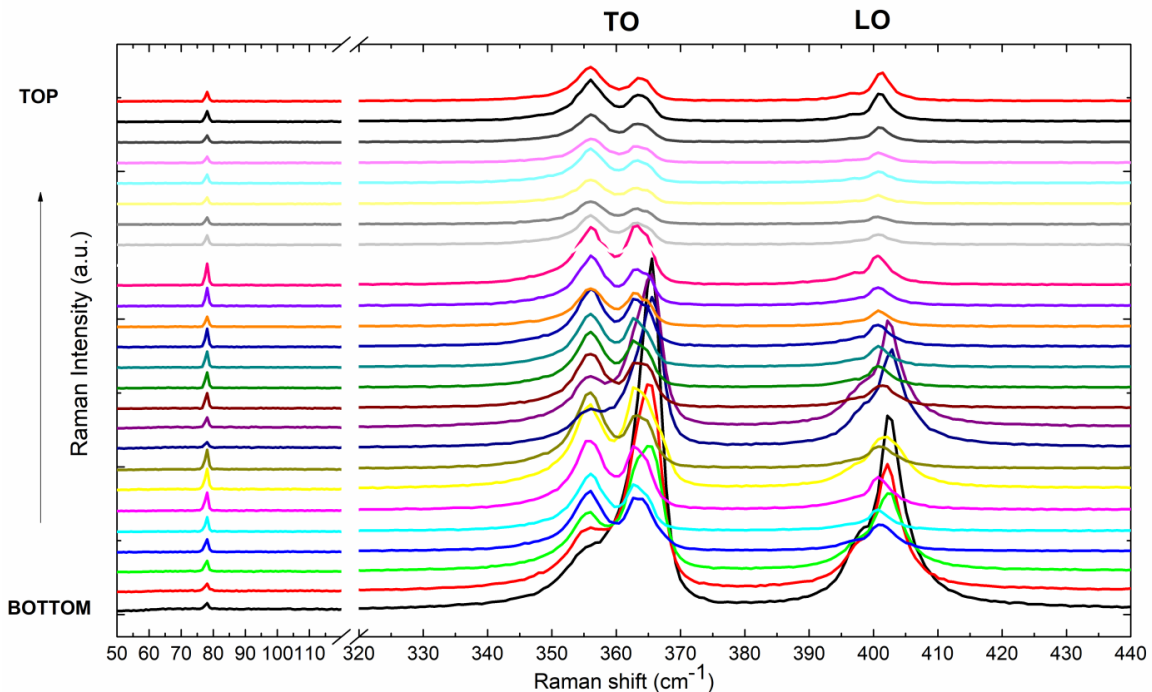
Figure 4.8 Room temperature Raman spectra performed in the $Z(XX)\overline{Z}$ configuration across the axis of the large GaP structures. It is possible to see the E_2^L mode at 78.1 cm^{-1} in the entire structure. The spatial step between sucessive spectra is 1 µm.

4.4 Low temperature PL of asymmetric WZ GaP NWs

Figure 4.9a shows the typical low temperature (10 K) macro-PL spectrum of the as-grown sample with WZ asymmetric GaP structures, which was performed at low excitation intensity regime (intensity < 0.1 kW/cm^2). We can see in Fig. 4.9a that the overall spectrum is dominated by broad emissions below 2.0 eV and two relatively narrow (FWHM ~ 30 meV) peaks at 2.04 eV and 2.09 eV are also observed. Throughout this work we will refer to these main emissions as band 1 (~ 1.68 eV), band 2 (~1.88 eV), peak A (2.04 eV) and peak B (2.09 eV), Fig. 4.9a.
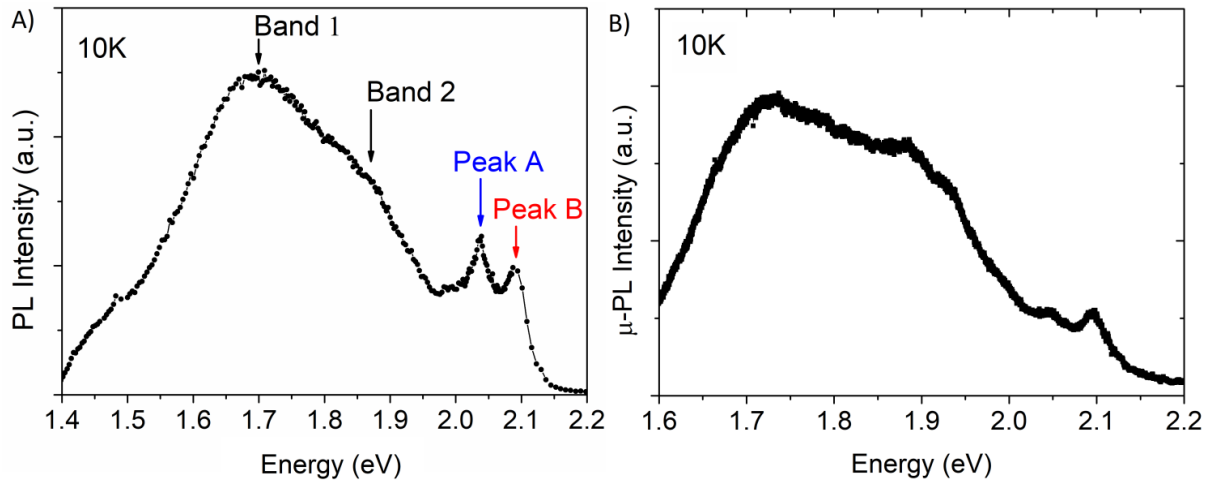
Figure 4.9 (a) Typical PL spectrum acquired at 10 K of WZ GaP structure and low excitation density (8.0 W/cm^2). The main narrow and broad emissions are named as band 1 (~ 1.68 eV), band 2 (~1.88 eV), peak A (2.04 eV) and peak B (2.09 eV). (b) μ-PL spectra acquired at 10K of WZ GaP NWs acquired at low excitation density (0.8 W/cm^2).

These emission bands have already been reported for WZ GaP NWs [41]. However, no systematic study about their physical origins has ever been reported. Similar PL signature is also obtained in our μ-PL measurements from a single NW, Fig. 4.9b, indicating that the macro-PL spectra of as-grown samples reproduce those of the individual WZ GaP nanostructure rather than from the ZB phase GaP thin film, which is grown simultaneously on the substrate. Similar spectra were obtained analyzing several NWs; the only difference was a different ratio between the four main emissions labeled in Fig. 4.9a.

4.5 Power dependent PL

Figure 4.10a,b shows the PL spectra as a function of excitation power.
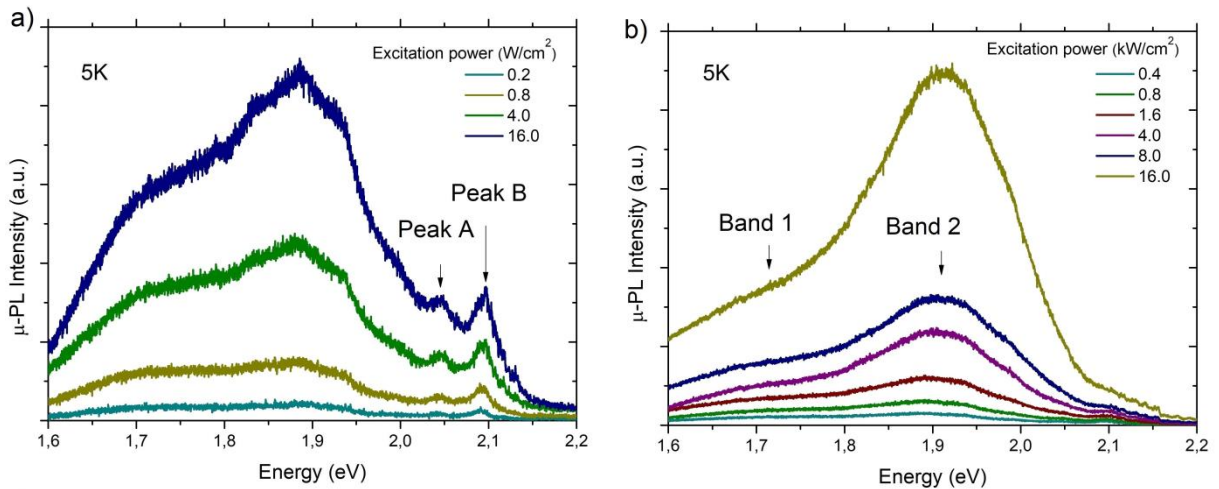
Figure 4.10 μ-PL of WZ GaP structure acquired at 5 K as function of excitation power. (a) in the low power regime (< 0.1 kW/cm^2). (b) in the high power regime (> 0.1 kW/cm^2).

We notice distinct behaviors in two regimes, for low (intensity < 0.1 kW/cm^2), Fig. 4.10a, and high (intensity > 0.1 kW/cm^2), Fig. 4.10b, excitation powers. For high excitation power regime, bands 1 and 2 dominate the spectra, while emissions A and B become much weaker than bands 1 and 2.

Power excitation dependence of the integrated PL intensity of narrow peaks, A and B, is shown in Fig. 4.11. We observe that they follow a power law behavior with exponent n $\leq$ 1 (eq. 4.1), which is characteristic of impuritiy emissions as (D-A) pair or donor-band (band-acceptor) recombinations [150, 99]:

$$I_{PL} = P^n , \quad \text{(eq. 4.1)}$$

where I_{PL} is the integrated PL intensity and P is the excitation power. In addition, a strong blue shift of few mili-eV was also observed for peaks A and B (Fig. 4.11).
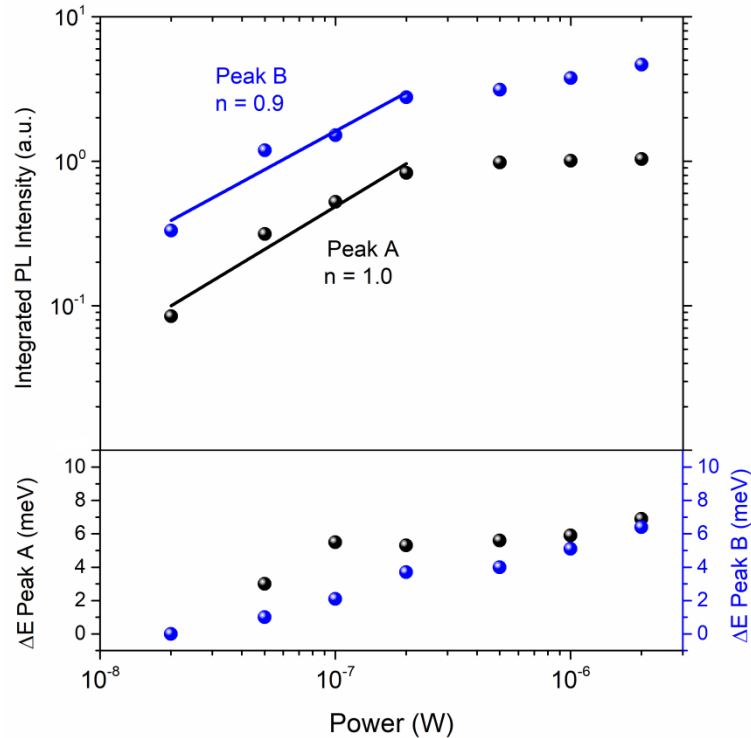
Figure 4.11 Integrated μ-PL intensity of peak A and B as function of excitation power in the high power regime (> 0.1 kW/cm^2).

4.6 Temperature dependent PL

Fig. 4.12 shows the μ-PL spectra of a single NW as a function of temperature. Rapid quenching of peaks A and B occurs at low temperature range, below 100 K, followed by band 1 at higher temperature; for temperatures above ~150 K, PL spectra are dominated by band 2 emission. The quenching of peaks A (at ~ 100 K) and B (at ~ 90 K), Fig. 4.12 and 4.13a,

indicate that shallow impurities should be involved in these emissions. At 200 K and also at room temperature (not shown here), a very weak signal at 2.18 eV is also observed, Fig. 4.12.
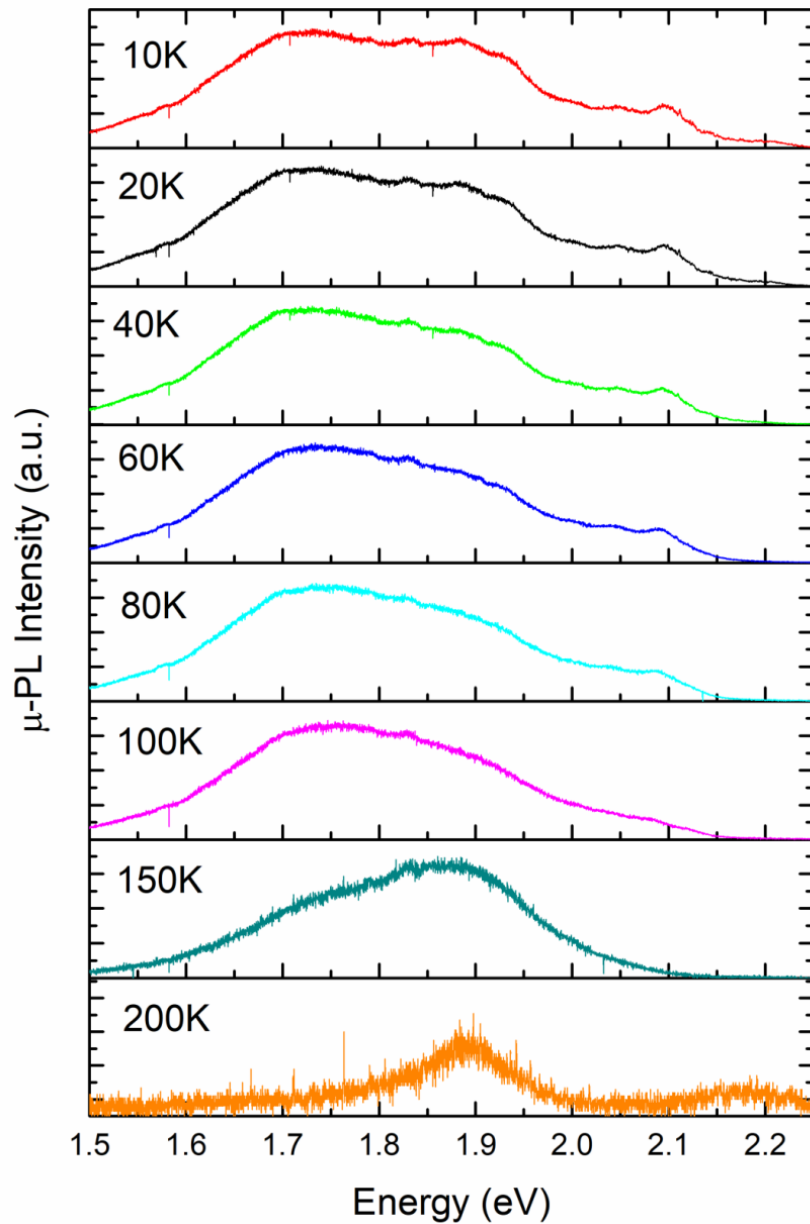
Figure 4.12 Temperature dependent μ-PL spectra acquired in the range 10 K – 200 K and low excitation density (8.0 W/cm^2) of WZ GaP structure.

In order to identify the impurities involved in the narrow peaks, A and B, we have estimated the ionization energies using an Arrhenius plot of the integrated PL intensity, Fig. 4.13a,b. The narrow peaks A and B were best fitted using two radiative recombination channels:

$$I = \frac{I_0}{1 + C_1^{A,B} e^{\frac{-E_1^{A,B}}{k_B T}} + C_2^{A,B} e^{\frac{-E_2^{A,B}}{k_B T}}} \,, \quad eq.\,(4.2)$$

where k_B is the Boltzmann constant, $C_1^{A,B}$ and $C_2^{A,B}$ are constants and E_1^A (E_1^B) and E_2^A(E_2^B) are the ionization energies of the impurity levels involved in the emission of peak A (peak B). For both bands we obtained two very distinct ionization energies: for peak A, $E_1^A = (68 \pm 8)\ meV$ and $E_2^A = (9 \pm 1)\ meV$ and for peak B, $E_1^B = (82 \pm 12)\ meV$ and $E_2^B = (6 \pm 1)\ meV$, as indicated in Fig. 4.13b.
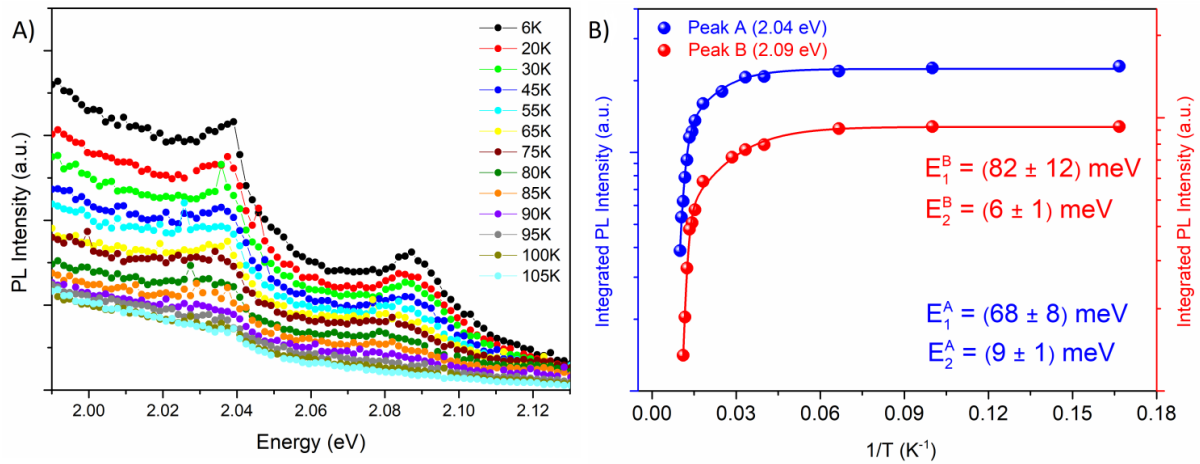
Figure 4.13 (a) Temperature dependent PL spectra acquired at low excitation density regime of WZ GaP NWs. (b) Integrated μ-PL Intensity of the peaks A (2.04 eV) and B (2.09 eV) as a function of reciprocal temperature.

The broad band emissions 1 and 2 are related to different impurities, what prevents a similar analysis. However, Fig. 4.12 shows that band 1 emission at 1.68 eV quenches before band 2 at 1.88 eV. This means that band 1 involves at least one impurity that is shallower than those related to band 2. We can see in Fig. 4.14 a red-shift in energy position of peaks A and B due to the decrease of the band gap with temperature, which seems to follow the phenomenological Varshni law, for the behavior of the band gap with temperature [151].
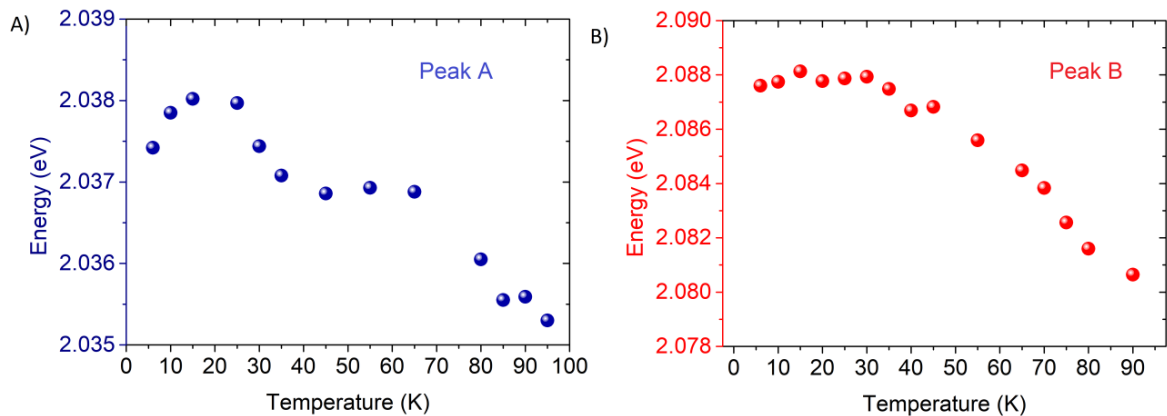
Figure 4.14 Energy values of peaks A and B as function of temperature in the range 5 – 100 K.

4.7 Excitonic recombination

Analyzing the large WZ GaP structure by µ-PL at low temperature and high power excitation regime (in this case, increasing the excitation density by three orders of magnitude), additional sharp peaks in the range of 2.13 –2.22 eV appear, Fig. 4.15.

Interestingly, the peaks at 2.140 eV and 2.155 eV remain constant when measurements were acquired at different regions along the structure. Meanwhile, other peaks appear or disappear at different energies as illustrated in Fig. 4.15a,b, which shows the µ–PL spectra versus excitation density measured on a different position along the structure. Assali et al. [152] attribute the sharp lines observed in that spectral range to quantum confinement effects around stacking faults.
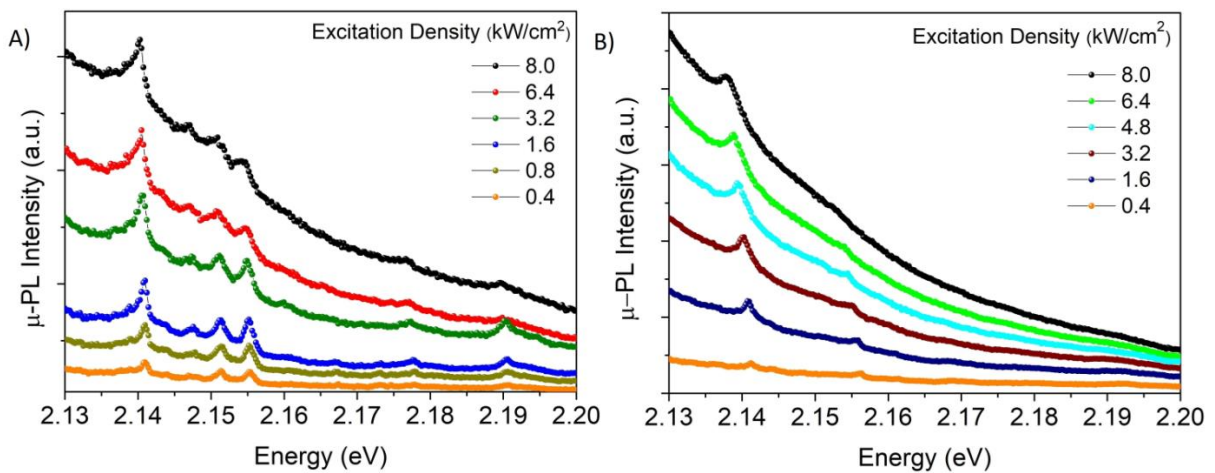
Figure 4.15 5K µ-PL spectra under different excitation densities and high power regime (≥ 0.1 kW/cm^2) in different positions across the large WZ GaP structure. (a) at top segment. (b) in the middle of the strcture.

However, the peaks at 2.140 eV and 2.155 eV, which are present in the entire GaP structure, rapidly saturate under high excitation power, as shown in Fig. 4.15a,b and 4.16. Therefore, these two emissions should not originate from locally formed crystalline defects, and are representative of all WZ GaP structure, with a distinct origin.

Careful analyses of the emission at 2.140 eV shows that this peak has a FWHM of ~ 1 meV (our resolution limit) and increases in intensity with excitation density following a power law with exponent n = 1.0, as we can see in Fig. 4.16. Therefore, this emission could be attributed to an excitonic recombination [99]. Moreover, the emission seems to saturate, indicating bound excitons, which are in agreement with the previous results of Assali et al. [55] Therefore, our results suggest that these bound excitons are associated with a point defect – most likely impurities – generated during growth. Furthermore, this intrinsic contamination

should not originate from the substrate, as previously suggested in the work of Assali et al. [153], because we have used a different substrate. In our case GaAs was employed, instead of GaP.
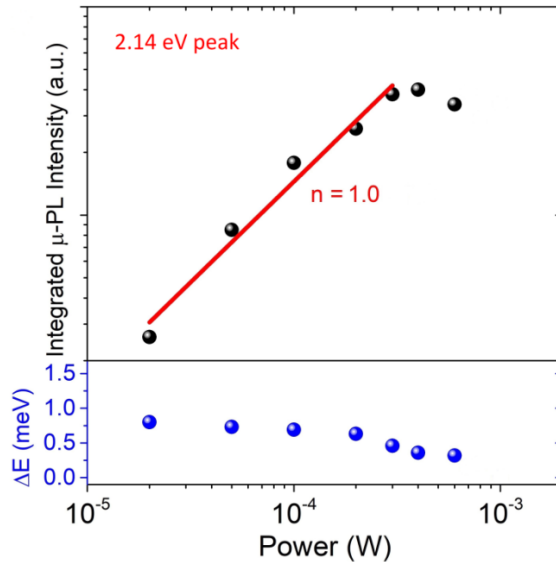
Figure 4.16 Integrated μ-PL intensity and energy shift of the peak at 2.14 eV as a function of the excitation power.

On the other hand, the peak at 2.155 eV saturates very quickly with excitation power. The background generated by deep level emissions dominates the spectra and the peak at 2.155 eV is smoothened out, Fig. 4.15b. However, this emission does not depend on position along the structure, as we can see in Fig. 4.15 for the μ-PL acquired at different points across the GaP structures axis; for that reason we also attribute it to a bound exciton. It is interesting to note that, in the PL spectra of Fig. 4.15b, additional sharp emissions appear below ~ 2.155 eV and are equally spaced within ~ 4 meV. Similarly, the emission at 2.19 eV is also accompanied by two very weak emissions separated by ~ 10 meV. This energy separation and the local dependence of all these minor peaks suggest a relationship to stacking faults; these defects create quantum wells of ZB monolayers in the WZ matrix [152]. Therefore, their emission energies depend on the number of zinc blend (ZB) monolayers in each well, so that emissions are separated by multiples of ~ 5 meV. Thus, the local dependent emission observed in Fig. 4.15a,b is attributed to the presence of these quantum wells.

4.8 Dependence of PL with position on asymmetric WZ GaP NWs

The μ-PL analysis along the GaP structure axis (large volume nanowire) is shown in Fig. 4.17. Interestingly, the spatial dependence of the PL spectra is very clear. Depending on

the position where the spectrum is acquired, band 2 overlaps peaks A and B. Thus, we will focus in bands 1 and 2.

Figure 4.17a depicts two PL spectra acquired at two extremities, at the base and top, of a single nanowire. In Fig. 4.17b we summarize the results for all spectra, by showing the plot of the integrated intensity (normalized to the sum of both bands, 1 and 2) as a function of the position along the nanowire, starting from the tip. The intensity normalization compensates for the volume variation along the structure. The intensity of band 2 is much stronger than for band 1 around the tip; surprisingly, however, band 1 intensity drops abruptly at the position ~ 6 µm from the base (which may not be exactly at the base of the as-grown nanowire).
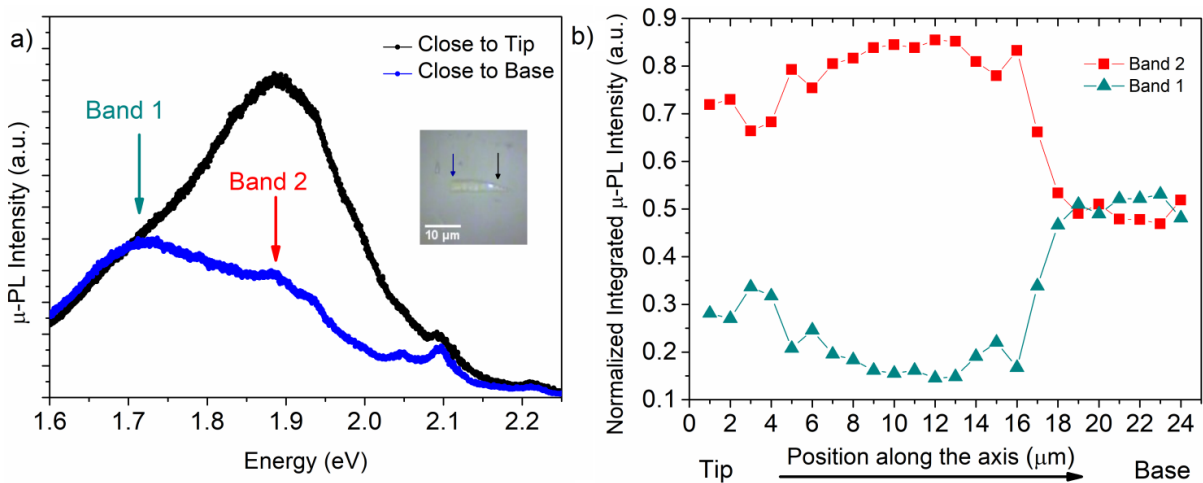
Figure 4.17 (a) µ-PL spectra of the large WZ GaP structure grown for 6 h acquired at 5K and low excitation density regime (8.0 W/cm^2) in different positions across the axis of the structure. The broad emissions observed below 2.0 eV, as band 1 centered ~ 1.68 eV and band 2 centered at 1.88 eV are indicated by green and red arrows, respectively. Inset: optical microscopy image of the WZ GaP structure transferred to a Si substrate, showing the positions where the measurements were performed. The blue and black arrows in the inset indicate where the spectra were acquired, at the basis and tip segments, respectively. (b) Normalized µ-PL intensities of band 1 in green (as indicated in (a)) and band 2 in red (as indicated in (b)) as a function of the position along the structure.

This abrupt variation suggests that the density of impurities or defects involved in band 2 emission varies across the WZ GaP structure. We suspect that this behavior originates from the effects of the different growth mechanisms close to the NP.

4.9 Dependence of PL with growth conditions of asymmetric WZ GaP NWs

We have also analyzed the effect of growth conditions on the overall PL spectrum of the WZ GaP nanowires. We have measured the macro-PL of nanowires grown for 1 h, as

described in chapter 3 for different TEG and PH$_3$ flows. First, we have studied the effect of changing TEG flows while keeping the group V flow constant, Fig. 4.18.
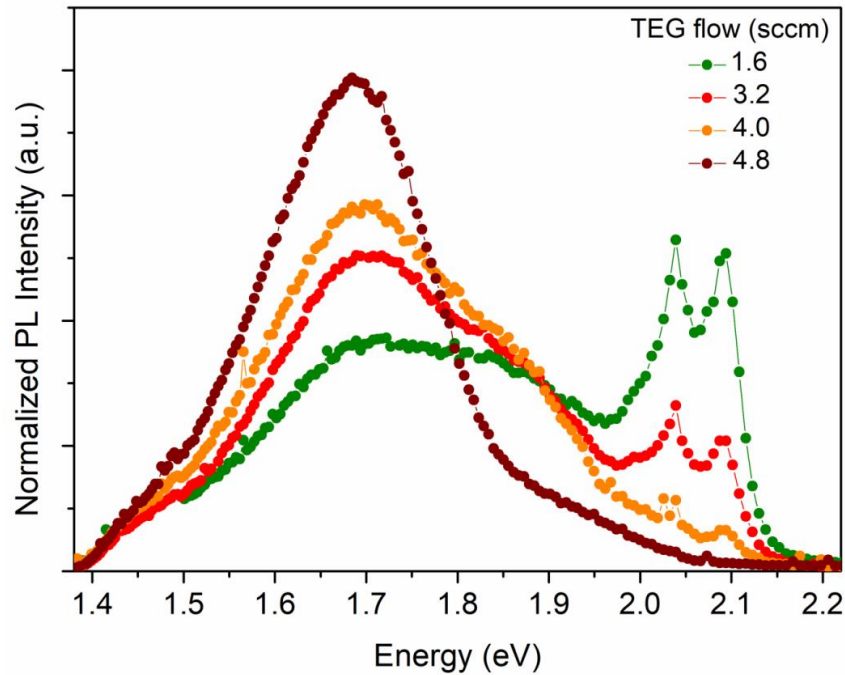
Figure 4.18 Normalized PL spectra of WZ GaP NWs carried out at 10 K and low excitation density (~ 1.5 W/cm^2) and different TEG flows. The spectra were normalized by the total area under the curve, in order to suppress volume effects on the relative intensities among samples.

The axial growth rates of GaP NWs are directly related to TEG flow. We have obtained samples with different nanowire lengths; the average NW length is about 10 μm for the highest TEG flow and 1 μm for the lowest. Thus, in order to compensate for volume variation among samples, all spectra were normalized using the integrated intensity.

In Fig. 4.18 we can notice that, for high TEG flows, band 1 emission, at 1.68 eV, dominates the spectra. As we reduce TEG flow, band 1 intensity decreases drastically, and band 2 emission slightly increases. On the other hand, no drastic modification on the PL spectra was observed when we change the group V supply (phosphine), Fig. 4.19, other than a small increase in band 2 emission. Therefore, the organometallic source can be considered as the main impurity source during growth.
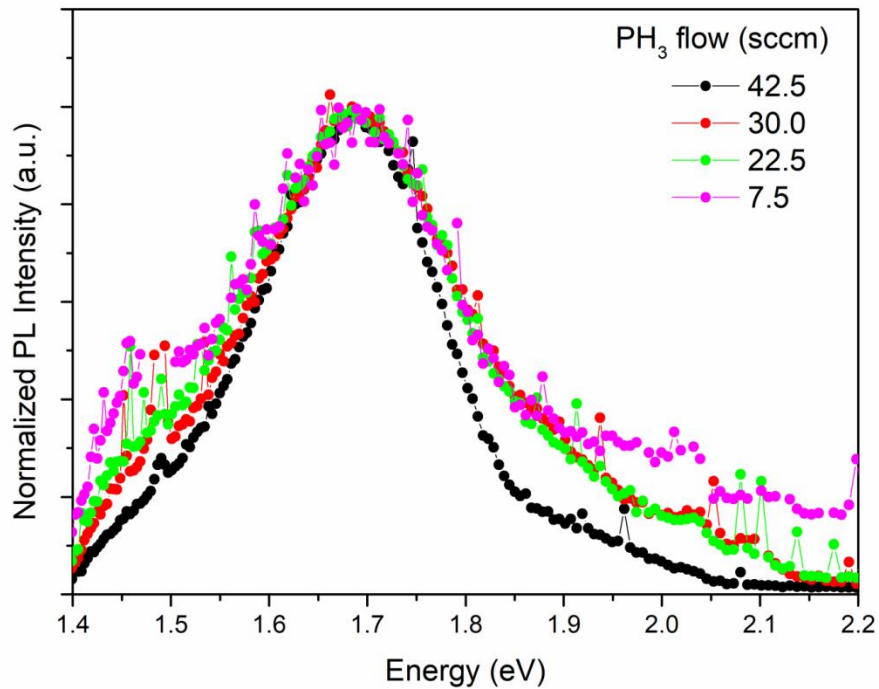
Figure 4.19 Normalized PL spectra acquired at 10 K of WZ GaP NWs acquired at low excitation density (~ 1.5 W/cm^2) of samples grown under different PH$_3$ flows. The spectra were normalized by the total area under the curve, in order to suppress volume effects on the relative intensities among samples.

Residual impurity incorporation in WZ GaP structures can also be evaluated by introducing a dopant with well known characteristics and studying how it affects the optical properties of the undoped material. In particular, Be is a well known shallow acceptor (Be$_{Ga}$) in ZB GaP, with ionization energy of (50 ± 1) meV [154]. Furthermore, doping is a key step for optoelectronic device fabrication. In this context, we have successfully grown Be-doped WZ GaP. Figure 4.20 shows the PL spectra as a function of the Be flux (as determined by Be cell temperature); the PL spectra are also normalized by the total area in order to compensate for variations in GaP volume.

We can see in the inset of Fig. 4.20 that the introduction of Be does not affect the growth dinamics, i.e., we still obtain WZ GaP nanowires with the characteristic asymmetric morphology. In all PL spectra of Be-doped samples, the enhancement of the peak at 2.03 eV is evident, where the peak position is very close to the peak A. It can be thus unambiguously attributed to a transition involving Be acceptor.
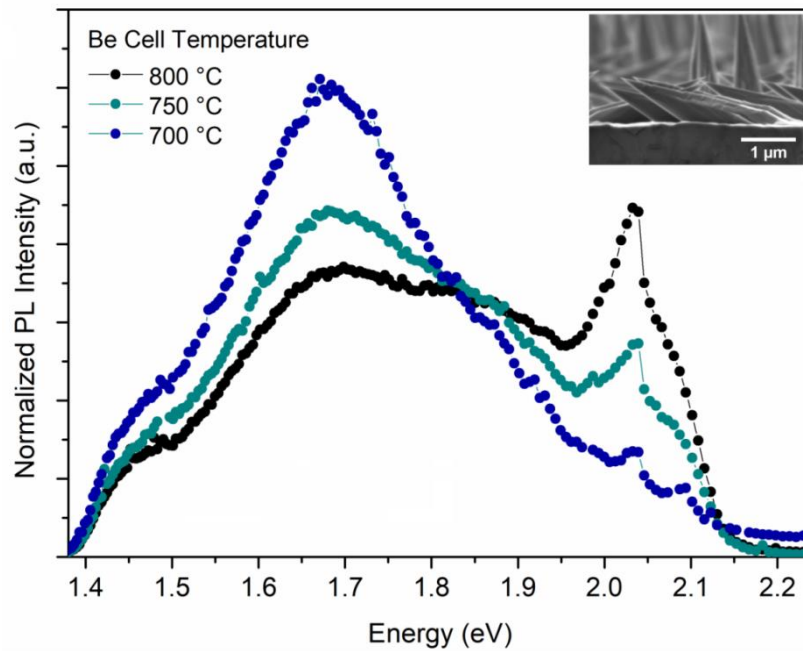
Figure 4.20 (a) Normalized PL spectra of Be doped WZ GaP NWs acquired at 10 K and at low excitation density (~ 1.5 W/cm^2) for different Be content (Be cell temperature). The spectra were normalized by the total area under the curve, in order to suppress volume effects on the analysis of relative intensities of the samples. Inset: Side-view SEM image of Be-doped (800 °C) GaP NWs.

4.10 Probing electronic band structure of GaP WZ phase by Photoluminescence Excitation Spectroscopy

The electronic band structure has been probed using PL and PLE spectroscopy performed at 10 K, presented in Fig. 4.21. We have used the large WZ GaP structures, in order to improve the signal/noise ratio. The PL spectrum shows a strong, broad band and two sharp lines, typical emissions observed in WZ GaP NWs, as discussed until now. The detection of PLE experiments was monitored at 1.68 eV from the broad band and, in order to improve the signal, we have used as well a large aperture slit in the single-monochromator (2 mm). Here, we consider that excited electrons fast thermalize and there is no trap in non-radiative states, which means that, in this case, the PLE spectrum resemble the optical absorption.
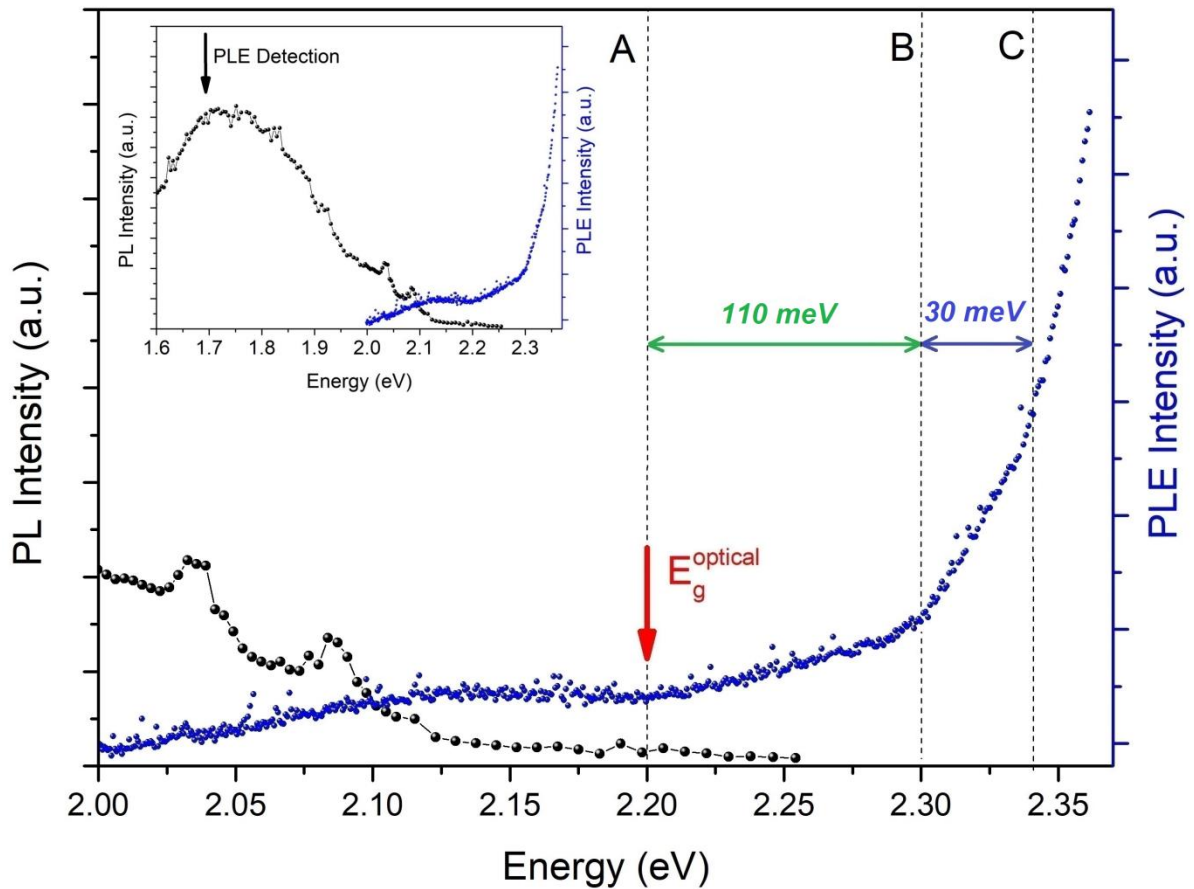
Figure 4.21 PL and PLE spectra of the GaP structures performed at 10 K; dashed lines indicate the absorptions edges labeled *A*, *B* and *C*. Inset: the same PL and PLE spectra with broad range. The black vertical arrow indicates the detection position at 1.68 eV, used in PLE measurements. PLE was acquired using the maximum of the single monochromator aperture slit (2 mm) and a long integration time (12 s), in order to increase the signal/noise ratio of the first absorption edges.

As we can see from the PLE signal in Fig. 4.21, a weak absorption starts at 2.00 eV, continues to be observed up to 2.10 eV and then decreases. This unexpected absorption, observed below the estimated band gap at 2.19 eV [55], could be associated to impurity absorption. Indeed, impurity based emissions, as peaks A and B, at 2.04 eV and 2.09 eV [41, 55], are very clear in this energy range, as we can see in the PL spectra, inset of Fig. 4.21.

However, the most interesting results in the PLE spectra are the successive absorption edges shown in Fig. 4.21: a very weak edge at (2.19 ± 0.02) eV, which is in good agreement with the experimental band gap value reported by Assali et al. [55]; and two stronger absorptions at (2.30 ± 0.03) eV and (2.33 ± 0.02) eV. The quantitative analysis for the determination of the energy thresholds is presented in the appendix E.

In Fig. 4.22 the single monochromator slit, that is coupled to the Xe lamp, was reduced from 2 mm to 0.75 mm in order to increase the spectral resolution. The resulting PLE spectrum shown in Fig.4.22 presents an excitonic-like peak at ~2.318 eV, that is just below the absorption onset at 2.33 eV, leading to an estimate exciton binding energy of 12 meV. In addition, it is clear that the absorption edges *B* and *C* have strong oscillator strengths, due to their parabolic increase with energy.
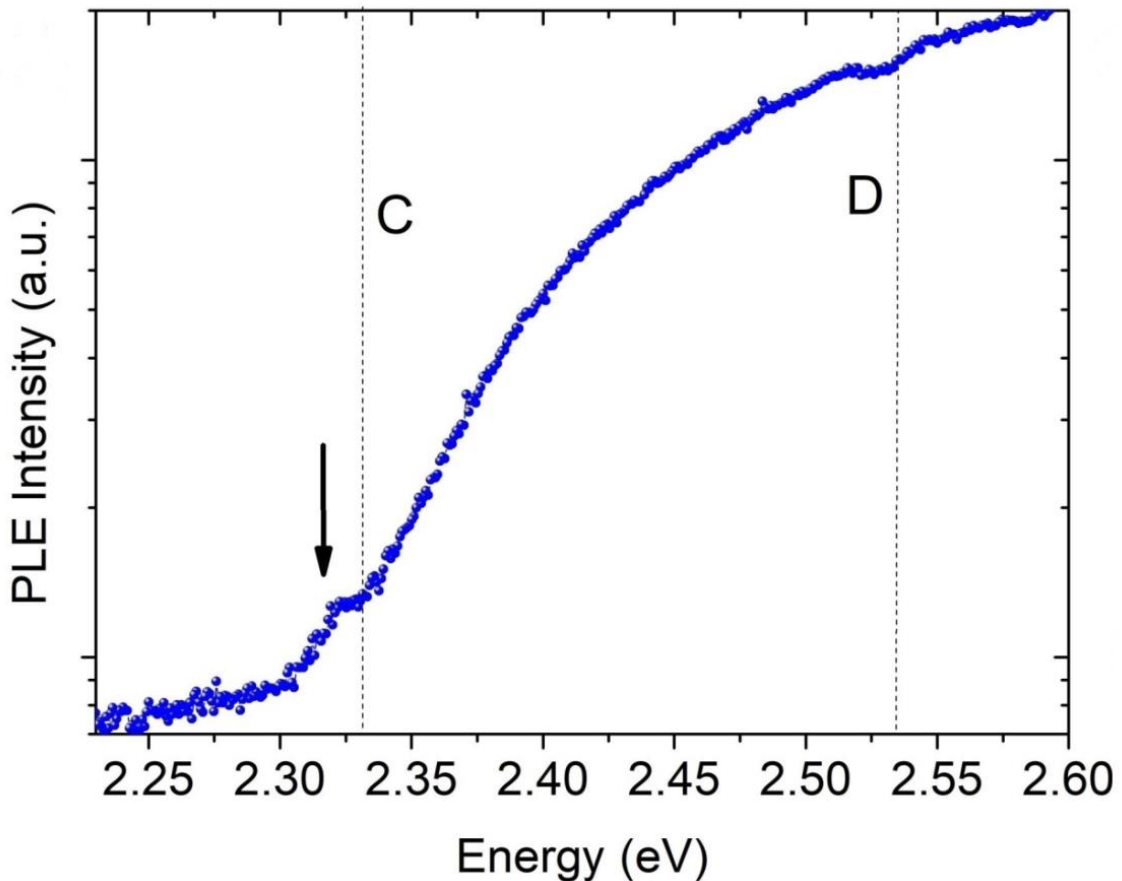
Figure 4.22 PLE performed with Xe lamp single monochromator aperture slit of 0.75 mm; additional absorption edge was observed at high energy and labeled *D*. The black arrow indicates the excitonic peak observed for transition *C*.

Figure 4.22 also shows an electronic transition at 2.54 eV, which could be related to the transition involving the second conduction band and the top of the valence bands. The electronic transitions observed are summarized in Fig. 4.23. The weak absorption edge measured for the first band-to-band electronic transition *A* is shown in dotted line due to the weak oscillator strength associated, while the others eletronic transitions *B*, *C* and *D* are represented in solid lines due to the stronger oscillator strength observed. Moreover, the valence

band splitting measured between the three highest valence bands were, 110 meV and 30 meV, respectively, Fig 4.23.
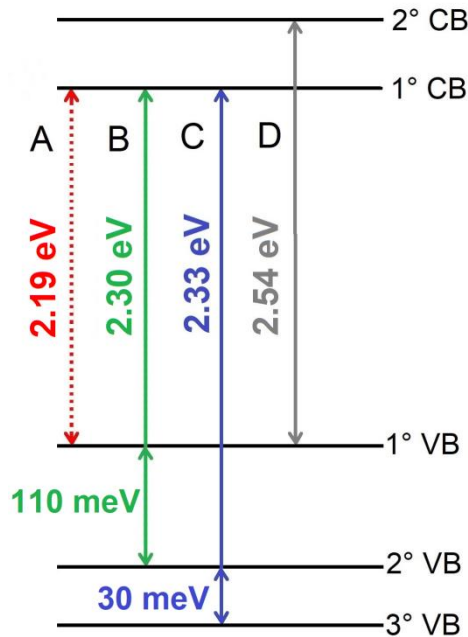
Figure 4.23 Schematic representation of the first absorption edges observed in PLE measurements. Dotted (solid) lines indicate the weak (strong) absorption edges with monotonic (parabolic) increase with energy.

4.11 Interpretation of the experimental results

4.11.1 Measuring the band gap and the absorption edges

The fundamental band gap of the WZ GaP nanowires has been experimentally estimated in previous reports in the range 2.09 - 2.19 eV, based on PL measurements [1, 55, 57]. Thus, combining our experimental results with the previously reported data, we can conclude that there is a threshold for the absorption, i.e., a band gap at $E_g = (2.19 \pm 0.02)$ eV at 10 K for the WZ phase.

Moreover, interesting features can be pointed out. First, the lowest band-to-band absorption edge, labeled as *A* in Fig. 4.21 and 4.23 (dotted lines), is very weak with a monotonic increase in energy. On the other hand, the absorptions related to *B* and *C* transitions are much stronger than *A*, especially for the *C* transition, with the presence of an excitonic-like peak (Fig. 4.22). The energy dependence of the absorption spectrum above the excitonic-like peak behaves as a typical three-dimensional (3D) parabolic band transition [155] around the edge. These observations points leads to a large oscillator strength, expected for the *C* transition.

The optical absorption of semiconductors can be used as a fingerprint for the nature of the bandgap. For instance, the direct allowed transition (typical direct gap semiconductors) shows a strong, abrupt and concave absorption edge at the band gap [155, 156]. On the other hand, indirect as well as direct forbidden transitions (so-called pseudo-direct gap) show a slow, convex-shaped increase in energy [155, 157, 98]. In addition, indirect gap transitions require phonon emission and, as the pseudo-direct transitions, should show much weaker absorption than direct band gap transitions. With that in mind, the results reported in Fig. 4.21 can be understood as a direct observation of the dipole forbidden (pseudo-direct) band gap nature of the WZ phase in GaP.

In order to analyze in more detail the absorption edges of the PLE spectra, it is important to compare the experimental data with available theoretical results [40, 137, 53, 54] Belabbes and Bechstedt have predicted the WZ GaP band gap at 2.12 eV and an almost forbidden fundamental transition, which would behave as a pseudo-direct band gap semiconductor. Analyzing the reported theoretical results of the wave vector dependence of the optical transition matrix element, it is clear that the dipole matrix element corresponding to the fundamental transition is non-null at the Γ-point, but is very small for the wave function perpendicular to the c-axis and it increases only for a certain wave vector k, as reported by Belabbes and Bechstedt [54]. This is consistent with the quite weak absorption band observed around the gap (band A), at 2.19 eV. Belabbes and Bechstedt [12] also suggested that the optical transitions observed in the previous experimental data do not strictly follow k-vector conservation, since the disorder introduces non-conservation of k. A similar analysis can be carried out for the absorption bands B and C, for which the expected matrix element at k = 0 is also negligible.

However, much stronger absorption is observed for these bands as compared to the band A, indicating that this model cannot explain all absorptions. Furthermore, the theoretical description by Belabbes and Bechstedt [54] provides valence band splitting values predicted as Δ_{AB} = 42.5 meV and Δ_{BC} = 175 meV. Therefore, the splitting between A and B bands is smaller than between B and C, contrarily to our experimentally observed behavior, i.e., $\Delta_{AB} > \Delta_{BC}$ with Δ_{AB} = 110 meV and Δ_{BC} = 30 meV reported here.

In order to clarify this discrepancy, our collaborator Prof. Dr. Guilherme Sipahi from the University of São Paulo (São Carlos), has calculated the band structure of WZ GaP phase using DFT implemented in the VASP code with a different functional, i.e., the HSE06 functional, which provides a realistic band gap ordering. Fig. 4.24 shows that the predicted band

gap energy was 2.10 eV, which is close to the previously calculated [40, 54] and measured results [55, 57] as well as to the data presented here. Also, the calculated energies splitting between the three highest valence bands were 230 meV and 110 meV, respectively. These values, despite being overestimated, are in qualitative agreement with our experimental data ($\Delta_{AB} > \Delta_{BC}$).
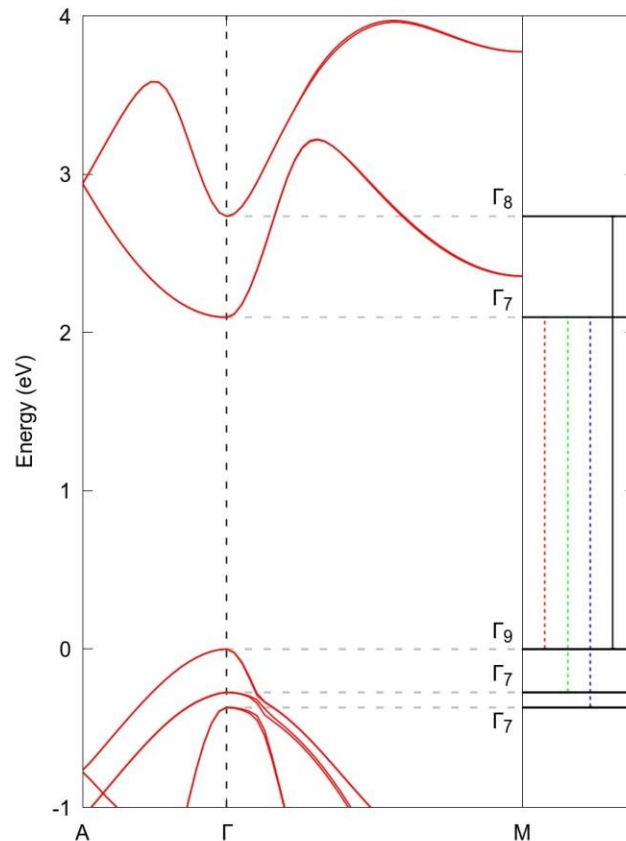
Figure 4.24 Electronic band structure of the WZ GaP calculated by DFT method using HSE06 functional. The band gap predicted was $E_g = 2.10$ eV, and the valence band splitting between the highest valence bands were 230 meV and 110 meV, respectively. Data calculated by our collaborator Prof. Dr. Guilherme Sipahi and research group.

Furthermore, this model provides an inversion between the conduction bands; the lowest energy conduction band, in this case, is the Γ_7 band with p-orbital contribution, while the higher one is Γ_8 s-orbital. In this case, the measured *A*, *B* and *C* absorption edges should correspond to the transitions involving Γ_9, Γ_{7+}, Γ_{7-} valence bands and Γ_7 conduction band. However, regardless of this band inversion, the three lowest energy electronic transitions are still dipole-forbidden at the center of the Brillouin zone, as reported by Belabbes and Bechstedt [54]. In our electronic band structure of the WZ GaP, the first allowed transition is between Γ_9 and Γ_8, as shown in Fig. 4.24. Therefore, the partial breakdown of the selection rules – usually

related to the presence of impurities and crystal defects - is required to explain the transition observed here.

In our case, PL spectra (inset in Fig. 4.21) clearly shows that impurities and/or point defects are present in the material, leading to broad band emissions below 2.0 eV. Thus, the excess of these impurities may lead to the partial breakdown of the k-selection rules. It is important to notice that Belabbes and Bechstedt [54] also explored this possibility in their models; however, the qualitative agreement for the experimental valence band splitting behavior presented here indicates that the electronic band structure shown in Fig. 4.24 may provide a better description of the absorption data of Fig. 4.21 and 4.22. Nevertheless, the exact distinction between the two electronic band structure models is not possible from the optical absorption data alone.

4.11.2 Identification of residual shallow and deep impurities

In order to understand the physical origins of the optical emissions observed, which dominate the spectrum of the WZ GaP NWs and are associated to residual impurities during growth, we discuss the possible candidates of impurities using the optical data presented until now. In table 4.2 we present some ionization energies of shallow and deep impurities for ZB GaP whose values may be of the same order of magnitude as WZ, which has not been reported yet.

Impurity	Ionization Energy $E_{A,D}$ (meV)
S (donor)	102
Si (donor)	80
Si (acceptor)	203
Cd (acceptor)	96.5
C (acceptor)	48-54
Zn (acceptor)	64
V_{Ga}	300-340
P_{Ga}	450

Table 4.2 – Ionization energies of shallow and deep levels introduced in ZB GaP, extracted from [158, 159, 160].

We first notice that the very small values obtained for the ionization energy (E_1^A and E_1^B) in Fig. 4.13 are not matched with those for the shallow impurities expected for GaP presented in Table 4.2, and their origin is not clear yet.

We tentatively attribute peak A to Zn acceptor, since its ionization energy (64 meV) is close to $E_2^A = (68 \pm 8)$ meV. Moreover, as we have shown in Fig. 4.11, the strong blue shift and the power law with exponent n = 1 suggest that peak A corresponds to a Donor-Acceptor (D-A) recombination. Thus, analyzing the main shallow donors in Table 4.2, both Si and S could fit the role. However, Si presents lower ionization energy than S, and it is energetically more compatible with the observed transition energy, 2.04 eV. Residual impurities Zn and Si are usually observed as unintentional impurities in growth systems where organometallic sources are employed, as observed for GaAs [140, 161, 142, 162]. Therefore, it is reasonable to expect that peak A is related to (D-A) pair recombination involving Si donors and Zn acceptors.

With regard to peak B (2.09 eV), we have obtained a large value of $E_2^B = (82 \pm 12)$ meV which is close to the Si donor ionization energy. Adding this value to the PL peak energy, the total value is almost the gap energy (2.19 eV) [55]. The ionization energies of shallow impurities shown in Table 4.2 present values above ~ 50 meV, which makes a (D-A) recombination energetically inconsistent for peak B. Moreover, it is well known that the (D-A) peak is usually followed by the free-to-bound (FB) recombination peak at higher energy range, such as band-to-acceptor $(FB)_A$ or donor-to-band $(FB)_D$ transitions. In our case, the energy separation between peak A and B is 50 meV; this value is close to the ionization energy (68 $\pm$ 8 meV) of Zn_{Ga} acceptor. Here, we should mention that C_p could also be the acceptor in the D-A transition, since the ionization energy ~ 50 meV agrees with energy difference between peak A and peak B. However, we assume here that Zn is the most probable acceptor involved since the ionization energy estimated for peak A is much closer to the value for Zn in ZB material. Therefore, the emission of peak A is attributed to the $(FB)_D$ recombination involving a Si donor. Even though energies do not perfectly match in this case ($E_g - E_{Si} = 2.108$ eV), we have a relatively large uncertainty in the estimated ionization energy, which is typical for Arrhenius plots of PL peaks. Moreover, we should keep in mind that donor ionization energies in WZ and ZB GaP phases can be slightly different, due to the character of the semiconductor band gap in each case. Thus, considering these points, we tentatively associate peak A emission with a Si donor – band recombination.

Furthermore, unintentional impurities from TEG should be present in a very small amount. In fact, as we have shown in Fig. 10a,b, peaks A and B quickly saturate with increasing excitation power, while bands 1 and 2 do not. In other words, the broad emissions 1 and 2 are related to a more constant or abundant impurity source during growth than those involved in A and B transitions, which in this case could be, for example, crystal point defects.

Now we focus on the point defects (such as host atom vacancies, anti-sites and interstitials). It is well known that growth is limited by group III precursor (Ga in our case). Thus, when the length of the NW exceeds the diffusion length of the TEG species (Ga), fewer Ga atoms can reach the region above this length along the NW, and Ga vacancies (V_{Ga}) can be formed. This interpretation could be related to the behavior observed in Fig. 4.17a,b, and the increase of band 2 at the top of the structure could be explained due to the high density of V_{Ga} in the top segment, compared to the basis of the GaP structure.

This type of point defect in III-V semiconductors commonly presents emission related to donor-vacancy complexes, such as donor-V_{Ga} complex in GaAs (~1.2 eV) [163]. The ionization energies of both V_{Ga} and donor-V_{Ga} complexes are not available for WZ GaP; in the case of ZB GaP, this energy has been predicted as 300 - 380 meV for V_{Ga} [159]. The difference between the WZ band gap (2.19 eV) [55] and the band 2 peak energy (1.88 eV), 310 meV, lies within that range. This result also suggests that this emission band is related to a V_{Ga}, or donor-V_{Ga} complex recombination.

In the case of band 1 (1.68 eV), we suspect that a different deep level point defect, such as P anti-site (P_{Ga}). This is a likely candidate, considering the expected emission energy. The P anti-site (P_{Ga}) defect should introduce a double donor state, and available theoretical data indicates that the ionization energy is 0.45 eV below the minimum of the ZB GaP conduction band [160]. The impurities associated to (D-A) recombinations have been most likely introduced during growth from TEG organometallic source, like the most abundant C as well as other residual impurities such as Zn and Si. Here, we should mention that, although C has an amphoteric behavior and could be incorporated as donor or acceptor in III-V semiconductors, it is well known that C is most likely incorporated as acceptor. Thus, the formation of a donor-acceptor pair involving this point defect and C as an acceptor (ionization energy ~ 50 meV) should originate an emission at 1.69 eV if we neglect the Coulomb interaction between the ionized impurities. This value is very close to band 1 emission. In addition, C as well as V_{Ga} and P_{Ga} are impurities/point defects that are abundant during growth and do not depend of any

external source, since C comes from TEG and point defects are intrinsically generated, in different concentrations, in a crystal growth process.

Concerning the Be-doped GaP NWs, we have noticed that Be doping also affects the emissions of band 1 and 2. We can see from Fig. 4.21 that, unambiguously, the increase in Be content during growth enhances the emission at 2.03 eV. Thus, we tentatively attribute this emission to the (D-A) recombination involving Be acceptor and most likely Si as donor.

Therefore, we summarize the possible candidates for the four main emissions observed in Fig.4.25.
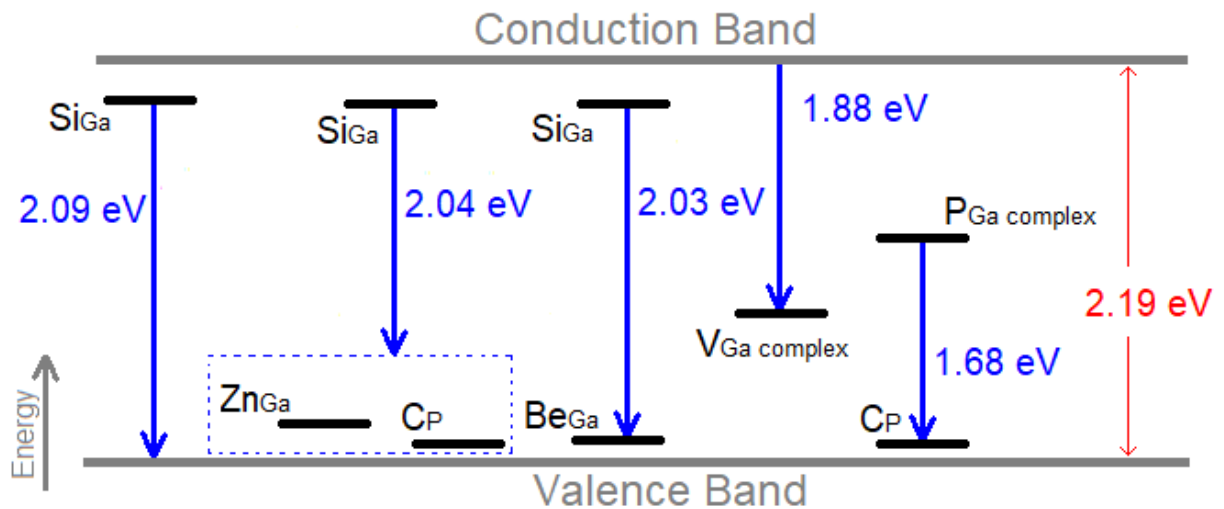
Figure 4.25 Band diagram of eletronic transitions due to shallow and deep levels observed in the WZ GaP nanowires and the proposed candidates for each impurity emission. We have highlighted with dotted lines the impurities that can not be univocally distinguished with the optical data analysis.

In this picture of the physical mechanisms behind the impurity emission of WZ GaP NWs, quenching of band 1 at lower temperatures than for band 2, observed in Fig. 4.12, is related to the ionization of C acceptor associated with band 1, while band 2 involves only a deep level related to V_{Ga}. At this point, we should mention that the small ionization energies found in the Arrhenius plot related to peaks A and B could be associated to nonradiative states originating from surface states, strain, etc, or even radiative states; thus, these peaks could involve an intermediate state. As shown in Fig. 4.13, peaks A and B are the first to quench at 100 K ($k_BT \sim 9$ meV) and 85 K ($k_BT \sim 7$ meV), respectively, due to the ionization of these unknown states, i.e., since this recombination stops, the subsequent recombination path cease. However, from the data presented here, it is not possible to determine the mechanism behind those small energies. In any case, the elucidation of the physical origins of these small

ionization energies does not affect our work and from this point on, we will focus on the larger ionization energies in the observed emissions.

In addition, Fig. 4.18 shows that deep levels, band 1 and band 2, exhibit a completely different behavior with increasing TEG flow. These opposite trends suggest a possible anticorrelation between band 1 emission and V_{Ga} density. Increasing organometallic precursor flows imply in larger C amounts in the growth environment. Based on our interpretation, we should expect band 1 emission to increase. In fact, as we can see in Fig. 4.18, providing more TEG during growth enhances the emission at 1.68 eV. When V_{Ga} is occupied by a P atom, band 2 optical emission may quench and band 1 emission may be enhanced. On the other hand, no drastic PL modification was observed when the group V (phosphine) supply is varied, (Fig. 4.19), since growth is always carried out under group V overpressure. Then, as we can see in Fig. 4.18, band 1 is the only emission that is not strongly reduced by changing precursor flows. This result supports the interpretation of a C-related emission, since C is the dominant impurity in CBE, originating from TEG. A more efficient way to reduce C incorporation and, hence, band 1 emission, would be raising growth temperature, therefore promoting the release of C from the alkyl group III species [164]. We have indeed observed that behavior, by growing the WZ phase at higher temperatures, using Ni catalysts, as we will discuss in the next chapter. All these observations show that the assignment of band 1 emission with P_{Ga} complex (donor) – C_p (acceptor) is in good agreement with the experimental results.

Lastly, regardless of the identification of the impurities involved in the observed emissions, it is important to mention that the results showed in Fig. 4.18 provide a rational way to control impurity incorporation. Enhancement of the narrow peak in the green/yellow spectral range, 2.04 eV and 2.09 eV, can be obtained for larger group III flows. The spectrum shown in Fig. 4.18 for the growth using 1.6 sccm TEG resembles the data reported by Assali et al. [41], where they initially assigned the emission at 2.09 eV to the band gap recombination [41]. However, despite the specific growth condition displayed, different samples have been reported with the suppression of deep level emissions below 2.0 eV [55, 165], but the understanding of growth mechanism related to that behavior has not yet been reported. Therefore, our results provide a pathway for any vapor-phase epitaxy system to control the impurity incorporation and, consequently, the luminescence of hexagonal phase GaP nanowires.

4.12 Conclusions

In summary, we have investigated in this chapter the optical properties of GaP nanowires in the hexagonal phase. Using PLE measurements, we have measured the absorption edges of this material, providing experimental evidence for WZ GaP eletronic band structure with three valence band splitting and DFT calculations provide support for PLE spectra taking place at the Γ point. Direct evidence that the bandgap is dipole forbidden with a band gap of (2.19 ± 0.02) eV at low temperature was also demonstrated, along with bound exciton recombination at 2.14 eV. Raman spectroscopy was used to probe the crystal structure as well as measure the vibrational modes of the unexplored WZ phase in GaP.

We have also studied the nature of the impurities and defects associated to the optical emissions in WZ GaP nanowires grown under different conditions. The photoluminescence spectra of this material is dominated by two broad emission bands and two relatively narrow peaks. We attribute the peaks at 2.04 eV and 2.09 eV to donor-acceptor pairs involving Si-Zn (or Si-C) and Si donor-band recombination, respectively. In addition, we report data suggesting that these residual impurities may come from the organometallic sources. Concerning the deep level emission and the broad bands below 2.0 eV, we associate them to point defects, as a transition between P_{Ga} antisite complex and C acceptor for 1.68 eV and band-Ga vacancy complex for 1.88 eV. Intentionally doped WZ GaP with Be produces an emission at 2.03 eV which was also studied, and attributed to a donor-acceptor pair recombination involving most likely Si as donor.

The understanding and the control of these impurities and defects are crucial for device fabrications as well as to determine eletronic/optical properties. Therefore, our results are a first attempt to reveal and control these unknown impurities involved on the luminescence of the WZ phase in GaP nanowires. They can also provide a pathway to optimize nanowire growth of metal-catalyzed WZ GaP using vapor phase techniques, since the source of these possible impurities are present in organometallic-based epitaxial systems, such as CBE and MOVPE. Our results also improve the knowledge concerning the basic electronic band structure parameters of this relatively new material.

Chapter 5

New catalysts for the epitaxial growth of III-V semiconductor nanowires

5.1 Introduction

For the last 60 years, gold (Au) has been popularly used as catalyst in the growth of III-V and goup IV semiconductor nanowires by the VLS growth mechanism [15, 25, 30, 166, 167, 168]. The use of gold as catalyst has many advantages: using gold, nanowires can be easily grown [27]; the crystal structure can be reliable controlled [168]; the development of complex nanostructures can be achieved [35, 167, 169] and the fabrication of several kind of device prototypes has also been demonstrated [19, 170, 171].

However, one the most interesting possibilities of III-V nanowires, which is the monolithic integration of III-V compounds on Si technology, is not a fully viable technology yet, despite intense fundamental and applied research on this topic [26, 172, 173, 174]. Silicon is a well known material, largely used in the microeletronic industry; therefore, the use of Si as a substrate can reduce costs. Moreover, integrating materials with higher carrier mobility and direct band gap, which means potentially efficient light emitters as III-V semiconductors, can boost Si-based microeletronic device performance by gathering unique advantages of each material on a single chip.

One of the most important drawbacks to achieve this goal using III-V nanowires is the fact that gold creates mid-gap states on Si, which can be problematic and affect Si transport properties, for example, reducing carrier mobility [175]. Therefore, it is important to search for alternative catalysts for VLS growth of III-V nanowires. Different approaches have been explored in literature such as the use of other metals, growth of self catalyzed nanowires and selective area epitaxy. In particular, interesting results concerning nanowire growth studies have already been demonstrated using Ag [176, 177, 178], Cu [179], Sn [75, 180], and Al [181, 182]. Moreover, in addition to the compatibility with Si technology, the introduction of new catalysts may lead to new functionalities as the bottom-up formation of p-n junctions without the introduction of dopants, as demonstrated for Sn-catalyzed GaAs nanowires [75].

In this chapter, we report our investigation, from the point of view of fundamental growth studies, on the synthesis of GaP and GaAs nanowires using tin (Sn) nanoparticles. Tin is a group IV element, as Si, thus, only introduce neutral doping centers in silicon. Moreover, the Sn-Ga system phase diagram [76] and the recently results demonstrated for GaAs nanowires [75, 180] indicate that Sn is a suitable material for the growth of III-V nanowires on Si than gold. We report here the growth of high aspect ratio Ga-based nanowires. However, we have also found Ni in the samples, and this unexpected result led us to investigate Ni as a possible catalyst as well.

5.2 The growth procedure

The growth of Sn-catalyzed nanowires was carried out using Sn nanoparticles produced by laser ablation in water solution, prepared in colaboration with Prof. Dr. Wido Schreiner, from the Federal University of Paraná (UFPR). The particles were deposited on GaAs(100), Fig. 5.1.
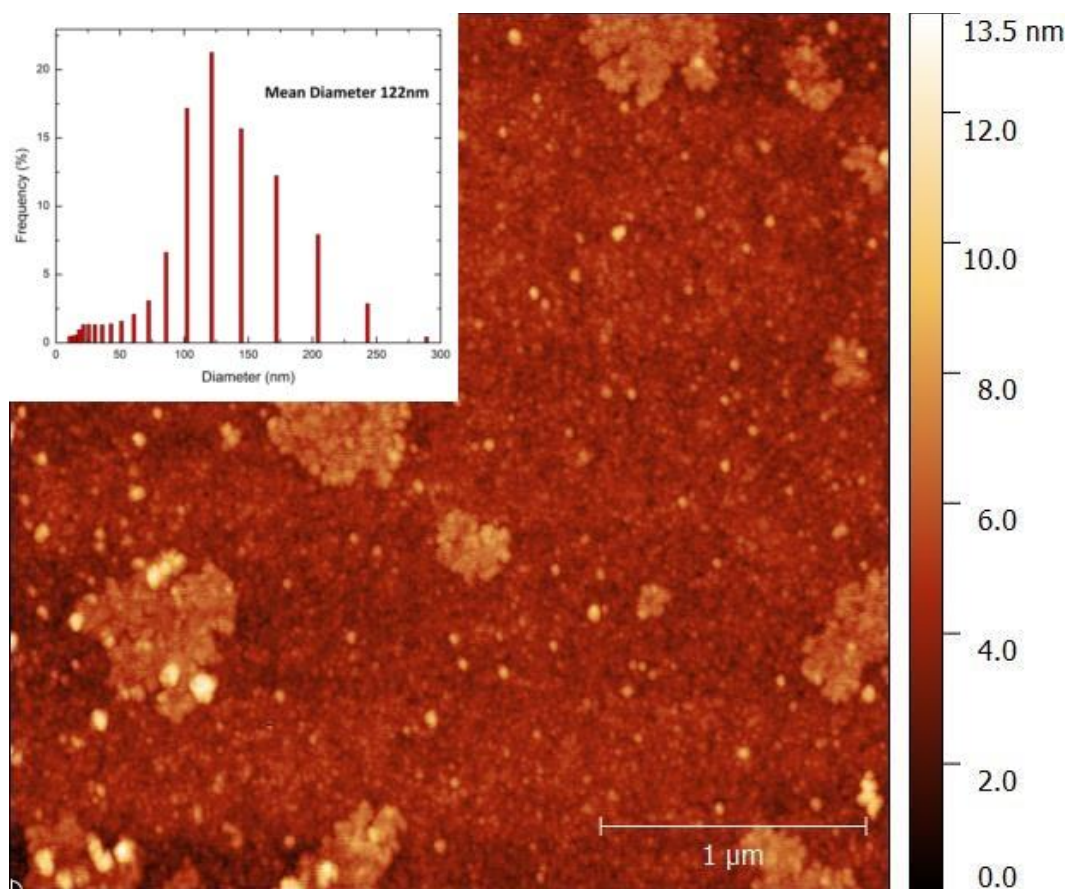
Figure 5.1 AFM topography image of Sn nanoparticles produced by laser ablation in water solution deposited on GaAs(100) substrate. Inset: Diameter distribution of the Sn NP's, measured by DLS (*Dynamic Light Scattering*) by our collaborators.

We can see in Fig. 5.1 individual Sn nanoparticles as well as cluster formation. The diameter distribution of the Sn NP's is shown in the inset of Fig. 5.1, and they are mainly composed by relatively large nanoparticles, with mean diameter 122 nm.

The growth of nanowires discussed in this chapter was performed as described in chapter 2 and 3. The nanowires were grown by chemical beam epitaxy using triethylgallium (TEG) and thermally cracked phosphine (PH_3) and arsine (AsH_3) as precursors. We have also grown samples using Au colloidal nanoparticles of 5 nm diameter commercially available from Ted Pella. The procedure consisted of diluting the solution with nanoparticles in deionized water at a 1: 4 concentration, depositing the solution on GaAs substrates (100) and drying with N_2 flow after 1 h.

5.3 Sn-catalyzed GaAs NWs

First, we investigate the effect of growth temperature on the formation of GaAs nanowires, as described in Table 5.1. All the samples discussed in this section were grown in GaAs(100) substrates. It has been reported on literature that the formation of uniform, oriented and good crystalline quality nanowires of Sn-catalyzed GaAs occurs only in a narrow temperature range, in MOVPE growths [75].

Sample	Material	TEG (sccm)	AsH₃ (sccm)	Time (min)	NP	Temperature (°C)
F1	GaAs	2.2	5.0	60	Sn	470
F2	GaAs	2.2	5.0	60	Sn	490
F3	GaAs	2.2	5.0	60	Sn	510
F4	GaAs	2.2	5.0	60	Sn	530
F5	GaAs	2.2	5.0	60	Sn	550

Table 5.1 – Growth conditions for the growth of GaAs on GaAs(100) using Sn nanoparticles.

Here, we have investigated nanowire growth dynamics in the range of 370 °C – 550 °C using our CBE system, as mentioned in table 5.1. At critical temperature, we observed that the nanowire morphology drastically changes from irregularly-shaped, at temperatures 470 °C and 490 °C, to nanowires with smooth sidewalls, as can be seen in Figure 5.2. In addition, within the range 510 °C – 530 °C, an enhancement in the VLS growth rate leads to high aspect ratio nanostructures (Figure 5.2C). At even higher temperatures, we have observed the same regular morphology, but a drastic reduction in the axial nanowire growth rate. The morphology obtained at low temperatures suggests that growth is unstable in this range; the catalyst particle most likely is not static at the NW apex during growth, what can lead to significant morphology

changes along the nanowires [183]. Therefore, the growth temperature for well-defined Sn-catalyzed GaAs nanowires is very narrow (510 °C – 530 °C).
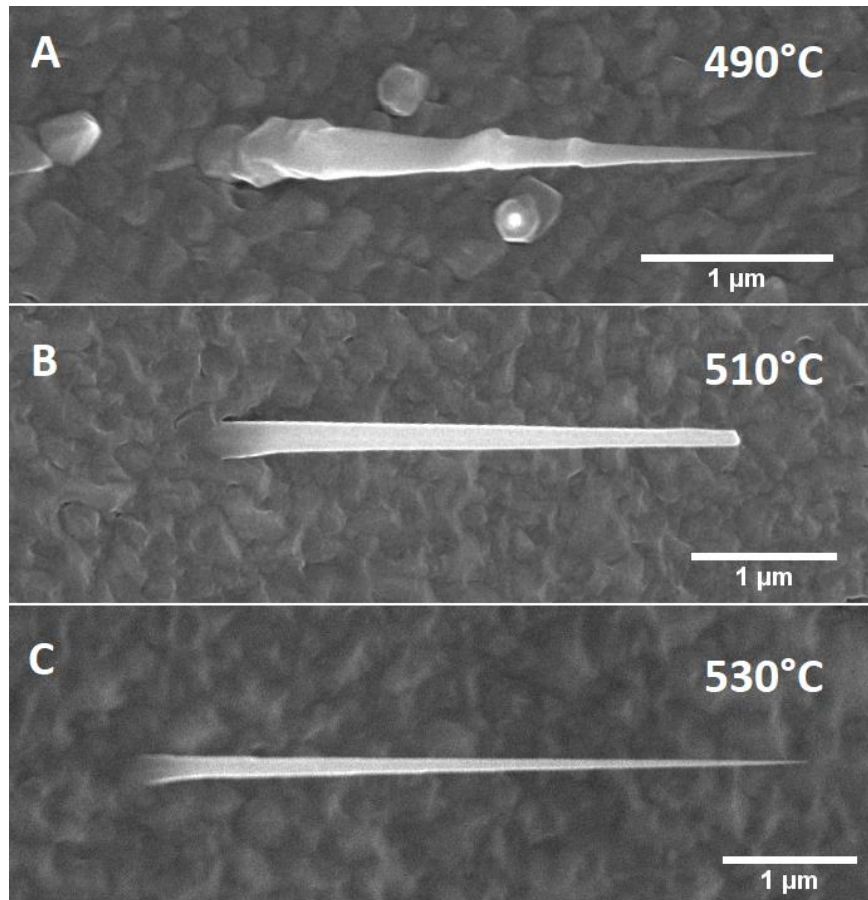
Figure 5.2 – (A-C) Top-view SEM images of Sn-catalyzed GaAs nanowires, grown in different growth temperatures, in the range 490 °C – 530 °C, respectively.

Nanoparticle size has a large influence on growth dynamics; completely different nanostructures are obtained by simply changing the size of the catalyst nanoparticle in the case of gold.[60, 65] Thus, it is important to confirm the nanoparticle diameter after growth. Furthermore, determining the chemical composition can show if the nanoparticle is composed of Sn, if contamination of another metal is present [178], or even if a Ga droplet, which could also self-catalyze nanowire growth, must be considered as well. The latter case could be possible because we are using high temperatures above the congruent evaporation temperature of GaAs; in this case As should evaporate from the substrate, since we have heated it up without group V overpressure [24].

Thus, we analyzed the apex of the nanowires, their chemical composition and crystallinity via transmission electron microscopy. We can see from Figures 5.3 and 5.4 that nanowires grown at 510 °C and 530 °C, respectively, have zinc blend (ZB) crystal structure,

but with a high density of extended defects as stacking faults and Wurtzite segment inserts. Defect density is high for the two well-ordered morphologies grown at 510 °C and 530 °C. Moreover, these nanowires grow in a direction that is approximately 36 ° with the substrate surface (100), Figure 5.2, indicating that they are <111>-oriented, which was also confirmed from TEM analysis, Fig. 5.3 and 5.4.
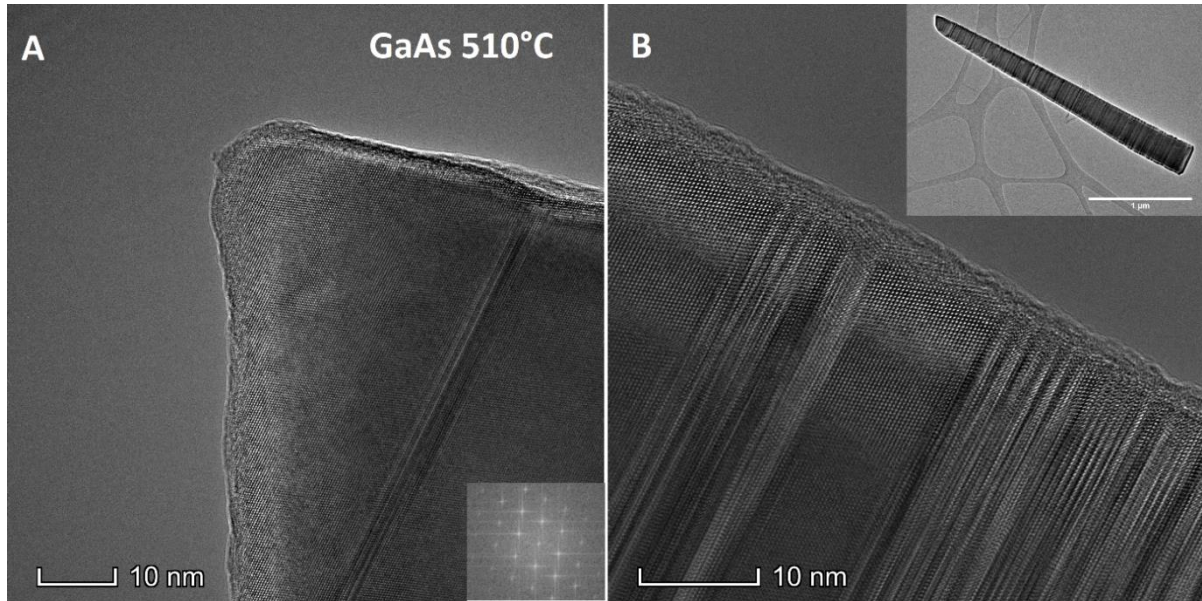
Figure 5.3 – (A e B) HRTEM images of Sn-catalyzed GaAs NWs grown at 510 °C. Inset: in (A) FFT of the HRTEM image shown in (A), and in (B) low magnification TEM image of the same NW shown in (A) and (B).
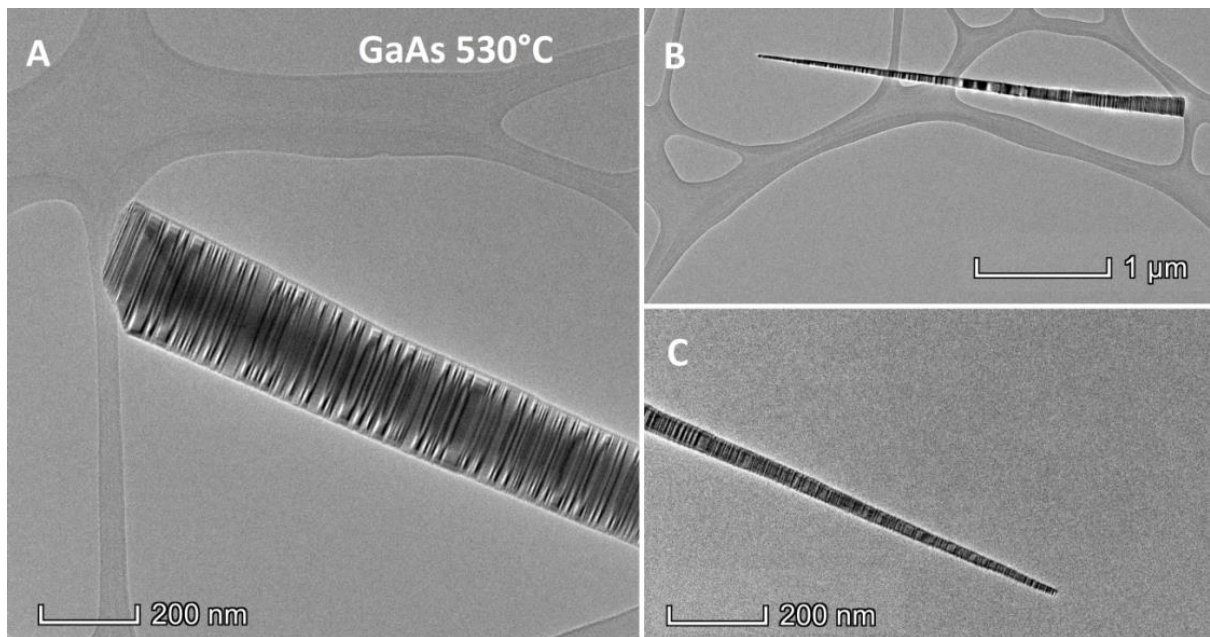
Figure 5.4 – (A - C) HRTEM images of Sn-catalyzed GaAs NWs grown at 530 °C.

However, we were unable to identify the catalyst at the tip of both samples. This analysis is difficult because, when the nanowires are transferred from the growth substrate to the carbon grid, required for TEM analysis, some nanowires break, especially the tip, which is extremely thin (d ≤ 10 nm), as we can see in Fig. 5.3A. Thus, we could not determine whether the nanowires actually grew without a catalyst or the NP was just removed from the structure during sample preparation for TEM analysis. In any case, if the structure shown in Figure 5.3 is catalyzed by a nanoparticle, it should have at least a diameter of 10 nm, i.e., small nanoparticles produce the nanowires.

5.4 Sn-catalyzed GaP NWs and Ni composition in Sn nanoparticles

We have also investigated the effect of temperature on the growth dynamics of GaP nanowires, as described in Table 5.2. In this case, we have deposited the Sn nanoparticles on GaAs(100) substrates. We can see in Fig. 5.5 that the formation of GaP nanowires occurs in these conditions. An increase in axial growth rate and smoothing of the morphology (for all populations present in the sample) are observed with an increase in temperature; therefore, a more favorable thermodynamic condition for the formation of the nanowires is most likely reached at higher temperatures, Figure 5.5.

Sample	Material	TEG (sccm)	PH₃ (sccm)	Time (min)	NP	Temperature (°C)
G1	GaP	2.4	15.0	60	Sn	510
G2	GaP	2.4	15.0	60	Sn	530

Table 5.2 – Growth conditions for the growth of GaP on GaAs(100) using Sn nanoparticles.

A crucial difference between GaP and GaAs nanowire growth is the presence of different populations in the sample, as can be seen in Figure 5.6, for the growth at 510 °C. In this case, the sample is dominated by two longer (~ 1.5 µm) nanowire ensembles, such as an irregular morphology, oriented to the substrate and differing by the curvature of their structure, Figure 5.6A and B. In addition, we have observed many rather short structures, with a completely atypical morphology for a nanowire, Figure 5.6C. Other types of nanowire are present in the sample, but in much smaller frequency. Among the long nanowires in this sample, the longest straight nanowire population without apparent curvature is dominant, Figure 5.6D. Similar behavior was observed for the growth performed at 530 °C.

The first step in controlling the synthesis of GaP nanowires includes a chemical analysis of the catalyst, to confirm that Sn indeed provides VLS growth of the nanowires and,

if so, which nanoparticle sizes favor their formation, since the size distribution of Sn NP's is relatively wide (Fig. 5.1)
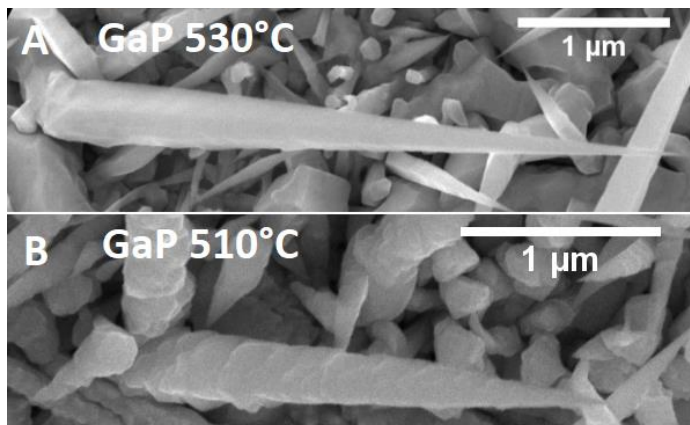
Figure 5.5 – (A) and (B) Top-view SEM images of the population of straight GaP NWs grown at different temperatures.
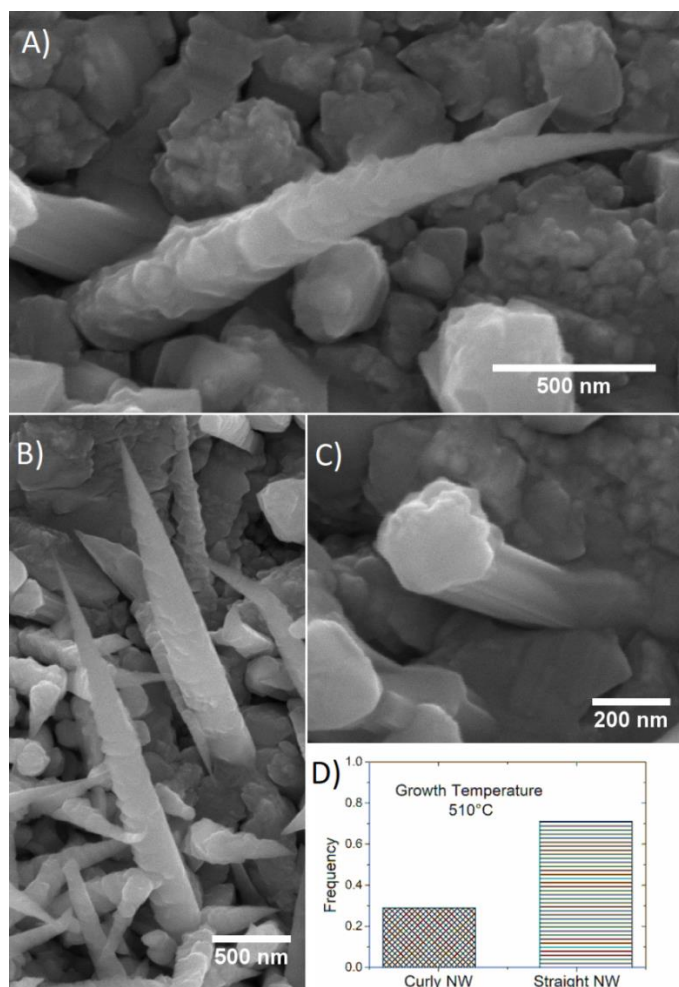
Figure 5.6 – (A - C) Top-view SEM images of GaP NWs grown at 510 °C. (D) Statistical analysis of the different populations that appears in the sample.

Transmission electron microscopy characterization of GaP nanowires grown at 510 °C has revealed that the two elongated populations, curved and straight nanowires, are catalyzed only by very small particles with diameters smaller than 10 nm, as can be seen from Figure 5.7 for the curly NWs. Furthermore, surprisingly, we found no tin in the catalyst nanoparticle; instead, Ni was shown as the main element in the composition (Fig. 5.7A,B).
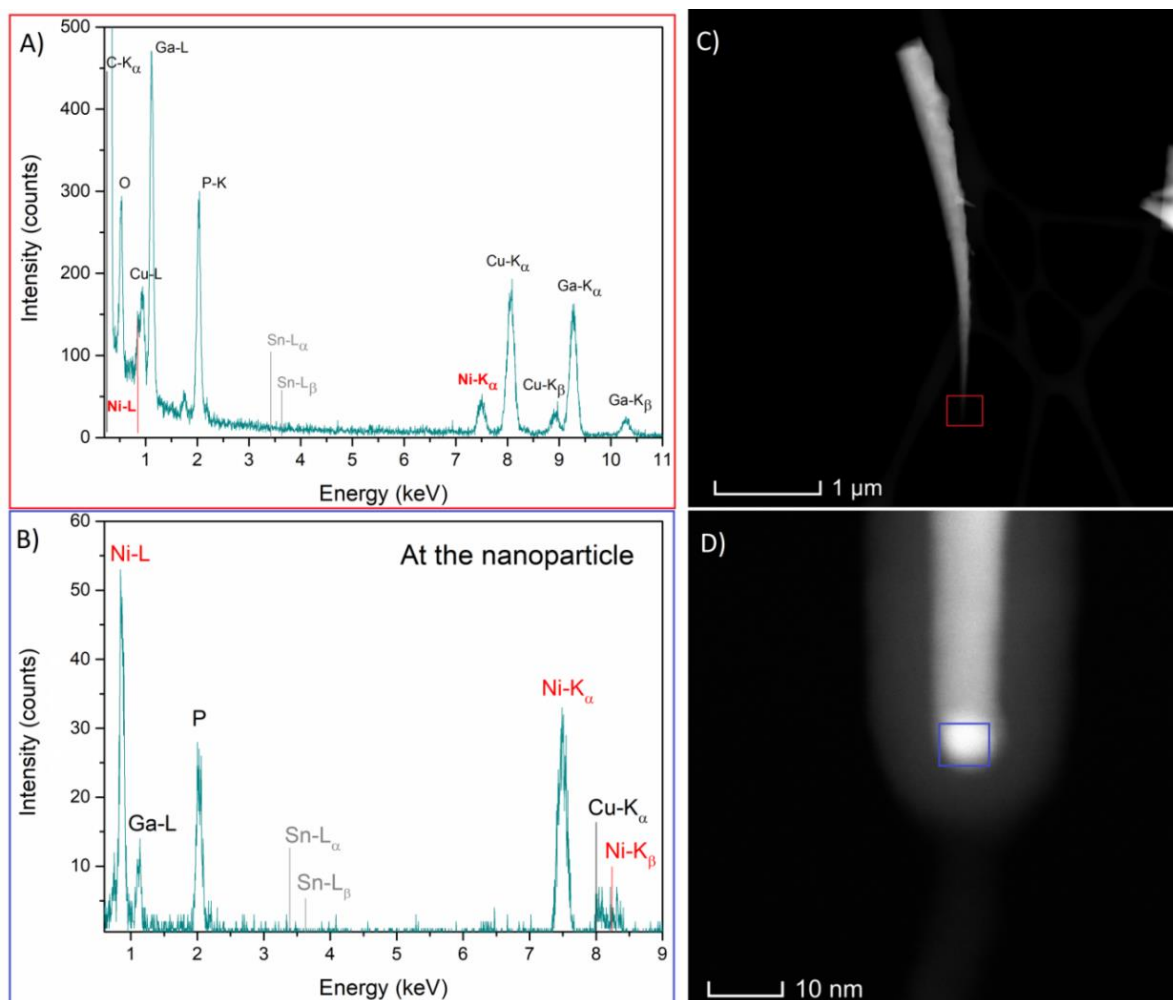
Figure 5.7 – (A) and (B) EDS spectrum acquired at the tip and the nanoparticle, respectively. (C) and (D) HAADF images of curly GaP NWs. The X-rays peaks related to Nickel are highlighted in red.

The EDS spectrum shown in Fig. 5.7A was acquired at the tip of the nanowire; it is clear the absence of Sn peaks and the presence of Ni-K$_\alpha$ peak at 7.48 keV. Fig. 5.8A also shows that the Ni-K$_\alpha$ intensity is greater than the standard deviation of the background ($3\sqrt{N}$; N is the counts of the background) which means this peak is statistically significant, i.e., a real observation. When the EDS measurement is acquired only in the nanoparticle, Fig. 5.7B, we can notice the reduction of the Cu signal from the sample holder and the clear presence of Ni-L signal (we cannot resolve the L peaks from these data, since the emissions are very close, Ni-

L_α at 0.849 keV and Ni-L_β at 0.866 keV). All these features were also observed for the straight GaP nanowires that were present in the same sample grown at 510 °C.

Therefore, the presence of statistically significant Ni peaks from both L-series and K-series indicates that the nanoparticle catalyst is composed by Nickel, rather than Sn. These results lead us to the question: where would the measured Ni come from? No Ni was detected on the nanoparticles measured before growth (Figure 5.8A,B), and we do not have any source of Ni in the growth system that could lead to this contamination.
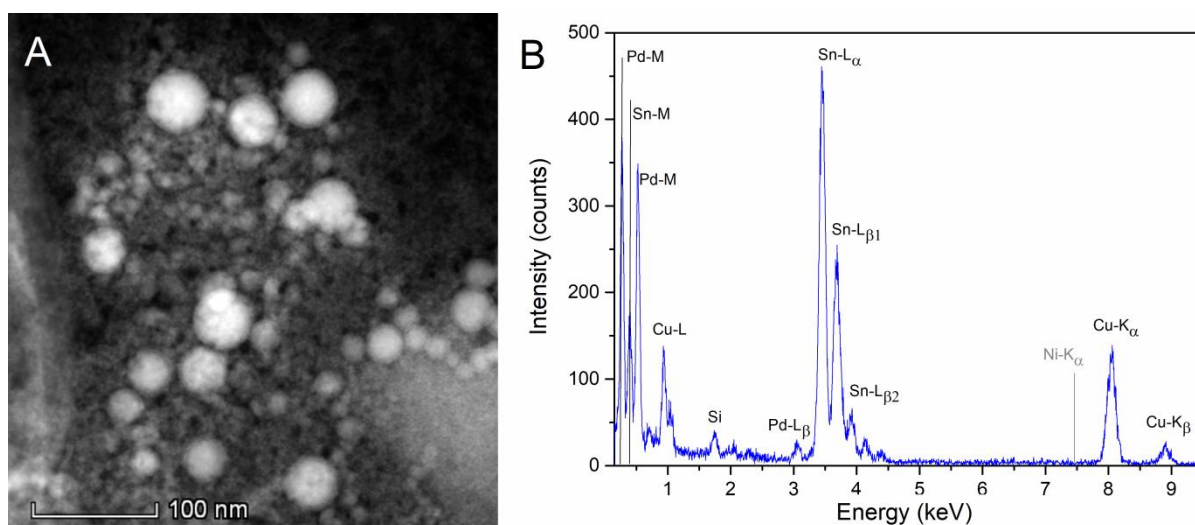
Figure 5.8 – (A) HAADF image of Sn Nanoparticles. (B) EDS spectrum acquired at an individual small nanoparticle (d $\simeq$ 15 nm).

We have also measured a large portion of nanoparticles performing the EDS measurement in the TEM mode, in order to increase the number of counts, i.e., be able to identify a small quantity of Ni. However, this procedure has produced the enhancement of the Cu peaks (that comes from the sample holder), which are very close of the Ni ones, and we were not able to identify any small Ni present, in this case. In Fig. 5.8B we can also see the presence of other elements in the particle as, for example, palladium (Pd), showing that there is an absence of purity in the nanoparticles.

The fact that we have never observed any Ni contamination from the samples grown using Au supports the argument that it comes from the NP, rather than the growth system. Another interesting point is that the nanoparticles that in fact catalyze the growth are very small (d $\leq$ 10 nm); hence, there was not much Ni available. In addition, Tin (Sn) and Nickel (Ni) easily form an alloy [184], and we speculate that the Ni present in the Sn nanoparticle was in atomic concentration, and because of that, we were not able to measure the Ni signal from EDS

directly on the nanoparticles before growth. However, during growth at high temperatures (T > 500 °C), Ni atoms could diffuse and aggregate, forming very small nanoparticles able to catalyze GaP nanowire growth.
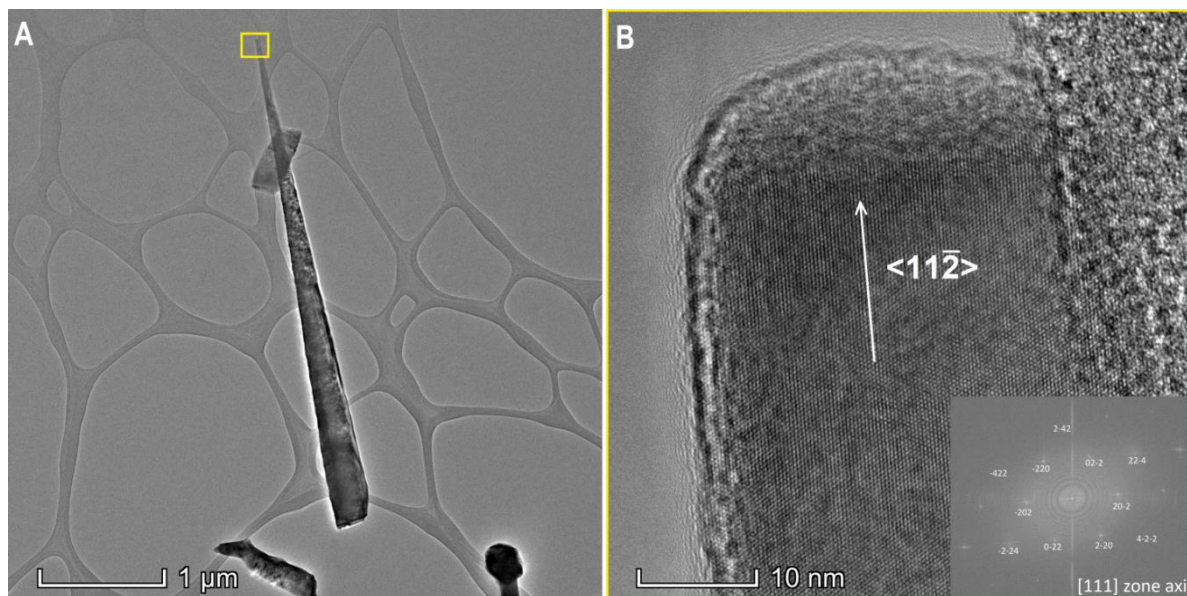
Figure 5.9 – (A) Low magnification of Ni-catalyzed straight GaP NWs. (B) HRTEM image of the same NW shown in (A). Inset: Fast Fourier Transform (FFT) of the image shown in (B).

Structural characterization of the straight GaP nanowires grown at 510 °C revealed that they are ZB phase nanowires, as can be seen for the straight nanowire population grown at 510 °C, Figure 5.9A,B. It should be noted that in Figure 5.9B the tip seems to be broken, but several images in STEM mode were made of both straight and curved nanowires. The presence of the catalyst was indeed observed, always at a size smaller than 10 nm and followed by a very thin long segment, as shown in Figure 5.7D.

We can also see from Figure 5.9B (FFT of the image inset) that straight nanowires exhibit a <11-2> growth direction, a result that has already been observed for group IV nanowires and ternary alloys III-V [120, 185]. In addition, they have extended lamellar defects, i.e., along the growth direction, Fig. 5.10A,B.
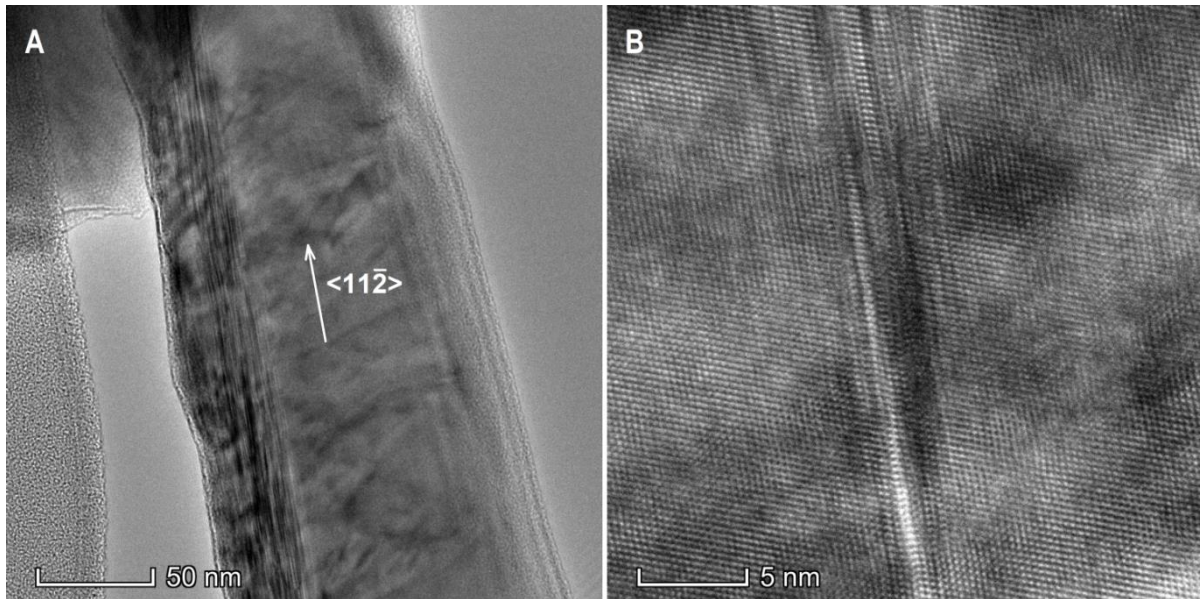
Figure 5.10 – (A) Low magnification of Ni-catalyzed straight GaP NWs. (B) HRTEM image of the same NW showed in (A).

It is interesting to mention that nanoparticle observation was possible for GaP nanowires, but not for GaAs, most likely due to the difference in nanowire density in both samples, as can be seen in Figure 5.11. While the observed GaAs nanowire density was very low in as-grown substrate (Figure 5.11B), formation of nanowires is favored in a noticeably larger amount for GaP, Figure 5.11A. Thus, in the latter case the amount of nanowires available in the grid for analysis was much larger, which allowed the eventual observation of the intact structure of the nanowire with the catalyst on the apex.
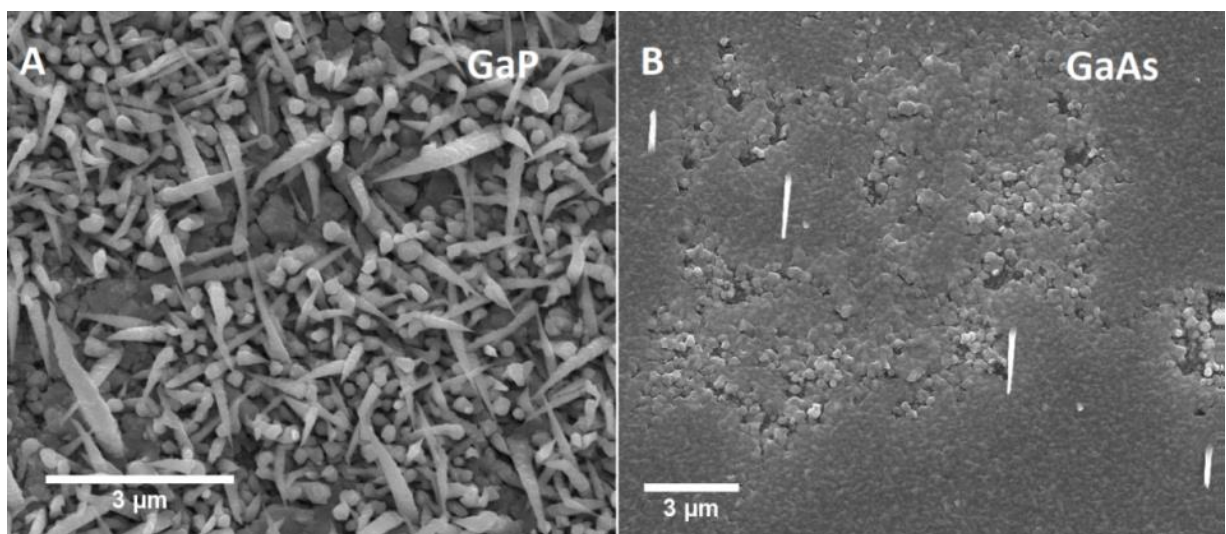
Figure 5.11 – (A e B) *Top-view* SEM images of GaP and GaAs nanowires grown on GaAs(100) at 510 °C e using the Sn nanoparticles produced by laser ablation in water solution.

5.5 Analyzing the growth dinamics of Ni-catalyzed GaP NWs

In order to solve the question of the Ni contamination, we decided to grow GaP nanowires using Ni nanoparticles prepared by another route; in this case, by thermally dewetting a Ni thin film. If we obtain similar nanowires in the same growth condition, our interpretation about Ni contamination in the Sn nanoparticles produced by laser ablation would be further confirmed.

Therefore, we have deposited from thermal evaporation 5 Å Ni thin film on GaAs(100) and Si(100). The nanoparticles were produced by in-situ annealing, before nanowire growth, at 600 °C under PH_3 overpressure (12.5 sccm PH_3 flow) for 10 min. After that, the temperature was lowered to the growth temperature under the same PH_3 flow and the growth was performed, as described in Table 5.3.

Sample	Material	TEG (sccm)	PH_3 (sccm)	Time (min)	NP	Temperature (°C)
H1	GaP	2.4	15.0	60	Ni	470
H2	GaP	2.4	15.0	60	Ni	500
H3	GaP	2.4	15.0	60	Ni	530
H4	GaP	2.4	15.0	60	Ni	560
H5	GaP	2.4	15.0	60	Ni	590

Table 5.3 – Growth conditions for the growth of GaP on GaAs(100) and Si(100) using Ni nanoparticles.

We have observed the growth of the GaP nanowires using Ni nanoparticles both on GaAs(100) and Si(100). Interestingly, the yield was much higher for the growth on Si than on GaAs; nevertheless, the same type of structures was observed, straight and curly nanowires (Fig. 5.12c). We can see in Fig. 5.12 the evolution of GaP nanowires with growth temperature. Curly and straight nanowires were obtained, similarly as those grown using the laser ablation Sn nanoparticles described in section 5.4, Fig. 5.12B,C. This result confirms that in fact Ni catalyzes the growth of these nanowires.

Furthermore, we could obtain Ni-catalyzed GaP nanowires in a wide growth temperature range and in a temperature window which is larger than that used for Au-catalyzed counterparts (usually T < 550 °C in our CBE reactor). As we can see in Fig. 5.12 the VLS mechanism in this case most likely occurs above 500 °C, where we have well defined nanowires.
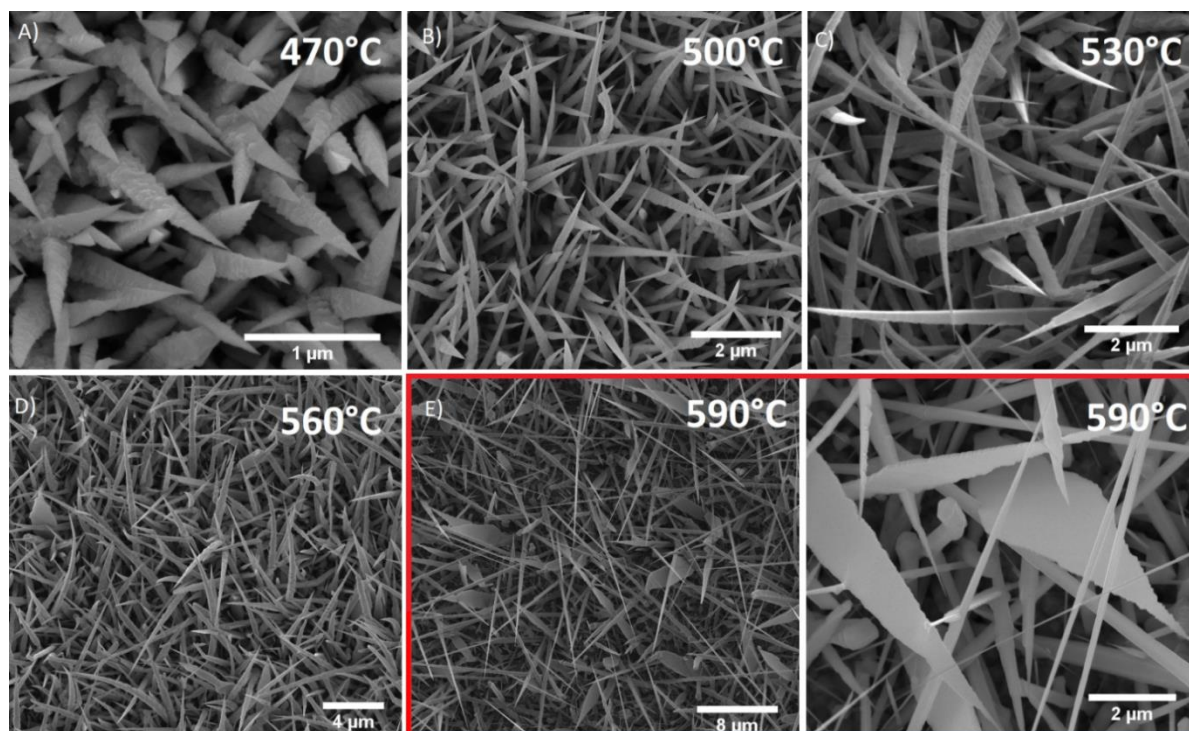
Figure 5.12 – (A - E) Top-view SEM images of Ni-catalyzed GaP nanowires grown on Si(100) at different temperatures in the range 470 – 590°C.

An increase in the axial growth rate and high aspect ratio nanowires grown at 590 °C, leads to nanowires larger than 30 μm, Fig.5.12E and Fig. 5.13A. As we have discussed in chapter 3, Au-catalyzed GaP nanowires usually have growth rates of 0.5 nm/s. Here, at 590 °C and providing the same precursors flow we can reach high growth rates ~ 8 nm/s. Moreover, at 590 °C the presence of a different morphology, that resembles a nanosheet was obtained, Fig. 5.13B.
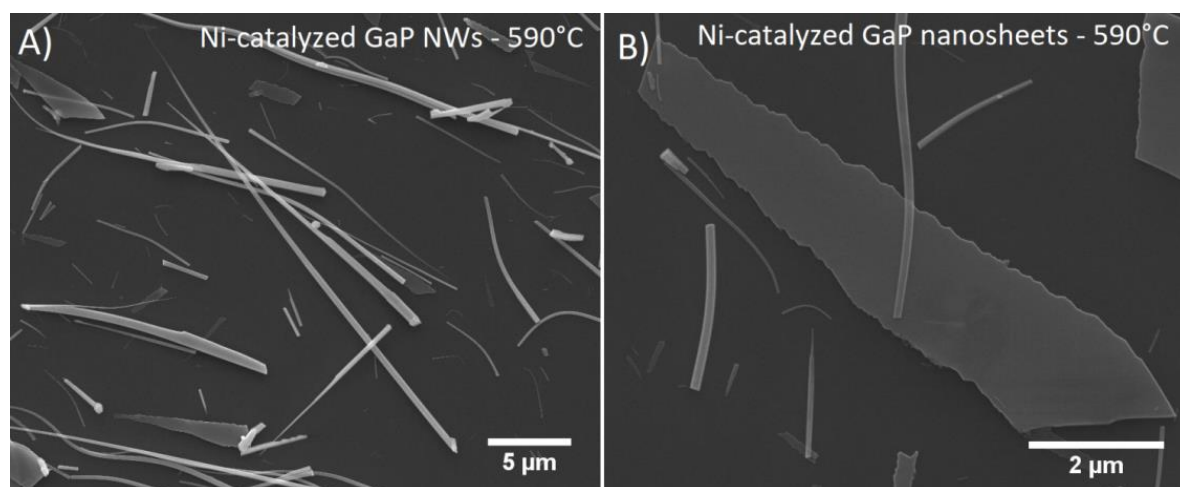
Figure 5.13 – (A) and (B) Top-view SEM images of Ni-catalyzed GaP NWs grown at 590 °C and transferred to Si substrate.

When we analyze the chemical composition of the post-growth Ni nanoparticles for both curly and straight nanowires, we observe that the nanoparticle is rich in phosphorous (P) rather than gallium (Ga), as can be seen in Fig. 5.14A-D. We have observed this effect in several curly and straight nanowires. This indicates that the growth dynamics, in this case, is most likely controlled by group V species, i.e., a distinct behavior compared to Au as catalyst.
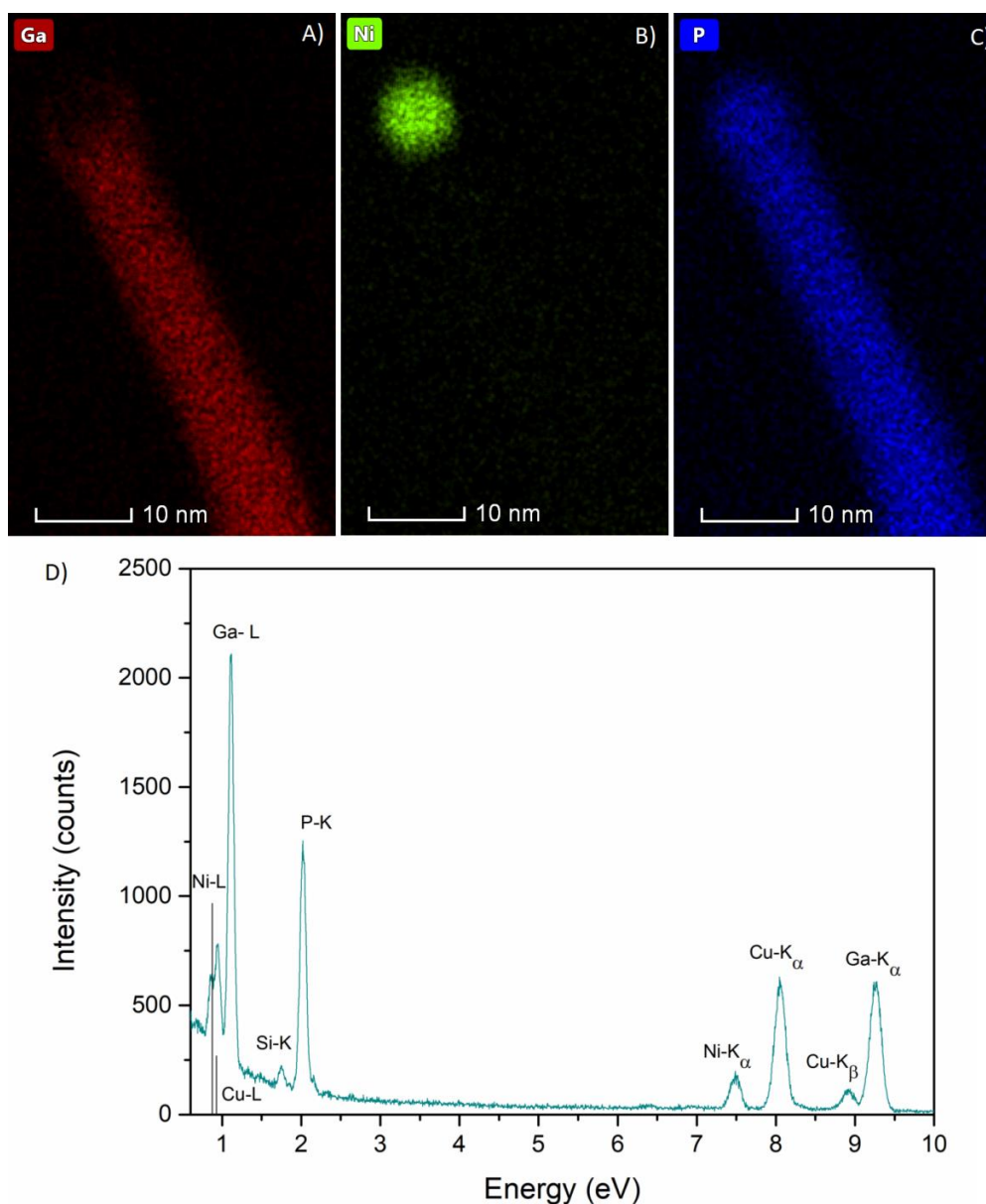
Figure 5.14 – (A - C) EDS images showing the different element present in the NP, Gallium (Ga), Nickel (Ni) and phosphorus (P). (D) EDS spectrum of the measurement done in the images (A-C).

5.6 Optical characterization of Ni catalyzed GaP NWs

PL measurements at low temperature were performed to optically characterize the Ni-catalyzed GaP nanowires. We can see in Fig. 5.15 a drastic change in the emissions bands, as compared to the spectrum of Au-catalyzed nanowires shown in chapter 4. The inset of Fig. 5.15 shows photographs of the samples grown at different temperatures. It is clear that, by increasing growth temperature, a color change appears in the sample and a more yellowish sample is produced for growth at 590 °C. This behavior is accompanied by the emergence of new relatively narrow emissions bands (linewidth ~ 25 meV and 30 meV) at 2.16 eV and 2.20 eV, respectively, Fig. 5.15.
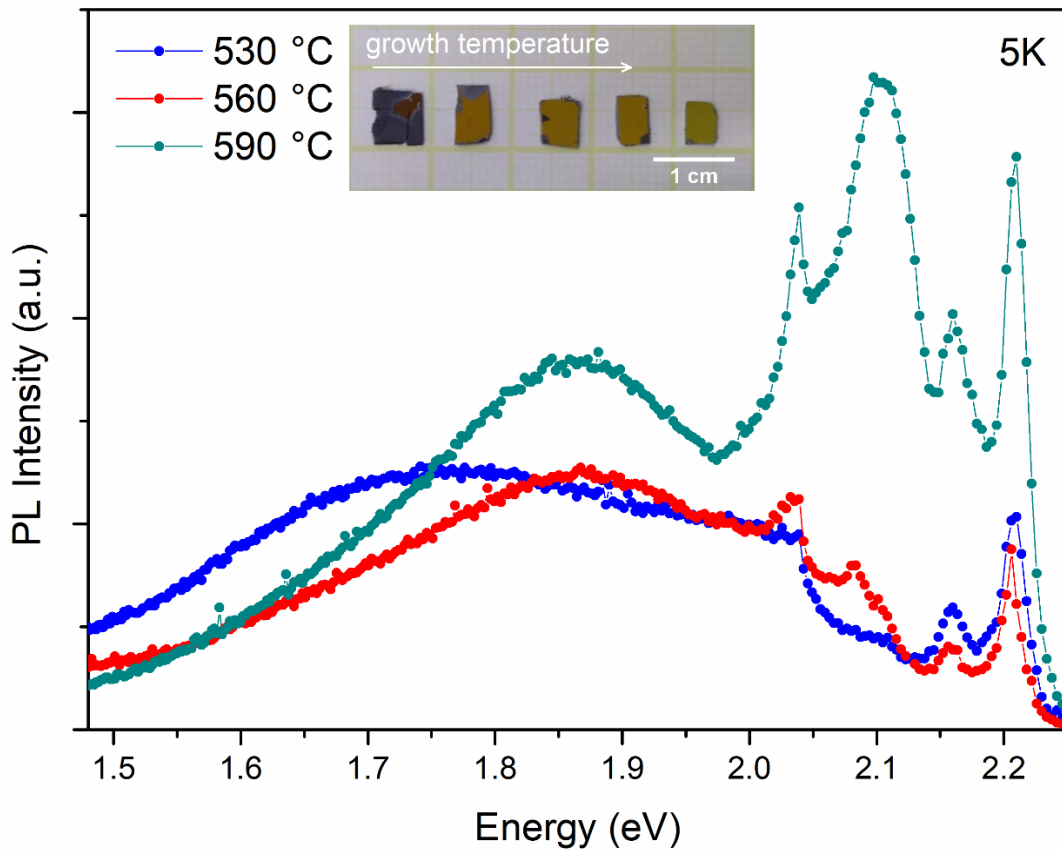
Figure 5.15 – PL spectra acquired at 5 K of Ni-catalyzed GaP nanowires acquired at low excitation density (8.0 W/cm^2). Inset: photographic images of the as-grown samples for different temperatures.

In addition, an enhancement of the peaks at 2.04 eV and 2.09 eV, discussed in chapter 4, are also observed. The linewidth of the new emissions and the intensity enhancement of the peaks also observed for Au-catalyzed nanowires suggest that they are all impurity-related. This enhancement is associated with an increase in the incorporation of residual impurities, most likely due to the higher temperature employed for the Ni-catalyzed NWs.

5.7 Differences between Au and the new catalysts, Sn and Ni, for the growth of III-V NWs

5.7.1 Au catalyzed III-V NWs in our CBE system

We have also grown Au-catalyzed nanowires of several III-V materials in order to better understand the similarities and differences between the new catalysts and the largely used gold. We have grown GaAs, GaP and InAs nanowires in different growth conditions; we display some of them in Table 5.4. We have used colloidal 5 nm Au nanoparticles deposited on GaAs (100) substrates for all growths. The samples were cooled down under PH_3 or AsH_3 overpressure, using the same flow used during growth.

Sample	Material	TEG (sccm)	TMIn (sccm)	AsH₃ (sccm)	PH₃ (sccm)	Time (min)	Temperature (°C)
I1	GaP	2.4	-	-	15.0	60	530
I2	GaAs	2.2	-	5.0	-	60	480
I3	InAs	-	0.6	15.0	-	60	450

Table 5.4 – Growth conditions for the growth of different III-V semiconductors on GaAs(100) using 5 nm Au nanoparticles.

Essentially, as general characteristics observed here, as we can see in Fig. 5.16a-c, and already reported in literature, we can highlight three main aspects of the Au-catalyzed nanowires grown in our CBE system.

First, the preferential growth direction lies on the family of crystallographic directions <111> [80]. The formation energy between ZB and WZ phase in III-V materials in this direction is very similar, resulting in a high density of extended defects as stacking faults, twins and insertions of one phase into another during growth [80]. Thus, only in very specific conditions nanostructures with high crystal quality can be obtained. In order to grow pure phase nanowires, this growth direction should be avoided, if possible [101, 108].

Secondly, in our CBE reactor we have a high axial (VLS) growth rate for the nanowires based in In, compared to Ga-based materials, which reflects the higher solubility of In in Au [126]. This effect results in Ga-based nanowires with low aspect ratio, i.e., nanostructures with a conical morphology compared to In-based, as we can see in Fig. 5.16a-c for the Au-catalyzed GaP, GaAs and InAs NWs grown in our CBE system, respectively.
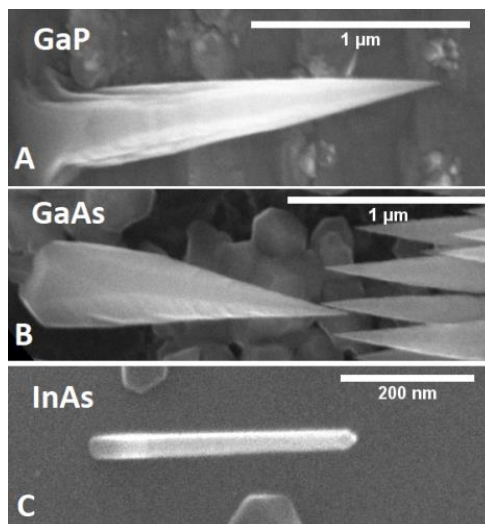
Figura 5.16 – (A-C) *Top-view* SEM images of Au-catalyzed GaP, GaAs and InAs nanowires, grown in different conditions in our CBE system.

Lastly, the growth of well-oriented nanowires and in a regular morphology occurs in a wide range of growth temperatures studied (390 °C – 550 °C) for the different III-V materials, highlighting another advantage of gold as catalyst: the facility to promote the anisotropic growth of III-V semiconductors at nanoscale under conditions available in traditionally used systems for synthesis of semiconductor thin films, such as MOVPE (Metallorganic Vapor Phase Epitaxy), MBE (Molecular Beam Epitaxy) and CBE (Chemical Beam Epitaxy).

5.7.2 Discussion

The use of new catalysts rather than gold is an interesting topic and has been explored recently for III-V semiconductor nanowires. In particular, Ni catalyzed GaP NWs are very poorly explored in literature and just few works recently describe Sn-catalyzed GaAs NWs [180, 75]. Thus, it is noteworthy that our results show that Ni can effectively be used as catalyst for GaP nanowires, producing high aspect ratio nanostructures oriented in unusual <11-2> direction and employing a higher temperature range compared to Au, but still within the working temperature of many vapor-phase epitaxy systems used for this goal.

Furthermore, we have shown that nanowire growth only occurs for very small Ni nanoparticles (d $\leq$ 10 nm), with high growth rate (~ 8 nm/s) for Ga-based nanowires, mainly for GaP grown on Si(100). This behavior could be explored to overcome the limitations of the use of gold in our system. The control/removal of the Vapor-Solid (VS) growth mode in nanowire sidewalls is usually done through in situ etching with HCl, for nanowires grown by

MOVPE [56, 31]. However, the use of HCl is unsuitable for CBE, since it could affect the weldings of the ultra-high vacuum chamber. Thus, the control of the VS growth in our system is limited for Au-catalyzed Ga-based nanowires. Therefore, by changing the catalyst metal, employing Ni, we can grow high aspect ratio nanowires. This is important, for example, for the growth of axial heterostrutures and axial p-n junctions, for which the VS growth should be avoided.

Another interesting point to note is that the post-growth Ni catalyst nanoparticle is rich in group V (phosphorus), a behavior that is completely different from Au catalyzed nanowires [22]. In the case of gold, it is extensively reported in the literature that NP reacts more easily with group III, which ultimately determines many aspects of growth dynamics such as supersaturation during growth [186]. This parameter is important because it can have a direct influence on the crystal structure to be adopted by the structure [130, 186]. Thus, our results suggest that, in the case of Ni, phosphine flow may play a much more important role than the Ga precursor and, consequently, in supersaturation.

Finally, we should mention that, by changing the catalyst metal, we were able to show that other crystallographic directions rather than <111> can be obtained. The growth direction control is an interesting topic, due to the possible supression of extended defects [187]. Moreover, the growth of <112> nanowires can present instabilities due to the different growth rates of the front-facets (111)A and (111)B [120], allowing the nanoparticle to move to the sidewall during the cool down process. Therefore, subsequent growth of the nanowire can occur in a distinct direction as compared to the first stem. However, until now the growth of the <11-2>-oriented III-V nanowires has not been fully controlled [120]. Here, we show a controllable way to favor the <11-2> growth direction; however, we observed no NP instablities, most probably due to the facts that only very small Ni nanoparticles catalyze the growth, and to the chemical and surface energy differences between gold and nickel.

5.8 Conclusions

In order to achieve the monolithic integration of III-V compounds on Si as well as obtain new properties and fine control over the semiconductor nanowire properties, the search for distinct metal catalysts has been pursued in the last years. Tin (Sn) and Nickel (Ni) have been barely explored for the growth of III-V materials, particularly Gallium Phosphide (GaP).

Here, we have reported the growth of high aspect ratio Ga-based nanowires. GaAs nanowires were grown on GaAs(100) substrates; they present a high density of stacking faults

and a phase mixture between ZB and WZ with the usual <111> growth direction. We have also observed that uniform and well defined morphologies occur just for a narrow growth temperature window. However, we were not able to confirm the presence of Sn as the catalyst, which seems to be consumed in the growth. Since only very small nanoparticles have promoted the growth here and Sn acts as dopant in III-V semiconductors, we speculate that the Sn nanoparticles were consumed during the cool down step, when the supersaturation inside the nanoparticles changes.

In the case of GaP nanowires, we have shown that using Ni as catalyst, high aspect ratio <11-2>-oriented nanowires can be grown on Si(100) in a temperature range that is higher than that usually employed for the gold counterparts. Moreover, the higher temperature growth allowed a change in the unintentional impurities incorporation during growth, leading to a narrow green luminescence at 2.16 eV and 2.20 eV. However, further optical studies would be needed in order to reveal the physical origin of these emissions.

In addition, the VLS growth of III-V nanowires performed with gold has demonstrated that the Au droplet is rich in the group III species, rather than the group V. This means that, for example, the supersaturation is mainly controlled by the III-element flow during growth. Here, we have found that the post-growth Ni nanoparticle is rich in phosphorous (group V), suggesting that supersaturation and, consequently, the crystal structure in this case, might be controlled by hydride flow. Finally, we also provide a discussion about the differences and the possibilities of changing the catalyst for the growth of III-V nanowires in our CBE system. All the observations here provide the first attempt in order to realize Ni as an alternative catalyst for GaP NW growth.

Chapter 6

Conclusions and Outlook

Nanowires are interesting platforms for developing new physics and material science studies; intense research on nanowire growth and basic optical and electrical properties has been carried out in the last 20 years. They are promising building blocks for boosting the efficiency of optoeletronic devices, but the development of new growth routes as well as in depth optical studies are still required for some materials, such as WZ Gallium Phosphide, in order to confirm or not their potential for device fabrication. Therefore, this work focused mainly in studying Gallium Phosphide NWs with hexagonal crystal structure, with a small contribution also on the growth of WZ GaAs nanowires. Here we provide a study combining growth and optical investigations, which open up the possibility to better understand and control the final nanostructure properties. We have first adressed different growth investigations, and then naturally extended the investigation to the optical properties of the materials, and finally combined them.

On the basic research point of view, our work answers important questions concerning the eletronic properties of WZ GaP, as the nature and value of the band gap. In chapter 4 we have provided direct evidence of the pseudo-direct band gap behaviour, as previously calculated by DFT. This basic information is important to develop optoeletronic devices; in this case, unfortunately, WZ GaP is not the best choice, since the pseudo-direct band gap should not have high radiative band-to-band recombinations, despite some contrary reports [55]. On the other hand, our work has also shown that large area WZ GaP (tending to a micro-sized volume) with good crystal quality can be achieved using the crawling assisted procedure, demonstrated in our study of WZ GaP NW growth and discussed in Chapter 3 [65]. These nanowires have been used as virtual substrates for the growth of hexagonal Si and SiGe alloys in a core-shell structure [39, 136]. These group IV materials, particularly SiGe, have indeed shown direct band gaps, which could be a revolution for on-chip photonics. In this sense, the Ni-catalyzed GaP nanostructures with nanosheet shapes presented in chapter 5 are interesting, because they could be a feasible 2D WZ GaP, which might show that the WZ phase can be grown without the restriction of nanowire morphology.

Concerning the optical properties and the understanding of the nature of WZ GaP optical emissions, we have shown here a unique combination of growth and optical studies.

Few works have studied in detail the optical properties of the Au-catalyzed WZ GaP NWs and none of them have suggested the possible impurities involved and how they have been incorporated. The work presented here brings some light to the optimizaton and understanding of the luminescence of this new material. Interestingly, we show that growth under low group III precursor flow resulted in enhanced emission above 2.0 eV, as compared to broad band emissions at lower energies. In principle, by lowering group III precursor the emission of deep levels below 2.0 e V could be suppressed or minimized. Moreover, new emissions in the visible range were observed for Ni-catalyzed GaP NWs/nanosheets. However, a detailed study about the physical mechanism behind these emissions is necessary in order to understand if they are due to impurities or band-to-band recombinations.

Finally, new strategies for bottom-up growth of semiconductor nanowires are interesting as they open up the possibility to access new phenomena. As an example, we have shown in this work that undesired phenomenon as Au droplet crawling on III-V surfaces can be used to alter nanowire growth dynamics and provide an asymmetric GaP morphology, which preserves the WZ phase. Semiconductor nanomaterials with alternative morphologies are interesting for anti-reflection coating, for example. In addition, we have shown that Ni can easily catalyze GaP nanowires with high aspect ratio, specially on Si substrates, which is very interesting for develop integration of III-V semiconductor on Si technology. Further studies are necessary in order to understand the role of the Si substrate in the growth mecahnism. We believe that Si forms an alloy with the Ni nanoparticles, which more easily triggers the VLS mechanism rather than in III-V substrates.

References

1. Parker, M. *Physics of Optoelectronics*. (CRC Press Taylor & Francis Group, 2005).

2. Simmons, J. H. & Potter, K. S. *Optical Materials*. *Journal of Chemical Information and Modeling* vol. 53 (Academic Press - Elsevier, 2000).

3. Yu, P. Y. & Cardona, M. *Fundamentals of Semicondutors*. (Springer, 2010).

4. Grundmann, M. *The Physics of Semiconductors*. (Springer, 2006).

5. Algora, C., Ortiz, E., Rey-Stolle, I., Díaz, V., Peña, R., Andreev, V. M., Khvostikov, V. P. & Rumyantsev, V. D. A GaAs solar cell with an efficiency of 26.2% at 1000 suns and 25.0% at 2000 suns. *IEEE Trans. Electron Devices* **48**, 840–844 (2001).

6. Gessmann, T. & Schubert, E. F. High-efficiency AlGaInP light-emitting diodes for solid-state lighting applications. *J. Appl. Phys.* **95**, 2203–2216 (2004).

7. Nakamura, S., Mukai, T. & Senoh, M. Candela-class high-brightness InGaN/AlGaN double-heterostructure blue-light-emitting diodes. *Appl. Phys. Lett.* **64**, 1687 (1994).

8. Nakamura, S., Senoh, M., Iwasa, N., Nagahama, S., Yamada, T. & Mukai, T. Superbright Green InGaN Single-Quantum-Well- Structure Light-Emitting Diodes. *Jpn. J. Appl. Phys.* **34**, L1332–L1335 (1995).

9. Nakamura, S., Senoh, M., Iwasa, N. & Nagahama, S. I. High-power InGaN single-quantum-well-structure blue and violet light-emitting diodes. *Appl. Phys. Lett.* **67**, 1868 (1995).

10. Matthews, J. W. & Blakeslee, A. E. Defects in epitaxial multilayers: misfit dislocations. *J. Cryst. Growth* **27**, 118–125 (1974).

11. Auf Der Maur, M., Pecchia, A., Penazzi, G., Rodrigues, W. & Di Carlo, A. Efficiency Drop in Green InGaN/GaN Light Emitting Diodes: The Role of Random Alloy Fluctuations. *Phys. Rev. Lett.* **116**, 027401 (2016).

12. Zou, X., Wong, K. M., Zhu, X., Chong, W. C., Ma, J. & Lau, K. M. High-performance green and yellow LEDs grown on SiO2 nanorod patterned GaN/Si templates. *IEEE Electron Device Lett.* **34**, 903–905 (2013).

13. Choi, W., Choudhary, N., Han, G. H., Park, J., Akinwande, D. & Lee, Y. H. Recent development of two-dimensional transition metal dichalcogenides and their applications. *Mater. Today* **20**, 116–130 (2017).

14. Wang, R., Mujahid, M., Duan, Y., Wang, Z. K., Xue, J. & Yang, Y. A Review of Perovskites Solar Cell Stability. *Adv. Funct. Mater.* **29**, 1808843 (2019).

15. Lieber, C. M. & Morales, A. M. A laser ablation method for the synthesis of crystalline semiconductor nanowires. *Science (80-.).* **279**, 208–211 (1998).

16. Persson, A. I., Larsson, M. W., Stenström, S., Ohlsson, B. J., Samuelson, L. & Wallenberg, L. R. Solid-phase diffusion mechanism for GaAs nanowire growth. *Nat. Mater.* **3**, 677–681 (2004).

17. Bakkers, E. P. A. M., Van Dam, J. A., Franceschi, S. De, Kouwenhoven, L. P., Kaiser, M., Verheijen, M., Wondergem, H. & Van Der Sluis, P. Epitaxial Growth of InP Nanowires on Germanium. *Nat. Mater.* **3**, 769–773 (2004).

18. Larsson, M. W., Wagner, J. B., Wallin, M., Håkansson, P., Fröberg, L. E., Samuelson, L. & Wallenberg, L. R. Strain mapping in free-standing heterostructured wurtzite InAs/InP nanowires. *Nanotechnology* **18**, 015504 (2007).

19. Wallentin, J., Anttu, N., Asoli, D., Huffman, M., Åberg, I., Magnusson, M. H., Siefer, G., Fuss-Kailuweit, P., Dimroth, F., Witzigmann, B., Xu, H. Q., Samuelson, L., Deppert, K. & Borgström, M. T. InP nanowire array solar cells achieving 13.8% efficiency by exceeding the ray optics limit. *Science (80-.).* **339**, 1057–1060 (2013).

20. Standing, A., Assali, S., Gao, L., Verheijen, M. A., Van Dam, D., Cui, Y., Notten, P. H. L., Haverkort, J. E. M. & Bakkers, E. P. A. M. Efficient water reduction with gallium phosphide nanowires. *Nat. Commun.* **6**, 7824 (2015).

21. Jacobsson, D., Panciera, F., Tersoff, J., Reuter, M. C., Lehmann, S., Hofmann, S., Dick, K. A. & Ross, F. M. Interface dynamics and crystal phase switching in GaAs nanowires. *Nature* **531**, 317–322 (2016).

22. Maliakkal, C. B., Jacobsson, D., Tornberg, M., Persson, A. R., Johansson, J., Wallenberg, R. & Dick, K. A. In situ analysis of catalyst composition during gold catalyzed GaAs nanowire growth. *Nat. Commun.* **10**, 4577 (2019).

23. Roelkens, G. *et al.* III-V-on-silicon photonic devices for optical communication and sensing. *Photonics* **2**, 969–1004 (2015).

24. Ambrosini, S., Fanetti, M., Grillo, V., Franciosi, A. & Rubini, S. Vapor-liquid-solid and vapor-solid growth of self-catalyzed GaAs nanowires. *AIP Adv.* **1**, 042142 (2011).

25. Ellis, C. and R. S. W. The Vapor-Liquid-Solid Mechanism of Crystal Growth and Its Application to Silicon. *Trans. Metall. Soc. Aime* **233**, 13 (1965).

26. Borg, M., Schmid, H., Moselund, K. E., Cutaia, D. & Riel, H. Mechanisms of template-assisted selective epitaxy of InAs nanowires on Si. *J. Appl. Phys.* **117**, 144303 (2015).

27. Dick, K. A. A review of nanowire growth promoted by alloys and non-alloying elements with emphasis on Au-assisted III-V nanowires. *Prog. Cryst. Growth Charact. Mater.* **54**, 138–173 (2008).

28. Tomioka, K., Ikejiri, K., Tanaka, T., Motohisa, J., Hara, S., Hiruma, K. & Fukui, T. Selective-area growth of III-V nanowires and their applications. *J. Mater. Res.* **26**, 2127–2141 (2011).

29. Yazawa, M., Koguchi, M., Muto, A., Ozawa, M. & Hiruma, K. Effect of one monolayer of surface gold atoms on the epitaxial growth of InAs nanowhiskers. *Appl. Phys. Lett.* **61**, 2051–2053 (1992).

30. Hiruma, K., Yazawa, M., Katsuyama, T., Ogawa, K., Haraguchi, K., Koguchi, M. & Kakibayashi, H. Growth and optical properties of nanometer-scale GaAs and InAs whiskers. *J. Appl. Phys.* **77**, 447–462 (1995).

31. Borgström, M. T., Wallentin, J., Trägårdh, J., Ramvall, P., Ek, M., Wallenberg, L. R., Samuelson, L. & Deppert, K. In situ etching for total control over axial and radial nanowire growth. *Nano Res.* **3**, 264–270 (2010).

32. Kelrich, A., Sorias, O., Calahorra, Y., Kauffmann, Y., Gladstone, R., Cohen, S., Orenstein, M. & Ritter, D. InP Nanoflag Growth from a Nanowire Template by in Situ Catalyst Manipulation. *Nano Lett.* **16**, 2837–2844 (2016).

33. Conesa-Boj, S., Russo-Averchi, E., Dalmau-Mallorqui, A., Trevino, J., Pecora, E. F., Forestiere, C., Handin, A., Ek, M., Zweifel, L., Wallenberg, L. R., Rüffer, D., Heiss,

M., Troadec, D., Dal Negro, L., Caroff, P. & Fontcuberta I Morral, A. Vertical 'III-V' V-shaped nanomembranes epitaxially grown on a patterned Si[001] substrate and their enhanced light scattering. *ACS Nano* **6**, 10982–10991 (2012).

34. Pan, D., Fan, D. X., Kang, N., Zhi, J. H., Yu, X. Z., Xu, H. Q. & Zhao, J. H. Free-Standing Two-Dimensional Single-Crystalline InSb Nanosheets. *Nano Lett.* **16**, 834–841 (2016).

35. De La Mata, M., Leturcq, R., Plissard, S. R., Rolland, C., Magén, C., Arbiol, J. & Caroff, P. Twin-Induced InSb Nanosails: A Convenient High Mobility Quantum System. *Nano Lett.* **16**, 825–833 (2016).

36. Pankoke, V., Kratzer, P. & Sakong, S. Calculation of the diameter-dependent polytypism in GaAs nanowires from an atomic motif expansion of the formation energy. *Phys. Rev. B* **84**, 075455 (2011).

37. Staudinger, P., K, E. M. & Schmid, H. Exploring the Size Limitations of Wurtzite III-V Film Growth. *Nano Lett.* **20**, 686–693 (2019).

38. Rödl, C., Furthmüller, J., Suckert, J. R., Armuzza, V., Bechstedt, F. & Botti, S. Accurate electronic and optical properties of hexagonal germanium for optoelectronic applications. *Prepr. arXiv* 1–11 (2019).

39. Fadaly, E. M. T. *et al.* Direct Bandgap Emission from Hexagonal Ge and SiGe Alloys. *Prepr. arXiv* 1–25 (2019).

40. De, A. & Pryor, C. E. Predicted band structures of III-V semiconductors in the wurtzite phase. *Phys. Rev. B* **81**, 155210 (2010).

41. Assali, S., Zardo, I., Plissard, S., Kriegner, D., Verheijen, M. A., Bauer, G., Meijerink, A., Belabbes, A., Bechstedt, F., Haverkort, J. E. M. & Bakkers, E. P. A. M. Direct Band Gap Wurtzite Gallium Phosphide Nanowires. *Nano Lett.* **13**, 1559–1563 (2013).

42. Lorenz, M. R., Pettit, G. D. & Taylor, R. C. Band gap of gallium phosphide from 0 to 900K and light emission from diodes at high temperatures. *Phys. Rev.* **171**, 876–881 (1968).

43. Panish, M. B. & Casey, H. C. Temperature dependence of the energy gap in GaAs and GaP. *J. Appl. Phys.* **40**, 163–167 (1969).

44. Holt, D. A., Alfrey, G. F. & Wiggins, C. S. Grain boundaries and electroluminescence in gallium phosphide. *Nature* vol. 181 109 (1958).

45. Ullman, F. G. Electroluminescence of Gallium Phosphide Crystals. *Nature* **190**, 161–162 (1961).

46. Starkiewicz, J. & Allen, J. W. Injection Electroluminescence at P-N Juntions in Zinc-Doped Gallium Phosphide. *J. Phys. Chem. Solids* **23**, 881–884 (1962).

47. Gershenzon, M., Logan, R. A. & Nelson, D. F. Electrical and electroluminescent properties of gallium phosphide diffused p-n junctions. *Phys. Rev.* **149**, 580–597 (1966).

48. Gershenzon, M. & Mikulyak, R. M. Electroluminescence at p-n junctions in Gallium Phosphide. *J. Appl. Phys.* **32**, 1338–1348 (1961).

49. Hayes, W., Ryan, J. F., West, C. L. & Dean, P. J. Photoluminescence studies of deep traps in GaP:Fe. *J. Phys. C Solid State Phys.* **13**, 5631–5643 (1980).

50. Rauch, C. J., Stickler, J. J., Zeiger, H. J. & Heller, G. S. Isoelectronic Traps due to Nitrogen in Gallium Phosphide. *Phys. Rev. Lett.* **4**, 64–66 (1960).

51. Dean, P. J., Gershenzon, M. & Kaminsky, G. Green electroluminescence from gallium phosphide diodes near room temperature. *J. Appl. Phys.* **38**, 5332–5342 (1967).

52. Wight, D. R. Green luminescence efficiency in gallium phosphide. *J. Phys. D. Appl. Phys.* **10**, 431–454 (1977).

53. Bechstedt, F. & Belabbes, A. Structure, energetics, and electronic states of III-V compound polytypes. *J. Phys. Condens. Matter* **25**, 273201 (2013).

54. Belabbes, A. & Bechstedt, F. Forbidden Band-Edge Excitons of Wurtzite-GaP: A Theoretical View. *Phys. Status Solidi Basic Res.* **256**, 1800238 (2019).

55. Assali, S., Greil, J., Zardo, I., Belabbes, A., De Moor, M. W. A., Koelling, S., Koenraad, P. M., Bechstedt, F., Bakkers, E. P. A. M. & Haverkort, J. E. M. Optical study of the band structure of wurtzite GaP nanowires. *J. Appl. Phys.* **120**, 044304 (2016).

56. Berg, A., Lehmann, S., Vainorius, N., Gustafsson, A., Pistol, M.-E., Wallenberg, L. R.,

Samuelson, L. & Borgström, M. T. Growth and characterization of wurtzite GaP nanowires with control over axial and radial growth by use of HCl in-situ etching. *J. Cryst. Growth* **386**, 47–51 (2013).

57. Halder, N. N., Cohen, S., Gershoni, D. & Ritter, D. Growth of large diameter pure phase wurtzite GaP nanowires by a two-step axial-radial growth approach. *Appl. Phys. Lett.* **112**, 133107 (2018).

58. Maliakkal, C. B., Gokhale, M., Parmar, J., Bapat, R. D., Chalke, B. A., Ghosh, S. & Bhattacharya, A. Growth, structural and optical characterization of wurtzite GaP nanowires. *Nanotechnology* **30**, 254002 (2019).

59. Nikoobakht, B., Herzing, A., Muramoto, S. & Tersoff, J. Vapor-Liquid-Solid Etch of Semiconductor Surface Channels by Running Gold Nanodroplets. *Nano Lett.* **15**, 8360–8364 (2015).

60. Whiticar, A. M., Mårtensson, E. K., Nygård, J., Dick, K. A. & Bolinsson, J. Annealing of Au, Ag and Au-Ag alloy nanoparticle arrays on GaAs (100) and (111)B. *Nanotechnology* **28**, 205702 (2017).

61. Da Silva, B. C. Master Thesis - Síntese e Caracterização Estrutural de Nanofios de GaP. (University of Campinas, 2016).

62. Wang, K. X., Yu, Z., Liu, V., Cui, Y. & Fan, S. Absorption enhancement in ultrathin crystalline silicon solar cells with antireflection and light-trapping nanocone gratings. *Nano Lett.* **12**, 1616–1619 (2012).

63. Wang, B., Stevens, E. & Leu, P. W. Strong broadband absorption in GaAs nanocone and nanowire arrays for solar cells. *Opt. Express* **22**, A386 (2014).

64. Diedenhofen, S. L., Janssen, O. T. A., Grzela, G., Bakkers, E. P. A. M. & Gómez Rivas, J. Strong geometrical dependence of the absorption of light in arrays of semiconductor nanowires. *ACS Nano* **5**, 2316–2323 (2011).

65. Da Silva, B. C., Oliveira, D. S., Iikawa, F., Couto, O. D. D., Bettini, J., Zagonel, L. F. & Cotta, M. A. Exploring Au Droplet Motion in Nanowire Growth: A Simple Route toward Asymmetric GaP Morphologies. *Nano Lett.* **17**, 7274–7282 (2017).

66. Tsang, W. T. From chemical vapor epitaxy to chemical beam epitaxy. *J. Cryst. Growth*

95, 121–131 (1989).

67. Bortoleto, J. R. R. Doctoral Thesis - Crescimento e Caracterização Estrutural de Nanoestruturas Semicondutoras Baseadas na Liga InP. (University of Campinas, 2005).

68. Vehkamäki, H. *Classical nucleation theory in multicomponent systems*. *Classical Nucleation Theory in Multicomponent Systems* (Springer, 2006).

69. Schmelzer, J. W. P. *Nucleation Theory and Applications*. *Nucleation Theory and Applications* (Wiley, 2005).

70. Zhang, T. H. & Liu, X. Y. Experimental modelling of single-particle dynamic processes in crystallization by controlled colloidal assembly. *Chem. Soc. Rev.* **43**, 2324–2347 (2014).

71. Maliakkal, C. B., Mårtensson, E. K., Tornberg, M., Jacobsson, D., Persson, A. R., Johansson, J., Wallenberg, R. & Dick, K. A. Independent control of nucleation and layer growth in nanowires. *ACS Nano* Article ASAP (2020).

72. Elliott, R. P. & Shunk, F. A. The Au-Si (Gold-Silicon) system. *Bull. Alloy Phase Diagrams* **4**, 362 (1983).

73. Johansson, J., Karlsson, L. S., Dick, K. A., Bolinsson, J., Wacaser, B. A., Deppert, K. & Samuelson, L. Effects of Supersaturation on the Crystal Structure of Gold Seeded III−V Nanowires. *Cryst. Growth Des.* **9**, 766–773 (2008).

74. Elliott, R. P. & Shunk, F. A. The Au-Ga (Gold-Gallium) system. *Bull. Alloy Phase Diagrams* **2**, 356–358 (1981).

75. Sun, R., Jacobsson, D., Chen, I. J., Nilsson, M., Thelander, C., Lehmann, S. & Dick, K. A. Sn-Seeded GaAs Nanowires as Self-Assembled Radial p-n Junctions. *Nano Lett.* **15**, 3757–3762 (2015).

76. T.J. Anderson & Ansara, I. The Ga-Sn (Gallium-Tin)System. *J. Phase Equilibria* **13**, 181–189 (1992).

77. Okamoto, H. Ni-P (nickel-phosphorus). *J. Phase Equilibria Diffus.* **31**, 200–201 (2010).

78. Okamoto, H. Ga-Ni (Gallium-Nickel). *J. Phase Equilibria Diffus.* **29**, 296–296 (2008).

79. Ek, M. Doctoral Thesis - Analysis of Structure, Composition and Growth of Semiconductor Nanowires by Transmission Electron Microscopy. *Lund University* (Lund University, 2013).

80. Caroff, P., Bolinsson, J. & Johansson, J. Crystal phases in III-V nanowires: From random toward engineered polytypism. *IEEE J. Sel. Top. Quantum Electron.* **17**, 829–846 (2011).

81. De Oliveira, D. S. Doctoral Thesis - Alternativas para o Crescimento de Nanofios Semicondutores III-V. (University of Campinas, 2016).

82. . https://www.eng-atoms.msm.cam.ac.uk/RoyalSocDemos/SEM.

83. Walock, M. Doctoral Thesis - Nanocomposite coatings based on quaternary metalnitrogen. (Ecole nationale supérieure d'arts et métiers, 2012).

84. Joyce, H. J. Doctoral Thesis - Growth and Characterisation of III-V Semiconductor Nanowires for Optoelectronic Device Applications. (Australian National University, 2009).

85. Goldstein, J. I. *Scanning electron microscopy and X-ray microanalysis*. (Kluwer Academic/Plenum Publishers, 2003).

86. Williams, D. B. & Carter, C. B. *Transmission Electron Microscopy: A Textbook for Materials Science*. (Springer).

87. Wang, J. Doctoral Thesis - Controlling nanowire growth direction. (Eindhoven University of Technology, 2014).

88. Sarid, D. *Scanning Force Microscopy With Applications to Electric, Magnetic and Atomic Forces*. (Oxford Universiy Press, 1994).

89. *Agilent AFM 5500 Scanning Probe Microscope User ' s Guide. Agil. Technol.* (2008).

90. A Practical Guide to SPM Scanning Probe Microscopy. Veeco Instrum. InC.

91. La Hera, V. R. M. Master Thesis - Optical Properties of Wurtzite Phase InAsP / InP Heterostructure Nanowires Propriedades ópticas de Nanofios de InAsP / InP. (University of Campinas, 2015).

92. Edinburgh Instruments. No Title. https://www.edinst.com/us/blog/what-is-the-stokes-shift/.

93. Zardo, I. Doctoral Thesis - Growth and Raman spectroscopy studies of gold-free catalyzed semiconductor nanowires. (Technische Universität München and Università Degli Studi Di Roma 'Sapienza', 2010).

94. Zardo, I., Conesa-Boj, S., Peiro, F., Morante, J. R., Arbiol, J., Uccelli, E., Abstreiter, G. & Fontcuberta I Morral, A. Raman spectroscopy of wurtzite and zinc-blende GaAs nanowires: Polarization dependence, selection rules, and strain effects. *Phys. Rev. B* **80**, 1–11 (2009).

95. Möller, M., De Lima, M. M., Cantarero, A., Dacal, L. C. O., Madureira, J. R., Iikawa, F., Chiaramonte, T. & Cotta, M. A. Polarized and resonant Raman spectroscopy on single InAs nanowires. *Phys. Rev. B* **84**, 085318 (2011).

96. Arguello, C. A., Rousseau, D. L. & Porto, S. P. S. First-order raman effect in wurtzite-type crystals. *Phys. Rev.* **181**, 1351–1363 (1969).

97. Benyahia, N., Zaoui, A., Madouri, D. & Ferhat, M. Dynamic properties of III-V polytypes from density-functional theory. *J. Appl. Phys.* **121**, (2017).

98. Shay, J. L., Tell, B., Buehler, E. & Wernick, J. H. Band Structure of ZnGeP_2 and ZnSiP2 - Ternary Compounds with Pseudodirect Energy Gaps. *Phys. Rev. Lett.* **30**, 983–986 (1973).

99. Schmidt, Lischka & Zulehner. Excitation-power dependence of the near-band-edge photoluminescence of semiconductors. *Phys. Rev. B. Condens. Matter* **45**, 8989–8994 (1992).

100. Kaufmann, U., Kunzer, M., Maier, M., Obloh, H., Ramakrishnan, A., Santic, B. & Schlotter, P. Nature of the 2.8 eV photoluminescence band in Mg doped GaN. *Appl. Phys. Lett.* **72**, 1326–1328 (1998).

101. Wang, J., Plissard, S., Hocevar, M., Vu, T. T. T., Zehender, T., Immink, G. G. W., Verheijen, M. A., Haverkort, J. & Bakkers, E. P. A. M. Position-controlled [100] InP nanowire arrays. *Appl. Phys. Lett.* **100**, 1–4 (2012).

102. Mårtensson, T., Carlberg, P., Borgström, M., Montelius, L., Seifert, W. & Samuelson,

L. Nanowire arrays defined by nanoimprint lithography. *Nano Lett.* **4**, 699–702 (2004).

103. Otnes, G., Heurlin, M., Graczyk, M., Wallentin, J., Jacobsson, D., Berg, A., Maximov, I. & Borgström, M. T. Strategies to obtain pattern fidelity in nanowire growth from large-area surfaces patterned using nanoimprint lithography. *Nano Res.* **9**, 2852–2861 (2016).

104. Tersoff, J., Jesson, D. E. & Tang, W. X. Running droplets of gallium from evaporation of gallium arsenide. *Science (80-.).* **324**, 236–238 (2009).

105. Zhou, Z. Y., Zheng, C. X., Tang, W. X., Jesson, D. E. & Tersoff, J. Congruent evaporation temperature of GaAs(001) controlled by As flux. *Appl. Phys. Lett.* **97**, 121912 (2010).

106. Wu, J., Wang, Z. M., Li, A. Z., Benamara, M., Li, S. & Salamo, G. J. Nanoscale footprints of self-running gallium droplets on GaAs surface. *PLoS One* **6**, 1–6 (2011).

107. Hilner, E., Zakharov, A. A., Schulte, K., Kratzer, P., Andersen, J. N., Lundgren, E. & Mikkelsen, A. Ordering of the nanoscale step morphology as a mechanism for droplet self-propulsion. *Nano Lett.* **9**, 2710–2714 (2009).

108. Fonseka, H. A., Caroff, P., Wong-leung, J., Ameruddin, A. S. & Tan, H. H. Nanowires Grown on InP(100): Growth Directions , Facets , Crystal Structures and Relative Yield Control. *ACS Nano* **8**, 6945–6954 (2014).

109. Bauer, C. L. Investigation of Interfacial Reactions Between Thin Films of Gold and Substrates of Gallium Arsenide by Transmission Electron Microscopy. *Surf. Sci.* **168**, 395–403 (1986).

110. Grepstad, R. W. B. and J. K. XPS Intensity Analysis for Assessment of Thickness and Composition of Thin Overlayer Films: Application to Chemically Etched GaAs(100) Surfaces. *Surf. Interface Anal.* **14**, 109–114 (1989).

111. Yoshiie, T., Bauer, C. L. & Milnes, A. G. Interfacial Reactions Between Gold Thin Films and GaAs Substrates. *Thin Solid Films* **111**, 149–166 (1984).

112. Richards, J. L. & Crocker, A. J. Etch pits in Gallium Arsenide. *J. Appl. Phys.* **31**, 611–612 (1960).

113. Tarui, Y., Komiya, Y. & Harada, Y. Preferential Etching and Etched Profile of GaAs. *J. Electrochem. Soc.* **118**, 118–122 (1971).

114. Kumar, K. & Kumar, K. Electron microscopic study of alloying behavior or Au on GaAs. *Jpn. J. Appl. Phys.* **18**, 713–716 (1979).

115. Isomura, N., Tsukamoto, S., Iizuka, K. & Arakawa, Y. Investigation on GaAs(001) surface treated by As-free high temperature cleaning method. *J. Cryst. Growth* **301**–**302**, 26–29 (2007).

116. Tone, K., Yamada, M., Ide, Y. & Katayama, Y. Characterization of oxidized GaAs (001) surfaces using temperature programed desorption and x-ray photoelectron spectroscopy. *Jpn. J. Appl. Phys.* **31**, L721–L724 (1992).

117. Coluci, V., Cotta, M., Mendonça, C., I.-Landers, K. & de Carvalho, M. Surface morphologies in GaAs homoepitaxy: Mound formation and evolution. *Phys. Rev. B - Condens. Matter Mater. Phys.* **58**, 1947–1953 (1998).

118. Tersoff, J., Jesson, D. E. & Tang, W. X. Decomposition controlled by surface morphology during Langmuir evaporation of GaAs. *Phys. Rev. Lett.* **105**, 1–4 (2010).

119. Zhang, C., Miao, X., Mohseni, P. K., Choi, W. & Li, X. Site-controlled VLS growth of planar nanowires: Yield and mechanism. *Nano Lett.* **14**, 6836–6841 (2014).

120. Oliveira, D. S., Tizei, L. H. G., Li, A., Vasconcelos, T. L., Senna, C. A., Archanjo, B. S., Ugarte, D. & Cotta, M. A. Interaction between lamellar twinning and catalyst dynamics in spontaneous core-shell InGaP nanowires. *Nanoscale* **7**, 12722–12727 (2015).

121. Plante, M. C. & LaPierre, R. R. Au-assisted growth of GaAs nanowires by gas source molecular beam epitaxy: Tapering, sidewall faceting and crystal structure. *J. Cryst. Growth* **310**, 356–363 (2008).

122. Sohn, J. I., Hong, W. K., Lee, S., Lee, S., Ku, J., Park, Y. J., Hong, J., Hwang, S., Park, K. H., Warner, J. H., Cha, S. & Kim, J. M. Surface energy-mediated construction of anisotropic semiconductor wires with selective crystallographic polarity. *Sci. Rep.* **4**, 5680 (2014).

123. Moore, D. & Wang, Z. L. Growth of anisotropic one-dimensional ZnS nanostructures.

J. Mater. Chem. **16**, 3898–3905 (2006).

124. Yang, X., Shu, H., Liang, P., Cao, D. & Chen, X. Crystal phase and facet effects on the structural stability and electronic properties of GAP nanowires. *J. Phys. Chem. C* **119**, 12030–12036 (2015).

125. Ikejiri, K., Kitauchi, Y., Tomioka, K., Motohisa, J. & Fukui, T. Zinc blende and wurtzite crystal phase mixing and transition in indium phosphide nanowires. *Nano Lett.* **11**, 4314–4318 (2011).

126. Guo, Y. N., Xu, H. Y., Auchterlonie, G. J., Burgess, T., Joyce, H. J., Gao, Q., Tan, H. H., Jagadish, C., Shu, H. B., Chen, X. S., Lu, W., Kim, Y. & Zou, J. Phase separation induced by Au catalysts in ternary InGaAs nanowires. *Nano Lett.* **13**, 643–650 (2013).

127. Zhang, X., Zou, J., Paladugu, M., Guo, Y., Wang, Y., Kim, Y., Joyce, H. J., Gao, Q., Tan, H. H. & Jagadish, C. Evolution of Epitaxial InAs Nanowires on GaAs (111)B. *Small* **5**, 366–369 (2009).

128. Mavel, A., Chauvin, N., Regreny, P., Patriarche, G., Masenelli, B. & Gendry, M. Study of the nucleation and growth of InP nanowires on silicon with gold-indium catalyst. *J. Cryst. Growth* **458**, 96–102 (2017).

129. Zhang, Z., Lu, Z. Y., Chen, P. P., Lu, W. & Zou, J. Defect-free zinc-blende structured InAs nanowires realized by in situ two V/III ratio growth in molecular beam epitaxy. *Nanoscale* **7**, 12592–12597 (2015).

130. Glas, F., Harmand, J. C. & Patriarche, G. Why does wurtzite form in nanowires of III-V zinc blende semiconductors? *Phys. Rev. Lett.* **99**, 3–6 (2007).

131. Tsivion, D. & Joselevich, E. Guided growth of horizontal GaN nanowires on spinel with orientation-controlled morphologies. *J. Phys. Chem. C* **118**, 19158–19164 (2014).

132. Heiß, M., Riedlberger, E., Spirkoska, D., Bichler, M., Abstreiter, G. & Morral, A. F. i. Growth mechanisms and optical properties of GaAs-based semiconductor microstructures by selective area epitaxy. *J. Cryst. Growth* **310**, 1049–1056 (2008).

133. Heinecke, H. & Wachter, M. Mechanisms and applications of selective area growth by metalorganic molecular beam epitaxy (CBE). *Appl. Surf. Sci.* **113**–**114**, 1–8 (1997).

134. Barabási, A. L. Self-assembled island formation in heteroepitaxial growth. *Appl. Phys. Lett.* **70**, 2565–2567 (1997).

135. Gutiérrez, H. R., Cotta, M. A., Bortoleto, J. R. R. & De Carvalho, M. M. G. Role of group V exchange on the shape and size of InAs/InP self-assembled nanostructures. *J. Appl. Phys.* **92**, 7523–7526 (2002).

136. Hauge, H. I. T., Verheijen, M. A., Conesa-Boj, S., Etzelstorfer, T., Watzinger, M., Kriegner, D., Zardo, I., Fasolato, C., Capitani, F., Postorino, P., Kölling, S., Li, A., Assali, S., Stangl, J. & Bakkers, E. P. A. M. Hexagonal Silicon Realized. *Nano Lett.* **15**, 5855–5860 (2015).

137. Belabbes, A., Panse, C., Furthmüller, J. & Bechstedt, F. Electronic bands of III-V semiconductor polytypes and their alignment. *Phys. Rev. B* **86**, 075208 (2012).

138. Brozel, M. R., Newman, R. C. & Clegg, J. B. Carbon, oxygen and silicon impurities in gallium arsenide. *J. Phys. D. Appl. Phys.* **11**, 1331–1339 (1978).

139. Watkins, S. P. & Haacke, G. Carbon acceptor incorporation in GaAs grown by metalorganic chemical vapor deposition: Arsine versus tertiarybutylarsine. *Appl. Phys. Lett.* **59**, 2263–2265 (1991).

140. Dapkus, P. D., Manasevit, H. M., Hess, K. L., Low, T. S. & Stillman, G. E. High Purity GaAs Prepared from Trimethylgallium and Arsine. *J. Cryst. Growth* **55**, 10–23 (1981).

141. Seki, Y., Tanno, K., Iida, K. & Ichiki, E. Properties of Epitaxial GaAs Layers from a Triethyl Gallium and Arsine System. *J. Electrochem. Soc.* **122**, 1108–1112 (1975).

142. Hata, M., Fukuhara, N., Zempo, Y., Isemura, M., Yako, T. & Maeda, T. Residual impurities in epitaxial layers grown by MOVPE. *J. Cryst. Growth* **93**, 543–549 (1988).

143. Johansson, J., Dick, K. A., Caroff, P., Messing, M. E., Bolinsson, J., Deppert, K. & Samuelson, L. Diameter dependence of the wurtzite-zinc blende transition in inas nanowires. *J. Phys. Chem. C* **114**, 3837–3842 (2010).

144. Panda, J. K., Roy, A., Gemmi, M., Husanu, E., Li, A., Ercolani, D. & Sorba, L. Electronic band structure of wurtzite GaP nanowires via temperature dependent resonance Raman spectroscopy. *Appl. Phys. Lett.* **103**, 023108 (2013).

145. Chen, G., Wu, J., Lu, Q., Gutierrez, H. R., Xiong, Q., Pellen, M. E., Petko, J. S., Werner, D. H. & Eklund, P. C. Optical Antenna Effect in Semiconducting Nanowires. *Nano Lett.* **8**, 1341–1346 (2008).

146. Peng, W., Jabeen, F., Jusserand, B., Harmand, J. C. & Bernard, M. Conduction band structure in wurtzite GaAs nanowires: A resonant Raman scattering study. *Appl. Phys. Lett.* **100**, 073102 (2012).

147. Martin, R. M. & Damen, T. C. Breakdown of selection rules in resonance Raman scattering. *Phys. Rev. Lett.* **26**, 86–88 (1971).

148. Leite, R. C. C. & Porto, S. P. S. Enhancement of Raman Cross Section in CdS due to Resonant Absorpion. *Phys. Rev. Lett.* **17**, 10–12 (1966).

149. Gajaria, T. K., Dabhi, S. D. & Jha, P. K. ab initio Energetics and Thermoelectric Profiles of Gallium Pnictide Polytypes. *Sci. Rep.* **9**, 5884 (2019).

150. Spindler, C., Galvani, T., Wirtz, L., Rey, G. & Siebentritt, S. Excitation-intensity dependence of shallow and deep-level photoluminescence transitions in semiconductors. *J. Appl. Phys.* **126**, 175703 (2019).

151. Varshni, Y. P. Temperature dependence of the energy gap in semiconductors. *Physica* **34**, 149–154 (1967).

152. Assali, S., Lähnemann, J., Vu, T. T. T., Jöns, K. D., Gagliano, L., Verheijen, M. A., Akopian, N., Bakkers, E. P. A. M. & Haverkort, J. E. M. Crystal Phase Quantum Well Emission with Digital Control. *Nano Lett.* **17**, 6062–6068 (2017).

153. Assali, S. Doctoral Thesis - Pure Crystal Phase Nanowires : Growth and Optical Properties. (Eindhoven University of Technology, 2015).

154. Dean, P. J. & Ilegems, M. The optical properties of Be, Mg and Zn-diffused gallium phosphide. *J. Lumin.* **4**, 201–230 (1971).

155. Elliott, R. J. Intensity of optical absorption by excitons. *Phys. Rev.* **108**, 1384–1389 (1957).

156. Pankove, J. I. Absorption edge of impure gallium arsenide. *Phys. Rev.* **140**, A2059–A2063 (1965).

157. Dash, W. C. & Newman, R. Intrinsic Optical Absorption in single-Crystal Ge and Si. *Phys. Rev.* **99**, 1151–1154 (1955).

158. Dean, P. J., Frosch, C. J. & Henry, C. H. Optical properties of the group IV elements carbon and silicon in gallium phosphide. *J. Appl. Phys.* **39**, 5631–5646 (1968).

159. Fazzio, A., Brescansin, L. M. & Leite, J. R. Electronic structure of neutral and negatively charged gallium vacancies in GaP. *J. Phys. C Solid State Phys.* **15**, L1–L3 (1982).

160. Jaros, M. Electronic properties of paramagnetic P(Ga) in GaP. *J. Phys. C Solid State Phys.* **11**, L213–L217 (1978).

161. Van De Ven, J., Schoot, H. G. & Giling, L. J. Influence of growth parameters on the incorporation of residual impurities in gaas grown by metalorganic chemical vapor deposition. *J. Appl. Phys.* **60**, 1648–1660 (1986).

162. Roth, A. P., Charbonneau, S. & Goodchild, R. G. Residual shallow acceptors in GaAs layers grown by metal-organic vapor phase epitaxy. *J. Appl. Phys.* **54**, 5350–5357 (1983).

163. Williams, E. W. Evidence for self-activated luminescence in GaAs: The gallium vacancy-donor center. *Phys. Rev.* **168**, 922–928 (1968).

164. Tsang, W. T. Modelling of chemical beam epitaxy. *J. Cryst. Growth* **98**, 226–233 (1989).

165. Greil, J., Assali, S., Isono, Y., Belabbes, A., Bechstedt, F., Valega MacKenzie, F. O., Silov, A. Y., Bakkers, E. P. A. M. & Haverkort, J. E. M. Optical Properties of Strained Wurtzite Gallium Phosphide Nanowires. *Nano Lett.* **16**, 3703–3709 (2016).

166. Givargizov, E. I. Fundamental aspects of VLS growth. *J. Cryst. Growth* **31**, 20–30 (1975).

167. Algra, R. E., Verheijen, M. A., Borgström, M. T., Feiner, L. F., Immink, G., Van Enckevort, W. J. P., Vlieg, E. & Bakkers, E. P. A. M. Twinning superlattices in indium phosphide nanowires. *Nature* **456**, 369–372 (2008).

168. Caroff, P., Dick, K. A., Johansson, J., Messing, M. E., Deppert, K. & Samuelson, L.

Controlled polytypic and twin-plane superlattices in III-V nanowires. *Nat. Nanotechnol.* **4**, 50–55 (2009).

169. Dick, K. A., Deppert, K., Larsson, M. W., Mårtensson, T., Seifert, W., Wallenberg, L. R. & Samuelson, L. Synthesis of branched 'nanotrees' by controlled seeding of multiple branching events. *Nat. Mater.* **3**, 380–384 (2004).

170. Kornienko, N., Gibson, N. A., Zhang, H., Eaton, S. W., Yu, Y., Aloni, S., Leone, S. R. & Yang, P. Growth and Photoelectrochemical Energy Conversion of Wurtzite Indium Phosphide Nanowire Arrays. *ACS Nano* **10**, 5525–5535 (2016).

171. Miao, X., Zhang, C. & Li, X. Monolithic barrier-all-around high electron mobility transistor with planar GaAs nanowire channel. *Nano Lett.* **13**, 2548–2552 (2013).

172. Ramirez, J. M. *et al.* III-V-on-Silicon Integration: From Hybrid Devices to Heterogeneous Photonic Integrated Circuits. *IEEE J. Sel. Top. Quantum Electron.* **26**, 6100213 (2019).

173. Björk, M. T., Schmid, H., Breslin, C. M., Gignac, L. & Riel, H. InAs nanowire growth on oxide-masked ⟨111⟩ silicon. *J. Cryst. Growth* **344**, 31–37 (2012).

174. Corbett, B., Bower, C., Fecioru, A., Mooney, M., Gubbins, M. & Justice, J. Strategies for integration of lasers on silicon. *Semicond. Sci. Technol.* **28**, 094001 (2013).

175. Schulz, M. Determination of deep trap levels in silicon using ion-implantation and CV-measurements. *Appl. Phys.* **4**, 225–236 (1974).

176. Lindberg, C., Whiticar, A., Dick, K. A., Sköld, N., Nygård, J. & Bolinsson, J. Silver as Seed-Particle Material for GaAs Nanowires - Dictating Crystal Phase and Growth Direction by Substrate Orientation. *Nano Lett.* **16**, 2181–2188 (2016).

177. Huang, K., Zhang, Z., Zhou, Q., Liu, L., Zhang, X., Kang, M., Zhao, F., Lu, X., Gao, X. & Liu, J. Silver catalyzed gallium phosphide nanowires integrated on silicon and in situ Ag-alloying induced bandgap transition. *Nanotechnology* **26**, 255706 (2015).

178. Oliveira, D. S., Zavarize, M., Tizei, L. H. G., Walls, M., Ospina, C. A., Iikawa, F., Ugarte, D. & Cotta, M. A. Different growth regimes in InP nanowire growth mediated by Ag nanoparticles. *Nanotechnology* **28**, 505604 (2017).

179. Hillerich, K., Messing, M. E., Reine Wallenberg, L., Deppert, K. & Dick, K. A. Epitaxial InP nanowire growth from Cu seed particles. *J. Cryst. Growth* **315**, 134–137 (2011).

180. Sun, R., Vainorius, N., Jacobsson, D., Pistol, M. E., Lehmann, S. & Dick, K. A. Sn-seeded GaAs nanowires grown by MOVPE. *Nanotechnology* **27**, 215603 (2016).

181. Wang, Y., Schmidt, V., Senz, S. & Gösele, U. Epitaxial growth of silicon nanowires using an aluminium catalyst. *Nat. Nanotechnol.* **1**, 186–189 (2006).

182. Kohen, D., Cayron, C., De Vito, E., Tileli, V., Faucherand, P., Morin, C., Brioude, A. & Perraud, S. Aluminum catalyzed growth of silicon nanowires: Al atom location and the influence of silicon precursor pressure on the morphology. *J. Cryst. Growth* **341**, 12–18 (2012).

183. Oliveira, D. S., Tizei, L. H. G., Ugarte, D. & Cotta, M. A. Spontaneous periodic diameter oscillations in InP nanowires: The role of interface instabilities. *Nano Lett.* **13**, 9–13 (2013).

184. Liu, H. S., Wang, J. & Jin, Z. P. Thermodynamic optimization of the Ni-Sn binary system. *Calphad Comput. Coupling Phase Diagrams Thermochem.* **28**, 363–370 (2004).

185. Davidson, F. M., Lee, D. C., Fanfair, D. D. & Korgel, B. A. Lamellar twinning in semiconductor nanowires. *J. Phys. Chem. C* **111**, 2929–2935 (2007).

186. Johansson, J., Karlsson, L. S., Dick, K. A., Bolinsson, J., Wacaser, B. A., Deppert, K. & Samuelson, L. Effects of supersaturation on the crystal structure of gold seeded III-V nanowires. *Cryst. Growth Des.* **9**, 766–773 (2009).

187. Krishnamachari, U., Borgstrom, M., Ohlsson, B. J., Panev, N., Samuelson, L., Seifert, W., Larsson, M. W. & Wallenberg, L. R. Defect-free InP nanowires grown in [001] direction on InP (001). *Appl. Phys. Lett.* **85**, 2077–2079 (2004).

Appendices

A.1 - Growth of asymmetric WZ GaP NW arrays

We have grown asymmetric WZ GaP nanowires in arrays, using patterned gold dots (20 nm) fabricated by Electron Beam Lithography (EBL) at CCSNano/UNICAMP, using the conditions described in Table A1. The growth conditions were the same as reported for sample B3 in chapter 3.

Substrate cleaning	15min acetone (in ultrasonication)
	15min isopropanol (in ultrasonication)
	5 min DI water (in ultrasonication)
Resist deposition	Pré-*bake* a 200°C for 10 min
	Adhesion promoter (HMDS): 5000rpm for 30s
	Wait for 1 min
	PMMA (ARP 670-04): 5000rpm for 30s
	Bake at 180°C for 3min
Exposition	Dose: 0,025µC/cm^2
	20 nm diameter dots
	Distance between dots 1-4µm
Development	90s no developer ARP 600-56
	Stopper: isopropanol
Evaporation (gold)	5 nm Au film 5nm
Lift-off	1h hot acetone (80°C) + 24h in acetone at room temperature

Table A1 – Steps and conditions for the fabrication of Au dots with 20 nm diameter used for the growth of asymmetric GaP NWs.

We observed that the results for the growth conditions that lead to this WZ asymmetric morphology are transferable to different methods of formation of gold nanoparticles, Fig. A1, since the results reported in chapter 3 were obtained using colloidal gold nanoparticles, and here gold was obtained via thermal evaporation for the dot arrays. In addition, approximately 40% of nanowires grow in an asymmetrical shape, with the growth direction along the c <0001> axis, leading to two growth directions that form projections along the directions ±[110] on the substrate surface (Fig. A1), as we have already observed in chapter 3. In addition, some nanowires grow in directions perpendicular to the substrate, while others are not even formed, as can be seen in Fig. A1.
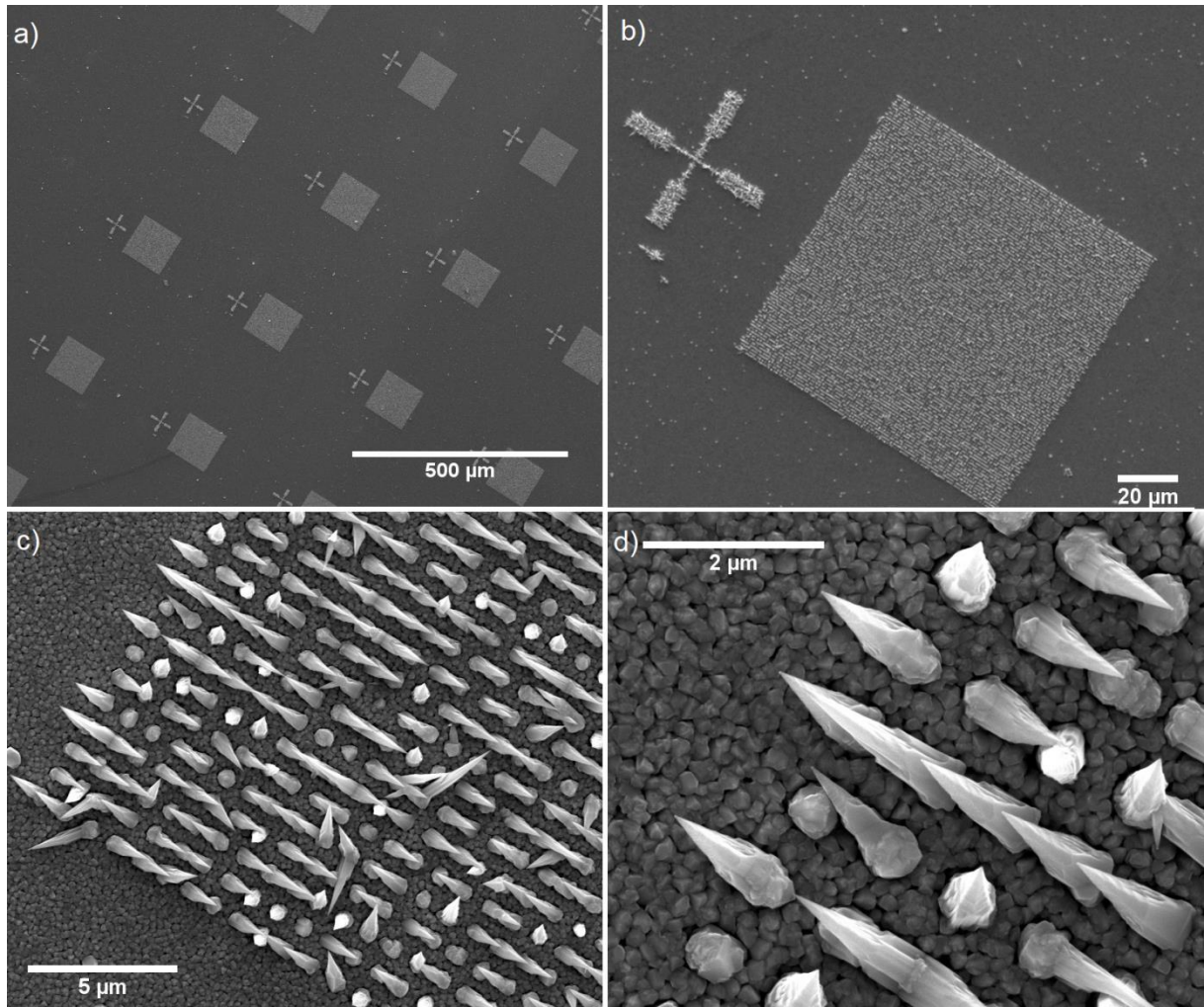
Figure A1 – Top-view SEM images of *arrays* of WZ GaP nanowires grown using arrays of 20 nm diameter gold, fabricated throught EBL (Electron Beam Lithography).

A.2 – Si-doped arrays of GaP NWs

These samples were grown using gold arrays of 20 nm and 2 μm spacing for the growth of Si-doped GaP WZ NWs under different conditions, as described in Table A2. For all runs, GaAs(111)B was used as substrate.

Sample	TEG (sccm)	PH$_3$ (sccm)	Time (min)	Growth Temperature (°C)	Si Knudsen cell Temperature (°C)
Y1	2.4	15.0	60	510	1050
Y2	2.4	15.0	60	510	1100
Y3	2.4	15.0	60	510	1150

Table A2 – Growth conditions for the Si doped arrays of GaP NWs.

Moderate quality arrays were obtained, as observed in Fig. A2a,b; few nanowires are missing within the array and most structures grew vertically in direction [111]B with the characteristic asymmetric morphology. We can conclude that the introduction of the dopant in

situ did not change the growth dynamics dramatically, and the asymmetric morphology is preserved (Fig. A2a,b), which is a positive result for the fabrication of more complex structures, such as p-n junctions using these nanowires. However, we still observe the splitting of some nanoparticles and the formation of more than one nanowire per site.
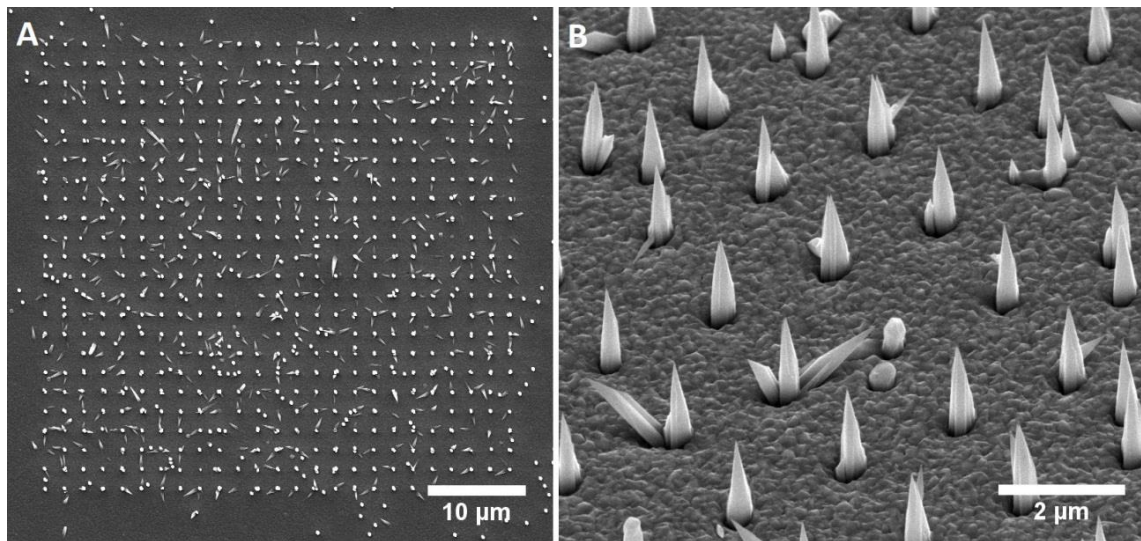

Figure A2 - Top-view SEM images of *arrays* of Si doped WZ GaP nanowires, using the Si effusion cell at 1150°C during growth.

B - Growth of GaAs NWs using other catalysts: Ag, Al and Cu

We have also investigated the use of different metals for the growth of GaAs NWs. Silver can be used as a catalyst for GaAs nanowires. This result was possible for higher temperatures than those used for Au-catalyzed growth under similar precursor flow conditions [176]. Table B1 shows the growth conditions under which the growth of GaAs nanowires using silver (Ag) nanoparticles was investigated.

Sample	TEG (sccm)	AsH₃ (sccm)	Time (min)	NP (nm)	Temperature (°C)
Z1	2.2	5.0	60	Ag 20	450
Z2	2.2	5.0	60	Ag 20	480
Z3	2.2	5.0	60	Ag 20	510
Z4	2.2	5.0	60	Cu 35	290
Z5	2.2	5.0	60	Cu 35	390
Z6	2.2	5.0	60	Cu 35	430
Z7	2.2	5.0	60	Cu 35	510

Table B1 – Growth conditions for the Ag catalyzed GaAs nanowires.

We have observed that Ag-catalyzed growth occurs at elevated temperatures, as can be seen in Fig. B1a,b. For growth at 480°C, nanowires begin to form, but it is apparent that the axial growth rate is not much higher than Vapor-Solid growth, so that the structure takes a rather flat shape, Fig. B1a. At 510 ° C we identify nanowire growth, but with populations showing different characteristics. We observed no nanowire growing at temperatures below 480 ° C (not shown here).
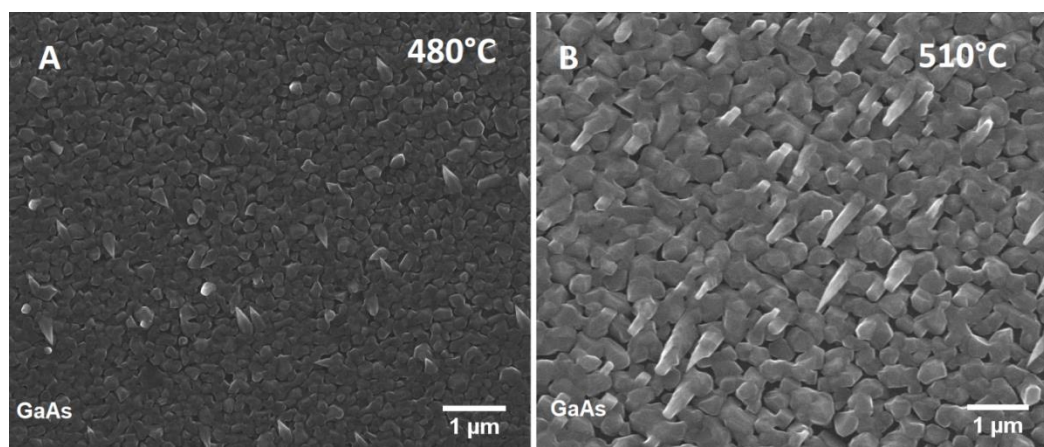

Figure B1 - Top-view SEM images of Ag-catalyzed GaAs nanowires grown at different temperatures.

On the other hand, Cu catalyzed GaAs nanostructures exhibit very low growth rates, in a very low temperature range, as can seen in Fig. B2a,b. For higher temperatures than 390°C, any nanostructure was obtained (not shown here). However, in a CBE system the growth

temperature should be above 300°C, so that TEG pyrolysis occurs at reasonable rates. Thus, despite observing that some growth can occur at 290°C, the diminished Ga availability for growth most likely leads to the low growth rate observed.
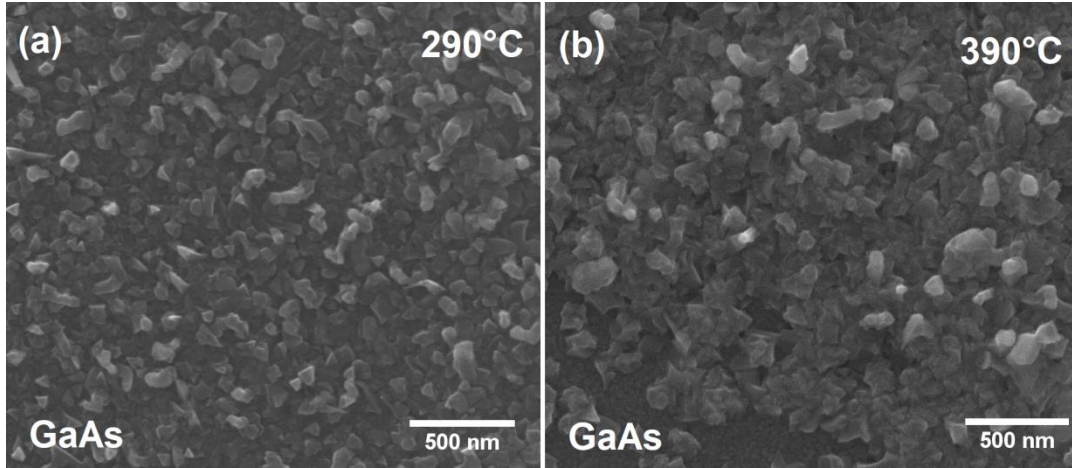

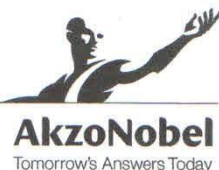**Figure B2** - Top-view SEM images of Cu-catalyzed GaAs nanostructures grown at different temperatures.

Using Al no sucessful results was obtained for GaP and GaAs in a wide varied of growth conditions as temperature and precursors flow.

C – Datasheet for the Triethylgallium (TEG) used is this work

The organometallic TEG used as precursor for group III was a eletronic grade TEG obtained from Akzonobel. Very low traces of some impurities are present in the bottle, as shown in Fig. C1.

Akzo Nobel Polymer
Chemicals LLC
Battleground Site

Certificate of Analysis

AkzoNobel
Tomorrow's Answers Today

Customer   ESCOLA POLITECNICA DA USP
Location   Sao Paolo, Brazil

TRIETHYLGALLIUM – Select Semiconductor Grade

Product   TEGa SSG
Lot Number   0812GE1033
Control Number   154129

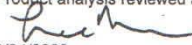| Component	Units	Result	Max	Test Method
B	PPM	<0.5	0.5	JA-812, 817
Ca	PPM	<0.05	0.1	JA-812, 817
Cd	PPM	<0.1	0.2	JA-812, 817
Cr	PPM	<0.2	0.2	JA-812, 817
Cu	PPM	<0.3	0.3	JA-812, 817
Fe	PPM	<0.2	0.2	JA-812, 817
Ge	PPM	<0.1	0.1	JA-812, 817
Mg	PPM	<0.1	0.1	JA-812, 817
Mn	PPM	<0.1	0.1	JA-812, 817
Ni	PPM	<0.3	0.3	JA-812, 817
Pb	PPM	<0.2	0.5	JA-812, 817
S	PPM	<0.1	0.2	JA-812, 817
Si	PPM	<0.1	0.4	JA-812, 817
Sn	PPM	<0.2	0.2	JA-812, 817
Zn	PPM	<0.2	0.2	JA-812, 817

Trace metals determined by inductively coupled plasma emission spectroscopy.
"PPM" is calculated on a metals only basis, i.e.: ug/g Al.

Oxygen	PPM	0.0	1.0	JA-808

nd = non-detectable (Below the Level of Detection)

Gallium (theoretical) = 44.5 wt%

Product analysis reviewed and approved by AkzoNobel Process Quality Control Lab

HPMO final verification by
Date   3/24/2009

QCF - 001   Reference: ICS - 331   154129_66371.doc

www.akzonobel.com/polymer   ISO 9001 certified

Figure C1 - Datasheet for the TEG used in CBE growth presented in this work. The TEG was obtained from Akzonobel.
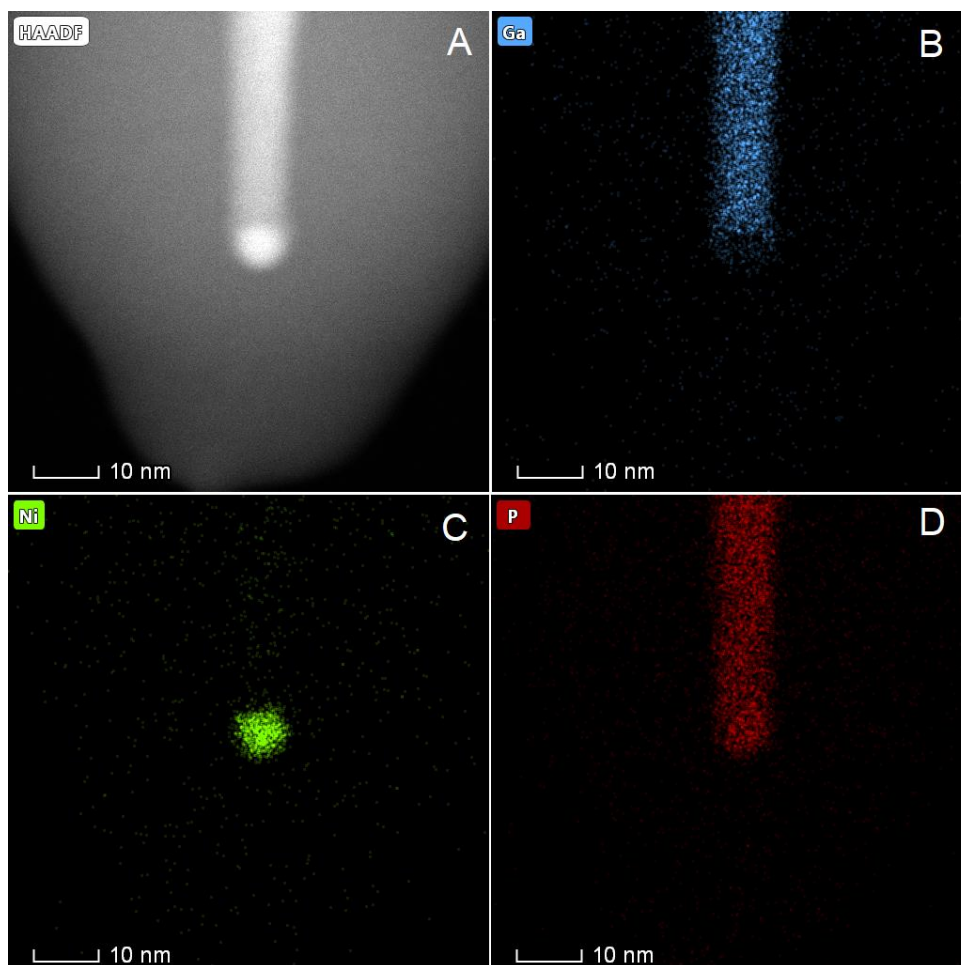
D – Additional EDS analysis of the Ni-catalyzed GaP NWs

Figure D1 – (A) HAADF image of the tip of a Ni-catalyzed curly GaP NW shown in Fig.5.8. (B - D) EDS images showing the different element present in the NP, Gallium (Ga), Nickel (Ni) and phosphorus (P), respectively.

E – Determination of the optical absorption energies

Dipole-forbidden (or pseudo-direct) transitions are characterized by the following absorption response [3]:

$$\alpha = A(E - E_g)^{3/2}$$

We can plot a linear relation with energy by:

$$\alpha^{2/3} = A(E - E_g) = aE + b$$

Therefore,

$$E = E_g \text{ , when } \alpha^{2/3} = 0,$$

$$E_g = \frac{-b}{a}$$

Direct dipole allowed transitions exhibit a different response[3], $\alpha = A(E - E_g)^{1/2}$. However, no linear curves could be reliably fitted to the data using the exponent $n = 1/2$; the best linearization was obtained with this specific exponent ($n = 3/2$). The absorption background generated due to impurity absorptions, I_0, has been subtracted from the optical data before linearization of the first absorption edge, Fig. E1a.
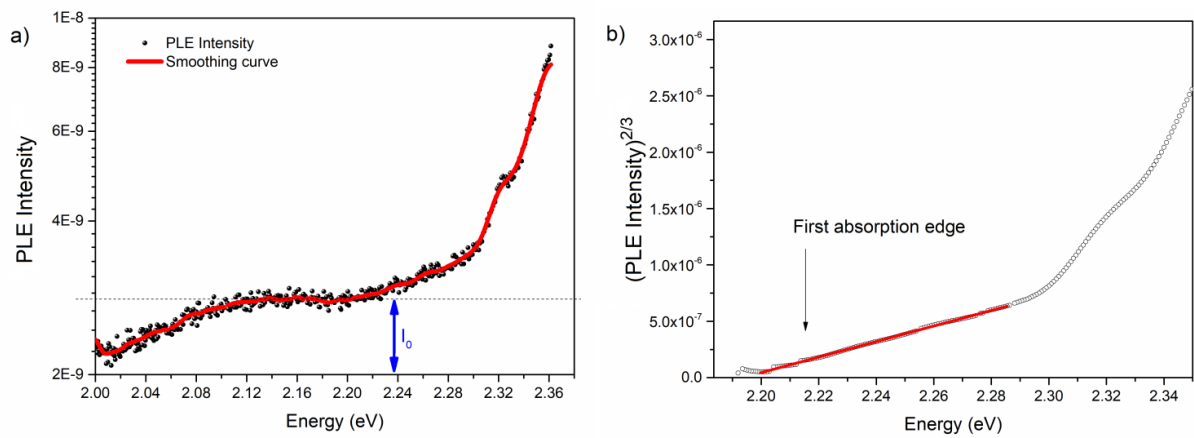

Figure E1 – (a) PLE spectrum and smoothing curve. The I_0 background, subtracted for the first absorption edge, is highlighted. (b) Linear PLE intensity and linear fit for the first absorption edge.

The linear fitting for the first absorption edge (Fig. E1b), associated to the band gap, provides:

Parameters	Value (10^{-6})	Uncertainty (10^{-8})
a	6.893 eV^{-1}	2.31 eV^{-1}
b	-15.12	5.18

Table E1 – Parameters of the linear fit presented in Fig. E.1b.

Therefore,

$$E_g = \frac{-b}{a} = 2.194 \ eV$$

The uncertainty $\mu_{linear \ fit}$ was:

$$\mu_{linear \ fit} = E_g \sqrt{\left(\frac{\mu_a}{a}\right)^2 + \left(\frac{\mu_b}{b}\right)^2} = 12.3 \ meV$$

The propagation of the uncertainty provides:

$$\mu^2_{E_{A,B,C}} = \mu^2_{linear \ fit} + \mu^2_{single \ monoch.} + \mu^2_{others}$$

Where $\mu_{linear \ fit}$ is the uncertainty of the linear fitting of the considered absorption edge (Fig. E1b), $\mu_{single \ monoch.}$ is the uncertainty of the single monochromator coupled to the Xe lamp, which was used as excitation source, and μ_{others} is an uncertainty related to the double monochromator used for the detection, background subtraction and other less significant sources. The energy uncertainty for the double monochromator is ~ 1 meV; considering that $\mu_{others} \ll \mu_{single \ monoch.}$ and $\mu_{others} \ll \mu_{linear \ fit}$:

$$\mu^2_{E_{A,B,C}} = \mu^2_{linear \ fit} + \mu^2_{single \ monoch.}$$

$$\mu_{E_{A,B,C}} = \sqrt{\mu^2_{linear \ fit} + \mu^2_{single \ monoch.}}$$

We have measured the uncertainty related to the single monochromator that is coupled to the Xe lamp as:

$$\mu_{single \ monoch.} = 8 \ meV$$

For the first absorption edge, related to the band gap $E_A = E_g$:

$$\mu_{E_g} = \sqrt{(12.3 \ meV)^2 + (8 \ meV)^2} \cong 0.0147 \ eV,$$

$$\mu_{E_g} \cong 0.015 \ eV = 20 \ meV$$

Therefore,

$$E_g = (2.19 \pm 0.02) \ eV$$

The other two lowest electronic transitions have also been predicted to be dipole-forbidden transitions. Thus, applying the same analysis for each absorption edge, we have found:

$$E_B = \frac{-b}{a} = 2.298 \ eV$$

$$E_C = \frac{-b}{a} = 2.329 \ eV$$

and

$$\mu_{E_B} = \sqrt{(23.8 \ meV)^2 + (8 \ meV)^2} \cong 0.0251 \ eV$$

$$\mu_{E_C} = \sqrt{(18.5 \ meV)^2 + (8 \ meV)^2} \cong 0.0202 \ eV$$

$$\mu_{E_B} \cong 0.025 \ eV \cong 30 \ meV$$

$$\mu_{E_C} \cong 0.020 \ eV = 20 \ meV$$

Therefore,

$$E_B = (2.30 \pm 0.03) \ eV$$

$$E_C = (2.33 \pm 0.02) \ eV$$

List of Publications

Da Silva, B. C.; Oliveira, D. S.; Iikawa, F.; Couto Jr., O. D. D., Bettini, J.; Zagonel, L. F. and Cotta, M. A. Exploring Au Droplet Motion in Nanowire Growth: A Simple Route Toward Asymmetric GaP Morphologies, *Nano Letters*, **17**, (2017), 7274-7282.

Da Silva, B. C.; Couto Jr., O. D. D.; Obata, H. T. Obata, de Lima, M. M.; Bonani, F. D.; de Oliveira, C. E.; Sipahi, G. M.; Iikawa, Fernando and Cotta, M. A. Optical Absorption Exhibits Pseudo-Direct Band Gap of Wurtzite Gallium Phosphide, accepted to *Scientific Reports.*

Da Silva, B. C.; Couto Jr., O. D. D.; Obata, H. T.; Senna, C. A.; Archanjo, B. S.; Iikawa, F. and Cotta, M. A. Deep and Shallow Levels Optical Emissions in Wurtzite GaP Nanowires. *In preparation.*

Da Silva, B. C.; Obata, H. T.; Schreiner, W. H.; Lambert, C. S.; Couto Jr., O. D. D.; Iikawa, F. and Cotta, M A. The growth of GaP nanowires by Ni nanoparticles: Different Growth Mechanism and Green Luminescence. *In preparation.*

CONFERENCE PRESENTATIONS

2019 3NANO2019, Brasília (Brazil) - oral

Gallium Phosphide Nanowires: Epitaxial Growth and Optical Properties

2019 Nanowire Week, Pisa (Italy) - poster

Probing Electronic Band Structure of Hexagonal Gallium Phosphide Using Photoluminescence Excitation Spectroscopy

2018 MRS Fall Meeting, Boston (USA) – poster

Investigating the Impurity Effects in WZ GaP Nanowire Optical Properties and Alternative Seed Catalysts

2018 B-MRS Meeting, Natal (Brazil) - oral

Doping Effect of Optical Transitions in Wurtzite GaP Nanowires

2017 Workshop in Epitaxial Growth, Campinas (Brazil) - oral

Yellow Luminescence in WZ GaP Nanowires

2017 Nanowire Week, Lund (Sweden) - poster

Asymmetrically-shaped Morphologies in Wurtzite GaP Nanowire Growth

2016 B-MRS Meeting, Campinas (Brazil) - poster

Asymmetrically-shaped Morphologies in WZ GaP Nanowire Growth